Master Thesis

Impact of Irradiations by Protons with different Energies on Silicon Sensors

Coralie Neubüser

Hamburg, January 2013

Universität Hamburg
Fachbereich Physik
Institut für Experimentalphysik

Erstgutachter: Prof. Dr. Erika Garutti
Zweitgutachter: Prof. Dr. Wolfgang Hansen

Abstract

In the frame of the CMS tracker upgrade campaign the radiation damage of oxygen-rich n-type silicon pad diodes induced by 23 MeV and 23 GeV protons was investigated. The diodes were manufactured by Hamamatsu Photonics. After irradiation with 1 MeV neutron equivalent fluences between 1×10^{11} cm^{-2} and 1.5×10^{15} cm^{-2}, the sensors were electrically characterized by means of capacitance-voltage (CV) and current-voltage (IV) measurements. Current pulses recorded by the Transient Current Technique (TCT) and Charge Collection Efficiency (CCE) measurements show a dependence of the bulk damage on the proton energy.

At a fluence of $\Phi_{eq} \approx 3 \times 10^{14}$ cm^{-2} oxygen-rich n-type diodes demonstrate clear Space Charge Sign Inversion (SCSI) after 23 MeV proton irradiation. This effect does not appear after the irradiation with 23 GeV protons. Moreover, RD50 pad diodes were irradiated with 23 MeV protons, electrically characterized and compared to results obtained after 23 GeV irradiations. Our previous observation on the energy dependence of the radiation damage could be confirmed. In order to get a deeper understanding of the differences of the radiation induced defects, the Deep Level Transient Spectroscopy (DLTS) and Thermally Stimulated Current Technique (TSC) were utilized. Defects with impact on the space charge could be identified and characterized and it was possible to find some hints for the reason of the SCSI after 23 MeV proton irradiation. Moreover, a dependence on the oxygen concentration of the sensors could be observed.

Kurzfassung

Es wurde die Strahlenschädigung von n-dotierten sauerstoffreichen Silizium-Flächendioden untersucht. Diese wurden im Rahmen der CMS-Tracker-Upgrade-Kampagne von Hamamatsu Photonics produziert und mit 23 GeV und 23 MeV Protonen im Fluenzbereich von einigen $\Phi_{eq} = 10^{11}$ cm^{2} bis $\Phi_{eq} = 1.5 \times 10^{15}$ cm^{-2} bestrahlt. Die induzierten Strahlenschäden wurden mit Hilfe von makroskopischen (CV-/IV-Charakteristiken und Transient Current Technique(TCT)) und mikroskopischen (Deep Level Transient Spectroscopy (DLTS) und Thermally Stimulated Current Technique (TSC)) Messmethoden charakterisiert. Somit konnte die strahleninduzierten Änderungen der effektiven Dotierungskonzentration bzw. der Verarmungsspannung, des Sperrstroms und der Ladungssammlung sowie die Defektkonzentrationen untersucht und verglichen werden.

Während sauerstoffreiche n-dotierte Silizium-Dioden nach einer Bestrahlung mit 23 GeV Protonen eine positive Raumladungsdichte behalten, ändert sich die effektive Raumladung sauerstoffreicher n-Typ Dioden nach 23 MeV Protonen Bestrahlung zu negativen Werten

und zeigt somit eine Inversion des Ladungsvorzeichens.
Mit Hilfe von mikroskopischen Messmethoden konnten Defekte mit Einfluss auf die Raumladung identifiziert und charakterisiert werden, auch wenn bis jetzt nur Mutmaßungen über den genauen Grund der Typeninversion angestellt werden können.

Contents

Chapter 1

Introduction

1.1 Motivation

The Large Hadron Collider (LHC) at CERN (European Organization for Nuclear Research) is the most powerful proton-proton accelerator in the world. The protons of both beams were accelerated in 2012 up to an energy of 4 TeV. The design energy of 7 TeV proton beams will be achieved in steps after the next shut down period. At four positions of the 26.7 km long ring the two beams are brought to collision and the reaction products are recorded by four large experiments: ATLAS, CMS, ALICE and LHCb. Among the general-purpose detectors ATLAS (A Toroidal LHC ApparatuS) and CMS (Compact Muon Solenoid) the later one is equipped with the largest silicon tracker ever built for high energy physics (HEP) experiment with an area of about 200 m^2. Beside the electromagnetic and hadronic calorimeter and the muon system, the tracker is one of the most important detector component. Due to the segmentation of the silicon sensors a high position resolution in the order of 10 μm can be achieved and therefore charged particles in a magnetic field of 3.8 T are tracked with high precision in order to determine their momenta, charges and reconstructed secondary vertices.

The future plan is to upgrade the LHC to the *High Luminosity* HL-LHC. The peak luminosity will be upgraded by a factor of 10 to 10^{35} $cm^{-2}s^{-1}$. This will lead to an increase of occupancy and fluence up to $\Phi_{eq} = 1.6 \times 10^{16}$ cm^{-2} during approximately 5 years of operation for the innermost pixel layer, located at a radius of R=4 cm from the interaction point . The existing tracker cannot withstand that high radiation. Therefore new silicon materials and new sensor designs have to be developed. The current tracker system will be replaced during the CMS phase 2 upgrade approximately in 2020. To tackle this challenge a tracker upgrade campaign (HPK campaign) was initiated in cooperation with the company Hamamatsu Photonics (Japan) of manufacturing the sensors. The requirements for the sensors were preliminary agreed an operating temperature of -20 °C, a maximum bias voltage of 500-600 V and a signal of about 10000 e^{-} ($\rightarrow$ 10 signal/noise ratio). Within the HPK campaign different silicon sensor materials in n- and p-type (Magnetic Chzochralski (MCz), Float Zone (FZ) and Epitaxial (Epi) silicon) in different thicknesses (FZ in 120, 200 and 300 μm; MCz in 200 μm; Epi in 50 and 100 μm) were analyzed for their radiation hardness. Both proton and neutron irradiations were performed to compare the electrical and charge collection properties of the sensors. One issue to find out about was if the radiation damage is dependent on the proton energy, which is the main topic of this thesis. The energy spectra of the particles expected as exposure to radiation for the tracker after the phase 2 upgrade were simulated by the CMS BRM [Gut12] group and shown as a so-called "lethargy"-plot (differential energy spectrum) in figure 1.1 for the most interesting radii of the pixel and strip regions in the tracker. The blue points represent the neutron spectra, the green points the pion and the red points the proton ones. The peaks of the pion and proton spectra are centered for both radii at a few hundred MeV to 1 GeV. The Z coordinate denotes the position along to the beam-pipe measured from the center of the detector. An increase of the energies is seen for increasing Z values.

1.2 Task Formulation

The purpose of this thesis is to perform a systematic study of the radiation damage caused by proton irradiations with two energies of 23 MeV and 23 GeV. Therefore MCz and FZ material of 200 μm thickness, with a high oxygen concentration were investigated. In previous studies oxygen-lean FZ sensors did not show a dependence of the proton energy. But due to the deep diffusion doping process with phosphorus at high temperatures and long duration, oxygen diffused from the SiO_2 passivation layer into the FZ bulk, which made the FZ sensors used in this work nearly as oxygen-rich as the MCz sensors.

Within this work the dark current and depletion voltage are investigated by means of CV/IV characteristics for different fluences and annealing times. Additionally, the charge collection properties are extracted with the Transient Current Technique (TCT) method for 660 nm laser light injection. With microscopic studies accomplished by the Deep Level Transient Spectroscopy (DLTS) and Thermally Stimulated Current (TSC) technique the differences in defect generation for 23 MeV and 23 GeV proton irradiation are determined.

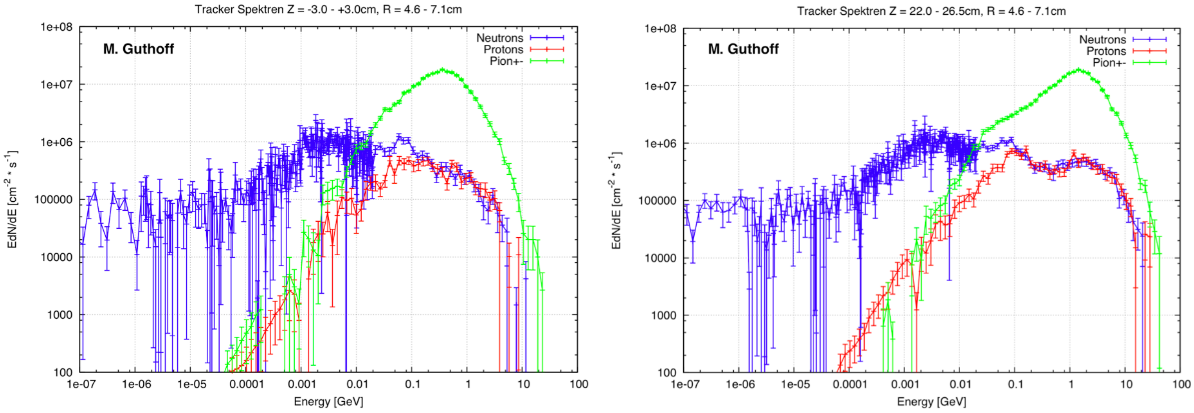

(a) R=4.6-7.1 cm, Z=-3-3 cm

(c) R=4.6-7.1 cm, Z=22-26.5 cm

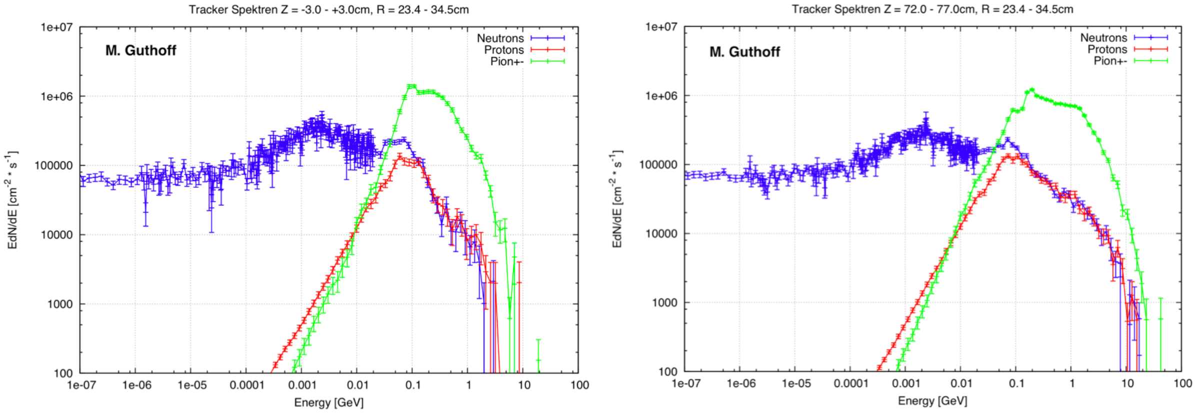

(b) R=23.4-34.5 cm, Z=-3-3 cm

(d) R=23.4-34.5 cm, Z=72-77 cm

Figure 1.1: Simulated energy spectra for neutrons, pions and protons for different radii R and Z-positions in the CMS tracker. The upper two figures describe the exposure to radiation for the pixel region and the two figures below for the strip region in the tracker. *Courtesy of the CMS BRM group*

Chapter 2

Basics of Silicon Crystals

2.1 Crystal Structure

Silicon is a Group IV semiconductor and possesses an electron configuration of 3s2 3p2. In other words 1s, 2s, 2p and 3s sub shells are completely filled while the 3p sub shell contains two electrons out of a possible six. All Group IV semiconductors crystallize in the diamond structure because of the tetrahedral bonding pattern of the s2p2 electrons around the atom, sharing electron-pair bonds to four adjacent atoms. These four outer electrons hybridize to form four sp3 molecular orbitals. These four electron clouds repel each other to equidistant tetrahedral spacing around the Si atom, attracted by the positive nucleus as shown in figure 2.1.

Every silicon atom has four nearest neighbors and is connected to them by covalent bonds. Two electrons may share an orbital if each has opposite spin quantum numbers (Pauli exclusion principle). Therefore an unpaired electron can share an orbital with an electron from another atom.

2.2 Band Structure

The relation between the energy and the momentum of the electrons in crystalline solids is reflected in the (electronic) band structure. For simplicity the lattice is usually described in the reciprocal momentum space, which is the Fourier transform of the spatial lattice. In that way it is possible to express the energy as a function of the momentum of the electrons. To calculate this relation the Schrödinger equation has to be solved:

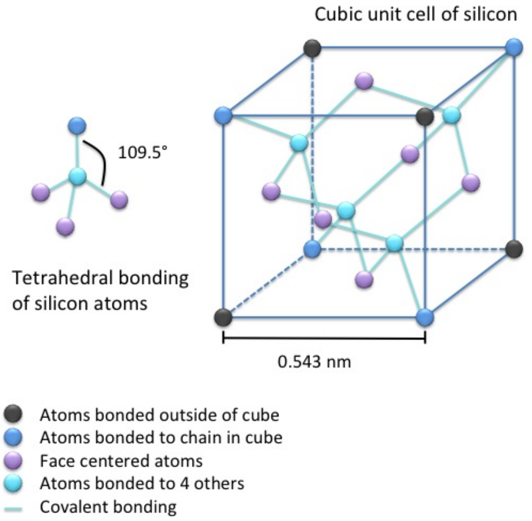

Figure 2.1: Diamond cubic crystal structure: four atoms (cyan) are bonded to four other atoms within the volume of the cell. Six atoms fall on the middle of each of the six cube faces (lilac), showing two bonds. The other two bond to adjacent cubes. Out of eight cube corners, four atoms bond to an atom within the cube (blue) and the other four bond to adjacent cubes of the crystal.

$$\left[-\frac{(\hbar)^2}{2m}\nabla^2 + V(\vec{r})\right]\Phi_{\vec{k}}(\vec{r}) = E_{\vec{k}}\Phi_{\vec{k}}(\vec{r}) \tag{2.1}$$

For a periodic lattice, thus a periodic potential $V(\vec{r})$ the solution of the Schrödinger equation is given by the Bloch wave function

$$\Phi_{\vec{k}}(\vec{r}) = e^{i\vec{k}\cdot\vec{r}}U_n(\vec{k},\vec{r}) \tag{2.2}$$

where U_n is the periodicity of the lattice $U_n(\vec{k},\vec{r})$ and n the band index.

Here, the Bloch theorem is used to describe the electrons as "nearly free". In this way, interactions between the electrons are completely ignored, while the electrons are affected by a periodic potential and have wave functions and energies which are periodic in wave vector $\vec{k}$ up to a constant phase shift between neighboring reciprocal lattice vectors. It follows that one just has to calculate the energy for a fixed band index to get the energy distribution of the first *Brillouin zone* (see figure 2.2a).

In figure 2.2b the allowed energy bands and forbidden ranges of energy for electrons are detected. E_V is called the valence band and is defined by the highest occupied energy

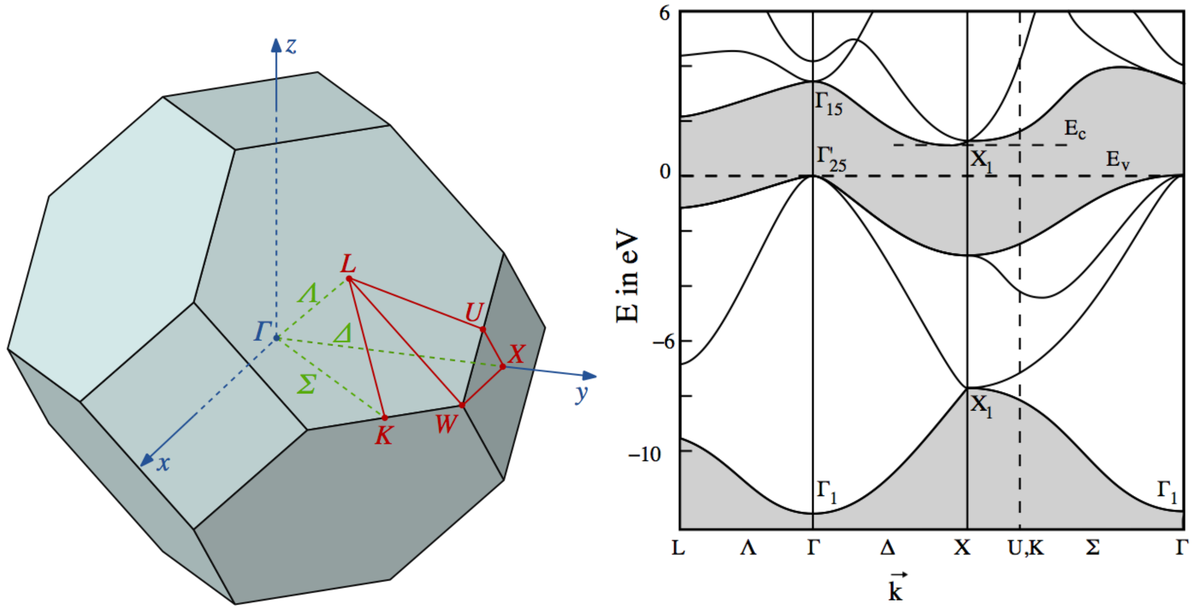

(a) (b)

Figure 2.2: (a) shows the *1. Brillouin zone* of a fcc lattice and the most important points of high symmetry [wiki1]. In (b) the band structure of silicon in the reciprocal space and the schematically representation of the valence and conduction band is shown [wiki2].

band at a temperature of zero Kelvin. The conduction band E_C is the next higher energy band and electrons in this band contribute to the conductivity of the semiconductor. The minimum of the conduction band and the maximum of the valence band are located at different points in the $\vec{k}$ space (X_1 and Γ_{25}). Thus, in order to be able to rise from the valence band to the conduction band, the electrons do not only need an activation energy of 1.12 eV at 300 K in Si, but also need momentum in terms of phonons (collective excitation of periodic arranged silicon atoms).

In this intrinsic semiconductor, the density of occupied levels in the conduction band is calculated by the integral over the density of states N(E) multiplied with the occupancy probability F(E):

$$n = \int_{E_C}^{\infty} N(E)F(E)dE. \tag{2.3}$$

E_C denotes the energy at the bottom of the conduction band, while the occupancy probability is given by the Fermi-Dirac distribution function $F(E)$:

$$F(E) = \frac{1}{1 + \exp\left(\frac{E-E_F}{k_B T}\right)} \tag{2.4}$$

which is given by the Fermi level E_F, the Boltzmann constant k_B and the temperature T. The concentration of electrons n and holes p is given by:

$$n = N_C \exp\left(-\frac{E_C - E_F}{k_B T}\right), \qquad p = N_V \exp\left(-\frac{E_F - E_V}{k_B T}\right) \tag{2.5}$$

with the density of states in the conduction band N_C and density of states in the valence band N_V. The Fermi level of an intrinsic semiconductor E$_i$ lies near of the middle the band gap and the intrinsic charge carrier concentration n_i:

$$E_i = \frac{E_C + E_V}{2} + \frac{k_B T}{2} \ln\left(\frac{N_V}{N_C}\right) \tag{2.6}$$

$$\Rightarrow np = n_i^2 = N_C N_V \exp\left(-\frac{E_g}{k_B T}\right) \tag{2.7}$$

with a width of the band gap of $E_g = E_C - E_V = 1.12$ eV (at 300 K).

2.3 Doping

By inserting impurities into the silicon lattice new shallow energy levels in the forbidden band gap are created and the semiconductor becomes extrinsic. By replacing a silicon atom with a phosphorus atom which is a Group V element the fifth electron is only weakly bound and released to the conduction band at room temperature. For that reason the phosphorus is left positively charged (donor), electrons are the free charge carriers and the silicon becomes n-type. By introducing a boron atom in a Si site of the lattice, it is similar. boron is a Group III element which needs an additional electron for the bonding. Therefore a hole is created in the valence band, the boron gets negatively charged, holes are the free charge carriers and the silicon becomes p-type. Another important influence of the variation of available electrons or holes in the crystal is the adjustment of E_F the fermi energy as shown in figure 2.3 for n-type silicon.

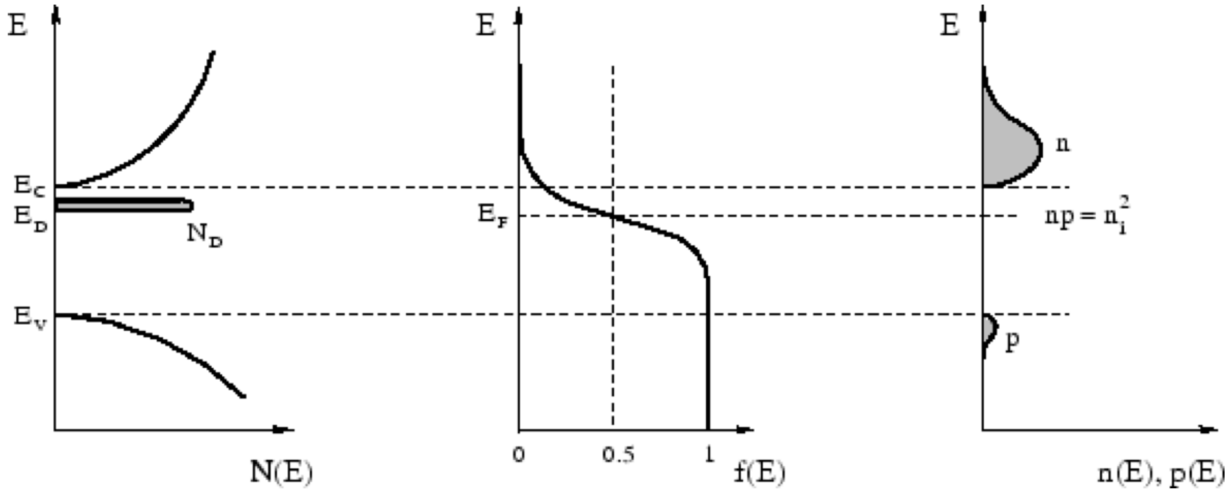

Figure 2.3: Density of states N_E, probability distribution $f(E)$, electron $n(E)$ and hole concentration $p(E)$ in an n-type semiconductor, taken from [Sze01].

Chapter 3

Silicon Diodes

Silicon is a highly abundant element on earth, but it occurs mostly as compounds like silicon dioxide (sand) or silicates. For high energy physic experiments only high resistivity mono-crystalline silicon is usable. In the following two of the most important techniques of production and growing mono-crystalline silicon are described.

3.1 Silicon Crystal Production Methods

3.1.1 Magnetic-Czochralski Silicon (MCz)

Magnetic-Czochralski silicon (MCz) is characterized by its production method. Mono-crystalline silicon is produced by the pull-from-melt method. A seed crystal drops into liquid melt of highly pure or doped silicon and gets pulled against gravity out of the melt held in a crucible. A schematic drawing of this technique is shown in figure 3.1. The orientation of the seed crystal determines the crystal orientation of the emerging mono-crystal. During the slow out-pulling of the top the silicon solidifies at the interface. This procedure is continued until the desired size is reached. The diameter of the crystal is determined by the pulling speed and the temperature of the melt. With this method it is unavoidable to introduce impurities like oxygen or carbon into the melt. To minimize this effect a strong horizontal or vertical magnetic field is applied. This permits a control of the convection fluid flow allowing to minimize the mixing between the liquid in the center with that at the edges. At the end the oxygen concentration amounts $(7-8)\cdot 10^{17}$ cm^{-3} and for carbon $2\cdot 10^{16}$ cm^{-3}.

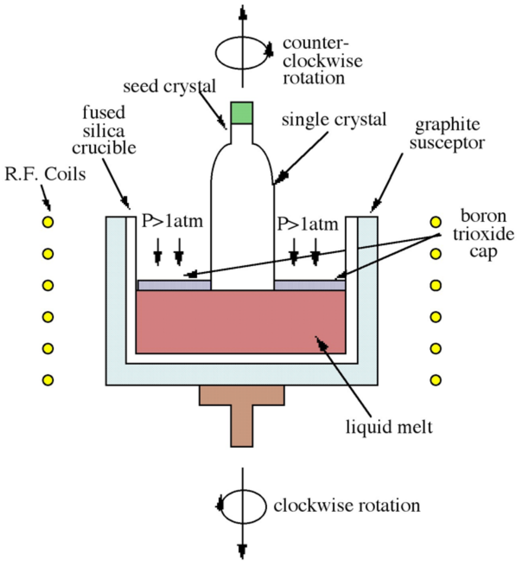

Figure 3.1: Schematically diagram of the Czochralski procedure, taken from [cnx12].

3.1.2 Float Zone Silicon (FZ)

Silicon grown by the float zone method is characterized by less impurity contamination than MCz silicon. The production chain starts with a rod of polycrystalline silicon. To achieve highly pure mono-crystalline silicon the segregation coefficient of the impurities is exploited. Therefore, a small zone of the boule is homogeneously melted with induction heating during a slow rotation. Than, the impurity atoms diffuse to the liquid part. The low impurity solidifies in the leftover regions. The boule can grow as a perfect single crystal if a seed crystal is placed at the base to initiate a chosen direction of crystal growth. The impure end of the boule is cut off, and the purification is repeated. Thus, a single crystal rod of a diameter of 150 mm can be grown. But because of the radial temperature profile during the zone melting process, FZ may exhibit a radial non-uniformity in the impurity concentration and resistivity distribution.

3.2 Electrical Properties of Silicon Diodes

Planar pad diodes are used in this work to investigate the radiation damage of the silicon caused by irradiation. A p^+-n-n^+ diode consists of a n-type (donor doped) bulk with a layer of highly doped p^+-type (acceptor doped) silicon on top and a thin layer of highly doped n^+-type silicon on the back. A schematic drawing is shown in figure 3.2. The guard ring (GR) and pad are in this work always kept on the same potential in order to limit the volume to the pad area and therefore avoid additional currents from the sensor's edges. In the following, the description of the electrical properties of the sensors is called macroscopic.

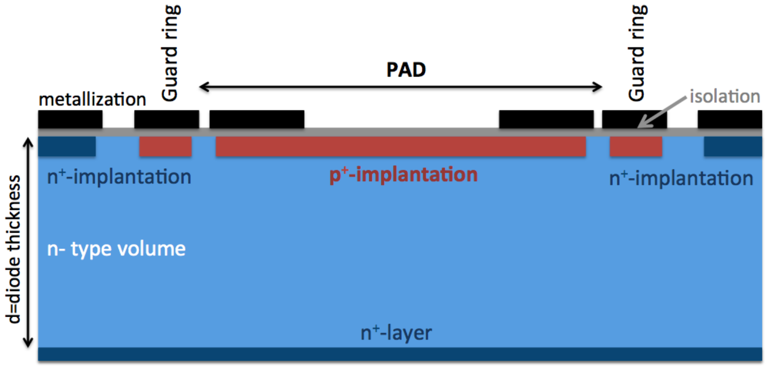

Figure 3.2: Schematic drawing of a n-type planar silicon pad diode. In the following the p$^+$ implantation of the diode defines the front and the n$^+$ layer defines the back of the sensors.

3.2.1 Junction

When n- and p-doped silicon get in contact, a depletion zone forms at the interface. This is due to the fact that electrons diffuse into the p-doped region and holes in the n-doped region and recombine. In that way, the n-type region becomes partly depleted from electrons and the p-type on holes, thus just the ionized positive donors on the n-type side and ionized negative acceptors on the p-type side are left. Because of the charged ionized donors and acceptors, an electric field builds up and creates a potential difference and thus a so called "built-in" voltage U_{bi}, which corresponds to the difference of the Fermi level in the n- and p-type region. This stops the charge carrier diffusion in the p-n region. To increase the depletion zone (also called space charge region (SCR)) through the whole volume one has to apply a voltage in reverse direction. The electric field strength E, the potential Φ and the width of the depletion zone W can be calculated from the solution of the Poisson equation with the assumptions that the free charge carrier density vanishes in the depletion region and the space charge density ρ_{el} is homogeneous over $0 < x < W$.

$$-\frac{d^2\Phi(x)}{dx^2} = \frac{\rho_{el}}{\epsilon\epsilon_0} = \frac{q_0 N_{eff}}{\epsilon\epsilon_0} \tag{3.1}$$

where ϵ_0 is the vacuum permittivity, $\epsilon = 11.9$ the relative permittivity of silicon, $N_{eff} = N_D - N_A$ the effective doping concentration given by the concentration of donors N_D and acceptors

N$_A$ and the elementary charge q_0.
From the Poisson equation it follows that $W(U)$ is given by

$$W(U) = \sqrt{\frac{2\epsilon\epsilon_0}{q_0\,|N_{eff}|} \cdot (U + U_{bi})}. \tag{3.2}$$

for W smaller or equal to the sensor thickness d. For a certain voltage U$_{dpl}$ the whole sensor is depleted ($W = d$) and the effective doping concentration is given by

$$|N_{eff}| = (U_{dpl} + U_{bi})\frac{2\epsilon\epsilon_0}{q_0 d^2}. \tag{3.3}$$

In the following, the assumption that $U_{bi} \approx 0.5V \ll U_{dpl}$ is made to simplify the relation to

$$|N_{eff}| = \frac{2\epsilon\epsilon_0}{q_0 d^2} \cdot U_{dpl}. \tag{3.4}$$

Because the depleted region of the p$^+$-n-n$^+$ planar diode can be treated like an insulator, one gets for the depletion capacitance

$$C(U) = \frac{\mathrm{d}Q}{\mathrm{d}W}\frac{\mathrm{d}W}{\mathrm{d}U} \tag{3.5}$$

with the space charge Q, the active area of the diode A and d$Q = q_0 N_{eff} A$dW. By simple inserting of equation 3.2 into equation 5.2c it follows that

$$C(U) = \epsilon\epsilon_0\frac{A}{W(U)}, \qquad U < U_{dpl} \tag{3.6}$$

That is the expression for a parallel plate capacitor with the thickness of $W(U)$. For a silicon diode the capacitance decreases with the increase of the depleted region until the full depletion is reached. At that point $W = d$ and the capacitance remains constant with increasing bias voltage:

$$C_{end} = \frac{\epsilon\epsilon_0 A}{d}, \qquad U \geq U_{dpl} \tag{3.7}$$

3.3 Devices used in this Work

In this section the used devices, their specifications and their labeling are presented. Some diodes are produced by Hamamatsu[1] within the framework of the CMS tracker upgrade campaign (”HPK campaign”). For comparison RD50[2] diodes produced by Okmetic[3] and processed by CiS[4] are investigated. This comparison was assumed to be necessary because in previous studies differences in materials were observed [Jun11]. The producers quote a sensor thickness of 200 μm and 230 μm for Hamamatsu and CiS diodes, respectively. However, the active volume varies. Thus the thickness for all devices are calculated via equation 3.7 and can be found in table 3.1, 3.2 and 3.3. All diodes from Hamamatsu provide a pad area A of 25 mm^2, while the RD50 diodes are smaller (A = 6.25 mm^2). Additionally, the initial doping concentrations $N_{eff,0}$ (via the equation 3.4) and the bulk resistivity $\rho = (q_0 \mu_n N_{eff,0})^{-1}$, with the elementary charge q_0 and the mobility of electrons in silicon (for n-type) $\mu_n = 1.45 \times 10^3$ cm^2/Vs, are calculated. Both can be found for the devices used in this work in the following tables.

Material	Labelling	Thickness d [μm]	N$_{eff,0}$ [10^{12} cm^{-3}]	Bulk resistivity ρ [kΩcm]
MCz	MCZ200N_03_DiodeL_8	201	4.38	0.982
MCz	MCZ200N_11_DiodeL_3	203	4.48	0.923
MCz	MCZ200N_03_DiodeL_11	201	4.42	0.996
MCz	MCZ200N_05_DiodeL_9	199	4.63	0.929
MCz	MCZ200N_10_DiodeL_11	202	4.39	0.979
MCz	MCZ200N_11_DiodeL_5	199	4.63	0.928
FZ	FZ200N_05_DiodeL_9	226	2.17	1.971
FZ	FZ200N_04_DiodeL_8	225	2.19	1.966

Table 3.1: Properties of HPK silicon n-type materials used in this work. $N_{eff,0}$ denotes the original doping concentration and ρ the resistivity. Materials used for irradiation with 23 GeV protons.

Important parameters of silicon diodes are the oxygen and carbon concentrations, since both have an impact on the defect generation and recombination. From the Secondary Ion Mass Spectroscopy (SIMS) measurements done at ITE[5] a 10 times higher oxygen

---

[1] Hamamatsu Photonics, Japan

[2] RD50 - Development of Radiation Hard Semiconductor Devices for High Luminosity Colliders

[3] Forschungsinstitut für Mikrosensorik und Photovoltaik GmbH, Erfurt (Germany)

[4] Okmetic Headquarters, Vantaa (Finland)

[5] Institute of Electronic Materials Technology, Warsaw (Poland)

Material	Labelling	Thickness d [μm]	N$_{eff,0}$ [10^{12} cm^{-3}]	Bulk resistivity ρ [kΩcm]
MCz	MCZ200N_09_DiodeL_5	202	4.71	0.961
MCz	MCZ200N_03_DiodeL_5	202	4.48	0.915
MCz	MCZ200N_04_DiodeL_5	202	4.7	0.940
MCz	MCZ200N_09_DiodeL_3	202	4.58	0.940
MCz	MCZ200N_01_Diode_01	202	4.58	0.940
FZ	FZ200N_01_DiodeL_9	225	2.19	1.966
FZ	FZ200N_03_DiodeL_2	223	2.24	1.918
FZ	FZ200N_04_DiodeL_11	225	2.20	1.959
FZ	FZ200N_01_DiodeL_11	224	2.21	1.951

Table 3.2: Properties of HPK silicon n-type materials used in this work. $N_{eff,0}$ denotes the original doping concentration and ρ the resistivity. Materials used for irradiation with 23 MeV protons.

Material	Labelling	Thickness d [μm]	N$_{eff,0}$ [10^{12} cm^{-3}]	Bulk resistivity ρ [kΩcm]
MCz	8556-02-31-1	229	3.99	1.076
MCz	8556-02-31-2	229	4.124	1.043
MCz	8556-02-31-3	229	4.033	1.067
MCz	8556-02-31-4	229	4.070	1.057

Table 3.3: Properties of RD50 silicon n-type materials used in this work. $N_{eff,0}$ denotes the original doping concentration and ρ the resistivity. Materials used for irradiation with 23 MeV protons.

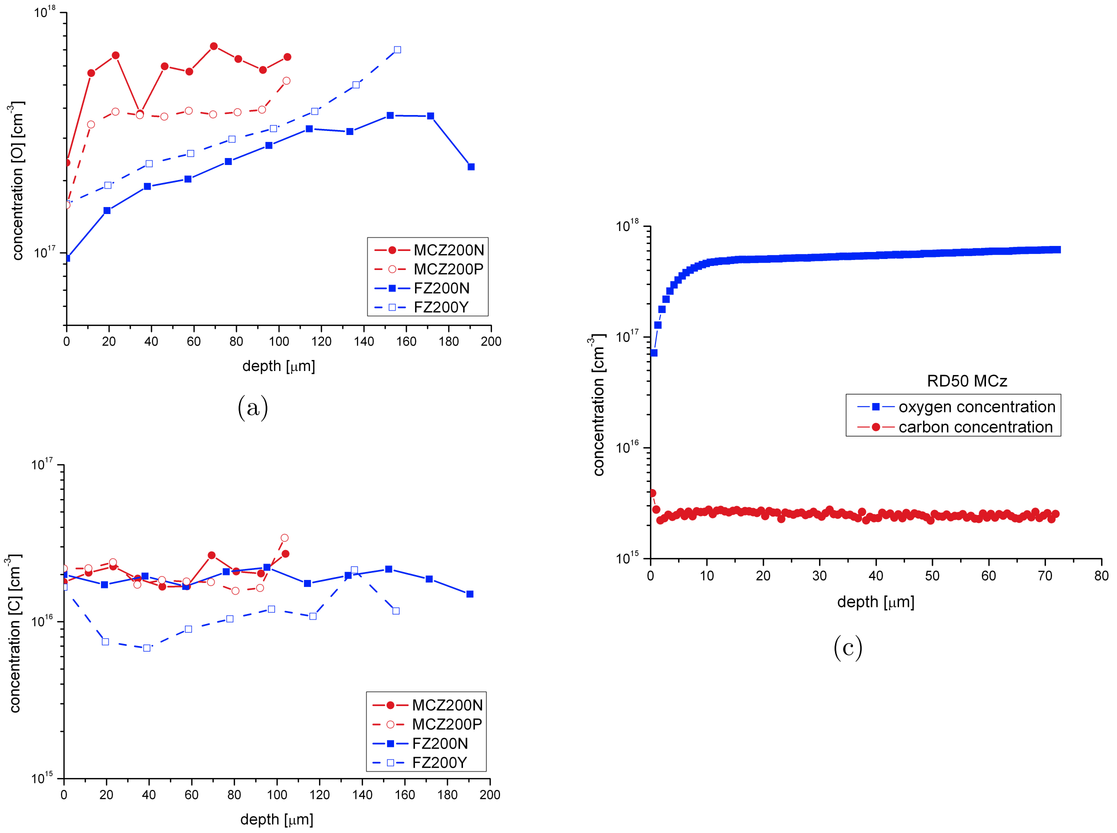

(a)

(b)

(c)

Figure 3.3: SIMS measurements of the oxygen (a) and carbon (b) concentration for MCZ and FZ materials . The oxygen concentrations for MCz lie around 5×10^{17} cm^{-3} and for FZ 3×10^{17} cm^{-3}. The oxygen and carbon concentration of RD50 MCz material from CiS is shown in (c) as a function of the depth.

concentration than usual for Float Zone materials could be observed in FZ200 n- and p-type diodes from Hamamatsu, see figure 3.3a. The origin of this unexpected high oxygen content could arise from the *deep diffusion* process, see figure 3.4. Within this process a highly doped n^+/p^+ layer is deposited on the back of the sensor and then heated up, during the heating procedure the dopants diffuse from the back side into the whole volume. In this way a non-homogeneous distribution of donors or acceptors is created in the sensor volume (see [Jun11]), which results in a non-uniformity of the effective doping and oxygen concentration. Therefore, the active volume is poorly defined.

For the RD50 diodes the doping is done by the standard process. This method produce the ohmic contact on the back and front with the implantation of n^+ or p^+ layers. The border between low and high doped material on the back of the sensor is sharp, therefore the active volume is well defined, the doping and oxygen content are homogeneous. The depth profile of the oxygen and carbon concentration is presented in figure 3.3c.

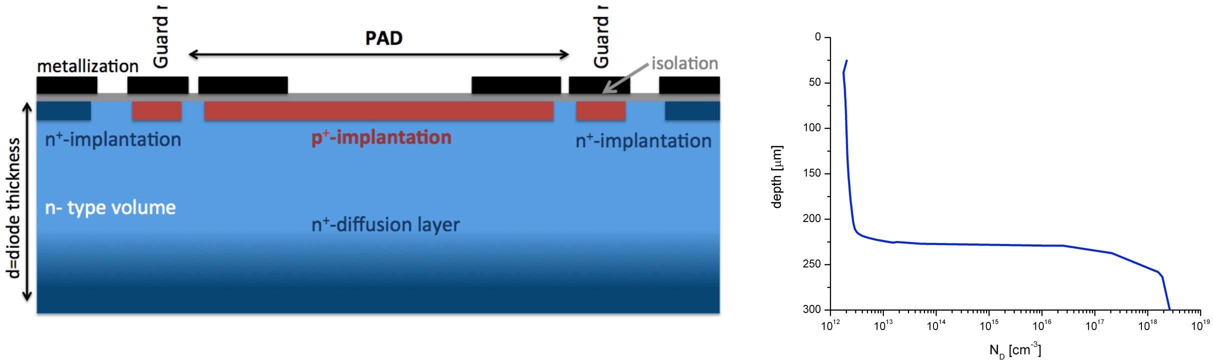

(a) (b)

Figure 3.4: Schematic drawing of the structure of a deep diffused planar pad diode (a) and the resulting donor concentration as a function of the depth (b).

Chapter 4

Radiation induced Defects in Silicon

Not only impurities generate new energy levels in the band gap, also radiation-induced microscopic defects like lattice distortions. The radiation-induced damage can be divided into surface and bulk damage. The surface damage is caused by ionization effects in the SiO_2 surface layer and the Si-SiO_2 interface leading to so-called fixed oxide charges and interface traps, respectively. In high energy physic (HEP) experiments silicon tracking detectors are located close to the interaction point where the radiation dose is highest and the limiting factor of the lifetime of these detectors is the bulk damage produced by displacements of silicon atoms. These defects can be further differentiated as point and cluster defects. In the following, the mechanisms of defect generation, formation and classification are described.

4.1 Generation of Defects

Hadrons like protons, neutrons and pions or high energetic leptons create bulk damage by producing primary knock-on atoms (PKA) which migrate through the crystal as an interstitial and leaves a vacancy this is called a Frenkel pair, see figure 4.1a. The displacement threshold in recoil energy is $E_R = 21$ eV [Akk01]. If the energy of the PKA is much higher than that, a displacement cascade can be formed. A possible path of a recoil atom of secondary displaced atoms with $E_R = 50$ keV is shown in figure 4.1b. One can see cluster formation at the end of the path, where the density of vacancies and interstitials is very high. This simulation shows a production of nearly 1000 Frenkel pairs. But the vacancies and interstitials also recombine with each other if their distance is smaller than a few lattice constants. 60 % of the Frenkel pairs recombine [Wun92] and the others migrate through the lattice and perform reactions with each other or impurity atoms and create so-called point defects.

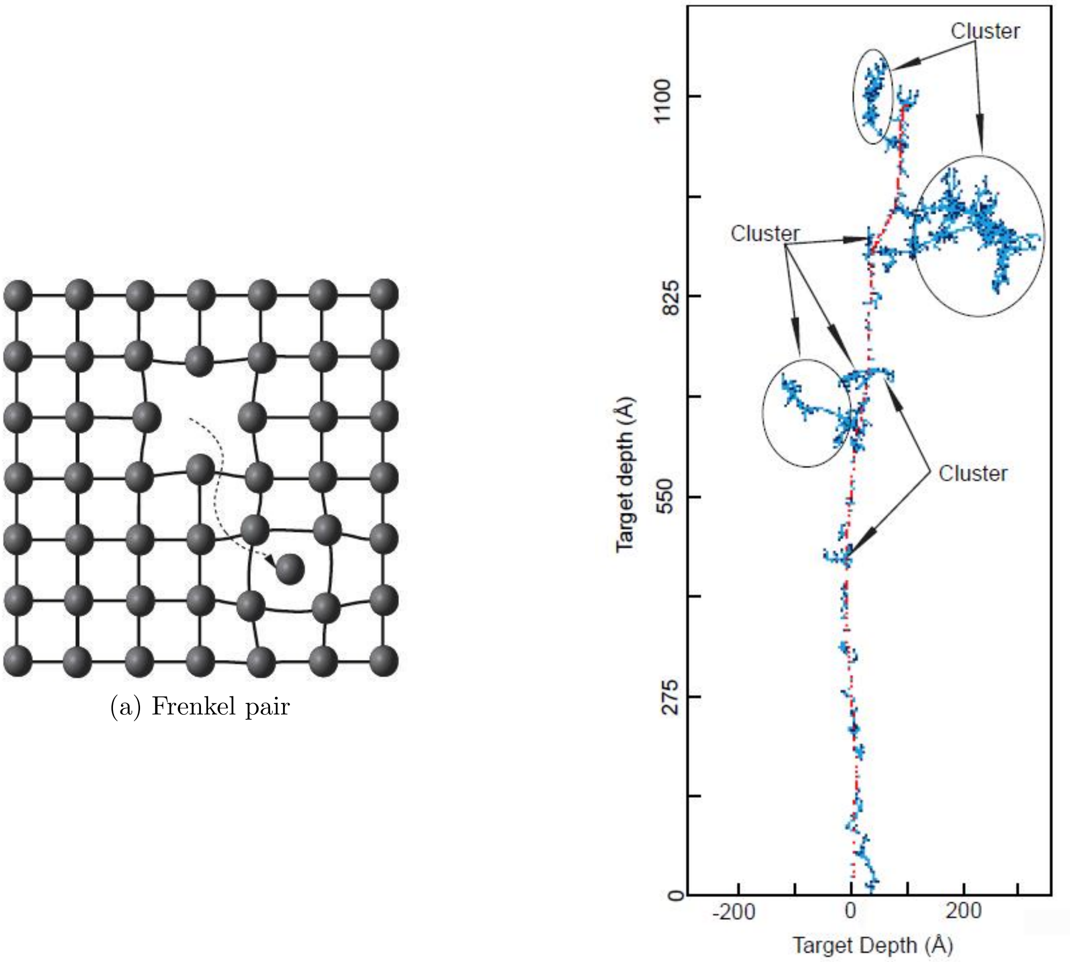

(a) Frenkel pair

(b) Damage cascade

Figure 4.1: Illustration of a Frenkel-pair (a) and TRIM simulation of a damage cascade with PKA of $E_R = 50$ keV, which is the average kinetic energy of a PKA of 1 MeV neutron. Taken from [Jun11].

4.2 NIEL scaling Hypothesis

The defect generation is dependent on the particle type and the particle energy. While neutrons can only interact with the nucleus, charged hadrons mainly interact via Coulomb scattering. For comparison of radiation damage effects it is commonly assumed that the damage parameters as a function of fluence are independent of particle type and energy if the fluences are normalized to the Non-Ionizing Energy Loss (NIEL). The NIEL is a quantity to describe the rate of energy loss due to atomic displacements of particles traversing a material. It is a valuable tool to compare the radiation damage produced by different particles and different energies with the damage of 1 MeV neutrons by scaling the fluences. But the assumption that the damage parameters are independent on the particle type and energy is not without controversy. Furthermore their is no explanation at the microscopic level [Huh02].

The Non-Ionizing Energy Loss is sometimes described by the displacement damage function $D(E)$, which is related to the NIEL by

$$\mathrm{NIEL}(E) = \frac{N_A}{A} D(E) \tag{4.1}$$

with the Avogardo constant N_A and the atomic mass of the target atoms A. The displacement damage function describes the amount of displacements as a function of the energy of the incoming particle:

$$D(E) := \sum_{\nu} \sigma_\nu(E) \int_{E_d}^{E_R^{max}} f_\nu(E, E_R) P(E_R) dE_R \tag{4.2}$$

where σ_ν is the corresponding cross section to reaction ν, f_ν gives the probability to generate a PKA with a specific recoil energy by a particle with energy E and the Lindhard partition function $P(E_R)$ [Laz87] which described the fraction of recoil energy that is deposited in displacements.

In the frame of this work the radiation damage induced by 23 MeV and 23 GeV protons is of main interest and, therefore, the NIEL scaling for proton damage at these energies. According to [Jun03] for proton energies below about 10 MeV the production of displacement atoms from the lattice site is mainly caused by Coulomb scattering. While at energies above 30-50 MeV nuclear interactions (elastic and non-elastic reactions) are mostly responsible for the displacements. For 23 MeV the creation of displacements is due to both Coulomb scattering and nuclear interactions with about the same contribution of 3×10^{-3} MeV cm^2/g to the NIEL of 6×10^{-3} MeV cm^2/g. On the other hand at

23 GeV the non-elastic processes become dominant for the displacement damage. The corresponding extrapolated NIEL value is about 1×10^{-3} MeV cm^2/g. For a comparison of the damage parameters in silicon detectors one has to keep in mind that the NIEL gives only the total number of displaced atoms, i.e. the number of created vacancies and interstitial atoms. Figure 4.2 [Huh02] presents simulation results for the initial distribution of vacancies produced by 10 MeV and 23 GeV protons and 1 MeV neutrons, in a volume of 1 μm^3 after exposure to a fluence 10^{14} cm^{-2}. As one can see, for 10 MeV the distribution of vacancies is quite uniform with only a few dense regions (clusters). Contrary to 1 MeV neutrons which produce mainly isolated dense vacancy clusters. The 23 GeV protons form an intermediate case between these two.
It has to be mentioned that in these simulation results —and in general in the NIEL— the recombination of the created vacancy-interstitial pairs and the final evolution of these primary defects into stable defects is not taken into account.
Nevertheless, it is expected that for 23 MeV protons the probability for the creation of point defects is much larger compared to 23 GeV protons which produce, due to the dominant nuclear interactions, more cluster defects and only some point defects.

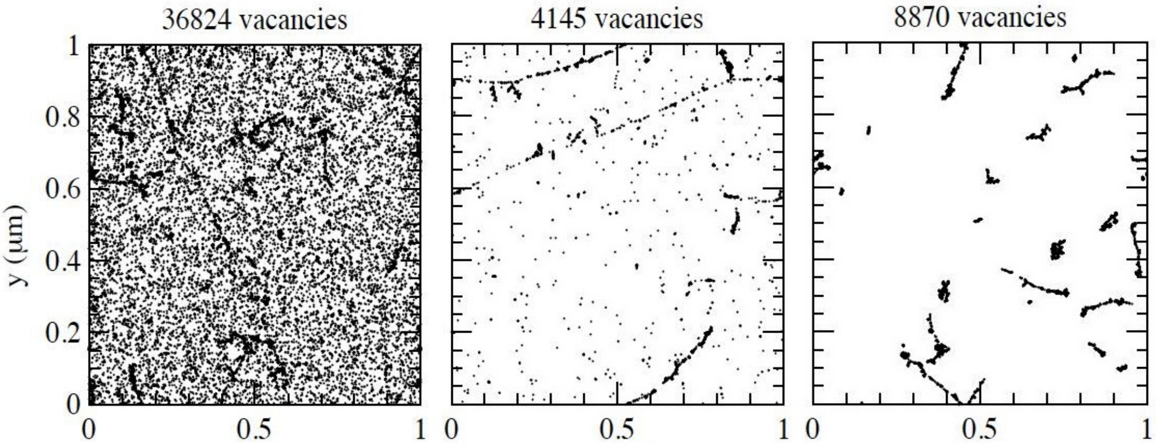

(a) (b) (c)

Figure 4.2: Simulations of the distributions of vacancies by 10 MeV protons (a), 24 GeV protons (b), and 1 MeV neutrons (c), for a fluence of $1 \cdot 10^{14}$ cm^{-2} in a cube of 1 μm^3. [Huh02]

4.2.1 Hardness Factors

To compare the damage efficiency of different radiation fields the displacement-damage cross section of a certain particle type with a certain energy spectrum is normalized to that of mono-energetic neutrons of 1 MeV. The resulting factor is called the *hardness factor* κ.

$$\kappa = \frac{\int D(E)\Phi(E)dE}{D(E_n = 1MeV)\int \Phi(E)dE} \tag{4.3}$$

This factor can then be used to calculate the 1 MeV neutron equivalent fluence for any particle and energy by the following formula.

$$\Phi_{eq} = \kappa \cdot \Phi \tag{4.4}$$

In table 4.1 the hardness factors of the used proton irradiations are shown. Further details on how to determine the hardness factors experimentally can be found in chapter 5.2. of [Mol99].

Table 4.1: Hardness factors of the used proton irradiations.

Particle energy	Hardness factor
23 MeV	2.0 [Die10]
23 GeV	0.62 [Lin01]

4.3 Classification of Defects

As already mentioned, two different types of defects are created, cluster and point defects. This classification describes single- and di- interstitials and -vacancies combined with impurities as point defects and on the other hand as large agglomerations of defects in a small volume of (15-20 nm)^3 with 10^5 to 10^6 included atoms per cm^3 [Gos59].

4.3.1 Point Defects

Point defects can originate from the fabrication process, from the doping (phosphorus and boron) or from irradiation like the vacancy-oxygen (VO) defect. Some of these defects are electrically active and have an energy level in the band gap. They are able to capture and emit charge carriers and can be classified correspondingly as neutral or charged. The activation energy ΔE_a which is needed to excite an electron from the energy level E_t to the conduction band E_C is given by $\Delta E_a = E_C - E_t$ for defect level in the upper half of the band gap. For defects in the lower part the energy needed to emit a hole into the valence band is $\Delta E_a = E_t - E_V$. In that way, donors are defined to be neutral if occupied by an electron and positively charged if empty, while it is the other way around for acceptors. The charge states of the defects depend of course on the Fermi-level. Another species of defects are the amphoteric defects which have two or more levels, e. g. with one acting as donor and the others as acceptors. One example of this is the di-vacancy V_2 with charge stages $V_2^{(+/0)}$, $V_2^{(-/0)}$ and $V_2^{(=/-)}$.

However, not every donor/acceptor contributes to the effective doping concentration of the sensor. Only defects which are ionized in the space charge region have an impact on this important property of the sensor.

It has to be noted that defects can be ”filled” either by electrons or holes dependent on wether they are donors or acceptors. In n-type material traps in the upper half of the band gap below the Fermi-level are filled by electrons and are so-called electron traps. For p-type material energy levels in that part of the band gap are occupied by holes and are so-called hole traps.

4.3.2 Cluster Defects

Cluster defects are highly complicated damage structures and hard to characterize. As mentioned before high energy particles produce displacement cascades ending in disordered regions or so-called terminal clusters with a high density of vacancies and interstitials. Most of the created vacancies and interstitials recombine, but the remaining vacancies and interstitials can form higher order vacancy-related defects or interstitial-related defects. These so-called cluster-related defects appear to be very similar to that of point defects but with specific distortions [Gil97], [Sve91]. The impact of such cluster-related defects on the macroscopic properties of silicon sensors was recently revealed by [Pin08] and [Jun11].

4.3.3 Occupation of Traps

The electron occupation probability of defect states with an energy of E_t can be described by the Fermi-Dirac distribution function in case of thermal equilibrium

$$F(E_t) = \frac{1}{1+\exp\left(\frac{E_t-E_F}{k_B T}\right)}. \tag{4.5}$$

With equation 4.5 it is possible to calculate the fraction of donors/acceptors occupied by electrons (n_t)/holes (p_t)

$$n_t = N_t \cdot F(E_t) \tag{4.6}$$

$$p_t = N_t \cdot (1 - F(E_t)) \tag{4.7}$$

for a total defect concentration N$_t$ with an energy E$_t$ of $N_t = n_t + p_t$. Because an occupied acceptor contributes with negative space charge to the effective doping concentration N$_{eff}$, the occupation of defects has to be taken into account for the calculation of N$_{eff}$.
The occupation of traps in the band gap is determined by the interaction of the defect level with the conduction and valence band. These processes can be described statistically by the Shockley-Read-Hall statistic [Sho52][Hal52]. Where the proportionality of the capture rates for electrons (holes) of the conduction (valence) band to the fraction of occupied defect states and concentration of free charge carriers can be given by emission rates $e_{n,p}$ and capture coefficients $c_{n,p}$ for electrons (n) and holes (p). The relation between $e_{n,p}$ and $c_{n,p}$ is given by

$$e_{n,p} = c_{n,p} N_{C,V} \exp\left(\pm \frac{E_t - E_{C,V}}{k_B T}\right) \text{ [Sze01].} \tag{4.8}$$

4.3.4 Occupation under Reverse Bias

With an applied reverse bias a space charge region builds up. In this region the free charge carrier concentration is approximately zero due to the electric field. The capturing of charge carriers is impossible for the traps and the occupation becomes a function of the emission coefficients for electrons e_n and holes e_p

$$n_t = N_t \cdot \frac{e_p}{e_n + e_p} \tag{4.9}$$

$$p_t = N_t \cdot \frac{e_n}{e_n + e_p} \tag{4.10}$$

4.3.5 Occupation under Forward Bias

For both microscopic measurement methods Deep Level Transient Spectroscopy and Thermally Stimulated Current Technique (see section 8) an applied forward bias (voltage in forward direction) injects a high concentration of electrons and holes to fill the defects inside the diode at low temperatures like 10 K. Here it is very important to understand the conditions of this "filling". By injecting a high number of free carriers into the silicon bulk, the emission rates of the traps become much smaller than the capture rates. Therefore, the steady state occupation for electron and hole traps is given by

$$n_t = N_t \frac{1}{1 + \frac{c_p p}{c_n n}}, \qquad p_t = N_t \frac{1}{1 + \frac{c_n n}{c_p p}} \tag{4.11}$$

with the capture coefficients for electrons c_n and holes c_p and the concentration of electrons n and holes p.
That means that defects can get filled by electrons when the capture coefficient for electrons is higher than for holes and for the filling with holes the other way around (see [Mol99]).

4.4 Poole-Frenkel Effect

Donor states in the upper half of the band gap become positively charged by emitting an electron. This electron has to overcome a potential barrier, which can be lowered by an external electric field E_e. This is the same for acceptors in the lower half of the band gap emitting holes and getting negatively charged. This effect is named after Yakow Frenkel and Horace Hewitt Poole and was published in 1938 [Fre38]. The change of the activation energy, e.g. for a donor can be calculated by

$$\Delta E = \sqrt{\frac{q_0^3 E_e}{\pi \epsilon_0 \epsilon}}. \tag{4.12}$$

An other important defect parameter is affected by that; the emission rate of electrons e_n or holes e_p of the defect level, taken from [Har68], is given as

$$e_{n,p}^{PF} = e_{n,p}^0 (1/\gamma^2)[1 + (\gamma - 1)e^{\gamma}] + 1/2 \tag{4.13}$$

where $\gamma = \sqrt{\frac{q_0 F}{\pi \epsilon_0 \epsilon}} \cdot \frac{q_0}{k_B T}$ is a function of the emission rate without an applied electric field $e_{n,p}^0$, the electric field F and the temperature T. Under the assumption of a temperature-independent cross section $\sigma_{n,p}$, $e_{n,p}^0$ is given by

$$e_{n,p}^0 = \sigma_{n,p} \nu_{th,n,p} N_{C,V} \exp\left(-\frac{E_a}{k_B T}\right) \tag{4.14}$$

with the thermal velocity of electrons/holes near the edges of the conduction/valence band $\nu_{th,n,p}$ (compare equation 4.8). The consequence of this influence of an electric field inside the sensor on the emission of charge carriers can be observed by the TCS method (see chapter 8).

4.5 Defect Annealing

Defects change under heat treatment. The CMS tracker operates at -10 °C, but during shut down periods it is getting heated up to room temperature. Therefore, it is important to know how the sensors react to that temperature difference. Defects become mobile at a certain temperature and *migrate*, *react with sinks* or *dissociate*. The most simple defects vacancies (V) and interstitials (I) are mobile at room temperature, more complicated structures like the di-vacancy (V_2) become mobile at temperatures between 250 °C and 300 °C. By thermal excitation defects can migrate through the silicon lattice and can recombine with their counterparts $V + I \to Si$ or form new defects with e. g. a carbon substitutional C_s to $I + C_s \to C_i + Si$ and than $C_i + O_i \to C_iO_i$. An other possibility is that defect complexes dissociate into their components $C_iO_i \to C_i + O_i$. For a detailed description of the annealing reaction kinetics see [Mol99] (chapter 3.5).

In this work annealing studies are performed isothermally, which means that the annealing temperature stays constant while the annealing time increases. Thus it is possible to get a complete picture of the defect evolution at that temperature (80 °C).

The standard procedure of the HPK campaign uses annealing steps at different temperatures to decrease the needed annealing time. The scaling of the annealing refers to the accelerating factors for the short term annealing of [Mol99]. Thus a factor of 8.6 is obtained for the annealing between 60 °C and 80 °C.

Step	Temperature [°C]	Time [min]	Accumulated time @80°C [min]
1	60	10	1.2
2	60	10	2.3
3	60	20	4.7
4	60	50	10.5
5	60	76	19.3
6	80	15	34.3
7	80	30	64.3
8	80	60	124.3

Table 4.2: Guideline of annealing steps as agreed on within the HPK campaign.

4.6 Irradiation Facilities

The proton irradiations with different particle energies were performed at two different facilities.

4.6.1 23 MeV Protons

In Karlsruhe (Germany) it was possible to irradiate with 23 MeV protons with the Karlsruhe Proton Cyclotron KAZ. It is operated by the Zyklotron AG (ZAG), while the Karlsruhe Institute of Technology (KIT) is a customer of this facility. The proton energy at extraction is 25.3 MeV and the typical proton current is 1.5 μA. After passing several materials the proton energy amounts to 23 MeV. The temperature in the box where the samples are located is approximately -40 °C, which provides negligible annealing during irradiation. The beam spot size is approximately 7 mm. The typical proton flux is $2.5 \cdot 10^{13}$ p/(s·cm^2), this makes it difficult to achieve low fluences. The lowest fluence which could be provided was $\Phi \approx 1.5 \cdot 10^{13}$ p/cm^2. For dosimetry, Nickel foils are used and the induced activity of the Ni-57 isotope is measured. The error of the fluence is given as 20 % [Die10].

4.6.2 23 GeV Protons

The irradiations with 23 GeV protons are performed at the Proton Synchrotron (PS) at CERN, the European Organization for Nuclear Research in Geneva. Because of the beam sharing with other experiments at the PS, there are one to three spills per cycle for the IRRD-1 at the PS-T7 beam line available. The proton flux of one spill amounts to $3 - 9 \cdot 10^9$ p/(s·cm^2), thus 50 spills deliver the minimum fluence of 1.5×10^{11} p/cm^2. The samples are placed in cardboards of 5x5 cm^2 and are scanned by the proton beam over an area of 2x2 cm^2. The irradiation temperature was around 27 °C. For the higher fluences several days are needed (for $\Phi = Flux \cdot t = 1 \cdot 10^{15}$ p/cm^2, $t = 3 \cdot 10^5$ s= 4 days), which causes annealing effects already during the irradiation. The dosimetry is done by measurements of the activity of Na-22 and Na-24 in 5x5 cm^{-2} aluminum foils. With this method, the fluence error is given by ±7 %.

Chapter 5

Influence of Defects on Macroscopic Properties

Defects created by the manufacturing process or by irradiation can affect the macroscopic properties of Si sensors. The main effects as shown in figure 5.1 are the creation of shallow dopants that affect the space charge (SC), deep levels that increase trapping and deep levels that increase the dark current and therefore the noise.

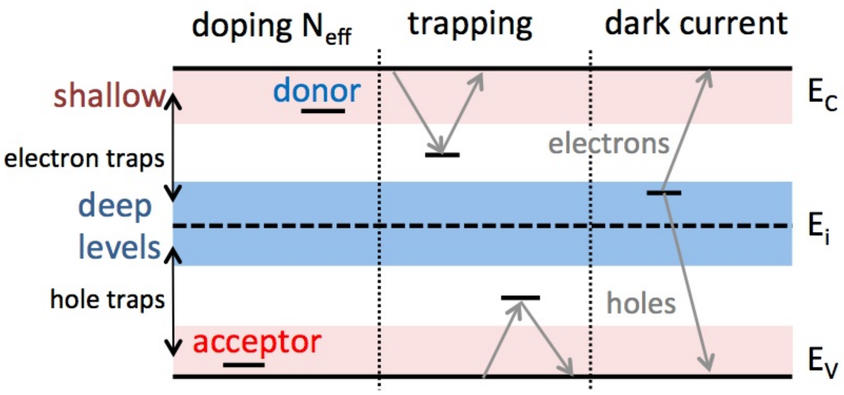

Figure 5.1: Position of defect levels in the band gap and their influence on the electrical properties of Si sensors (see [Jun11]).

5.1 Change of N_{eff} - *Shallow Levels*

Like the dopants (for example boron and phosphorus), defects introduced during irradiation can introduce energy levels near the valence band (VB) or conduction band (CB).

If these defect levels are ionized at room temperature they are electrically active and affect the SC and the *effective doping concentration*, respectively. Most of these defects are point defects related to impurities, thus the type of the material has a big influence on the operation of the sensor during and after irradiation. In case acceptors are created during irradiation the positive space charge of a n-type sensor with for example a phosphorus-doping concentration of typically a few 10^{12} cm^{-3} will be reduced by the so-called *donor removal* [Mol99]. Additionally, N_{eff} is reduced by the created acceptors which are negatively charged in the SC region. With higher fluences these effects become strong enough to compensate the initial phosphorus doping and the effective doping concentration becomes negative. This is called the Space Charge Sign Inversion (SCSI) or *type inversion*. Because the n-type silicon effectively becomes p-type, the pn-junction is no longer on the p$^+$ read-out side, but on the back (n$^+$ electrode) of the sensor. In case the depletion voltage rises above the voltage that can be applied, in addition to the loss of charge from trapping, losses from the non-depleted bulk and a decrease of the position resolution of strip sensors might occur.

In the silicon bulk material there is usually a generation of both, deep acceptors and donors as a result of irradiation with hadrons (neutrons, protons and other charged hadrons). Because of the high dark current generated by current generation centers, these deep donors and acceptors become charged by capturing thermally generated free charge carriers at room-temperature [Ere02]. Because the free charge carrier distribution is non-uniform throughout the sensor volume, the hole concentration $p(x)$ is highest near the p$^+$ electrode and the electron concentration $n(x)$ dominant near the n$^+$ electrode (see figure 5.2a). The occupation of deep donors with holes increases in the direction of the p$^+$ side and contributes to the SC with positive sign while the concentration of occupied deep acceptors with electrons increases in the direction to the n$^+$ side, contributing with negative sign to N_{eff}. Therefore, N_{eff} changes with the depth (compare figure 5.2b), forms an additional pn-junction on the back of the sensor and an applied reverse bias leads to a growth of two depletion regions from both sides of the sensor. The resulting two maxima in the electric field distribution (see figure 5.2c) as a function of the depth is often referred to as *double junction* or *double peak electric field effect* ([Li10]). The influences on the current signals of the sensors will be further discussed in chapter 6.2.

A study on the dependence of N_{eff} on the material for 23 GeV proton irradiated Si sensors was performed within the RD50 collaboration. The materials under investigation are thin Float Zone (50 μm and 100 μm) and Magnetic Czochralski (100 μm) silicon. The sensor processing was performed by CiS. The results of the study are shown in figure 5.3. On

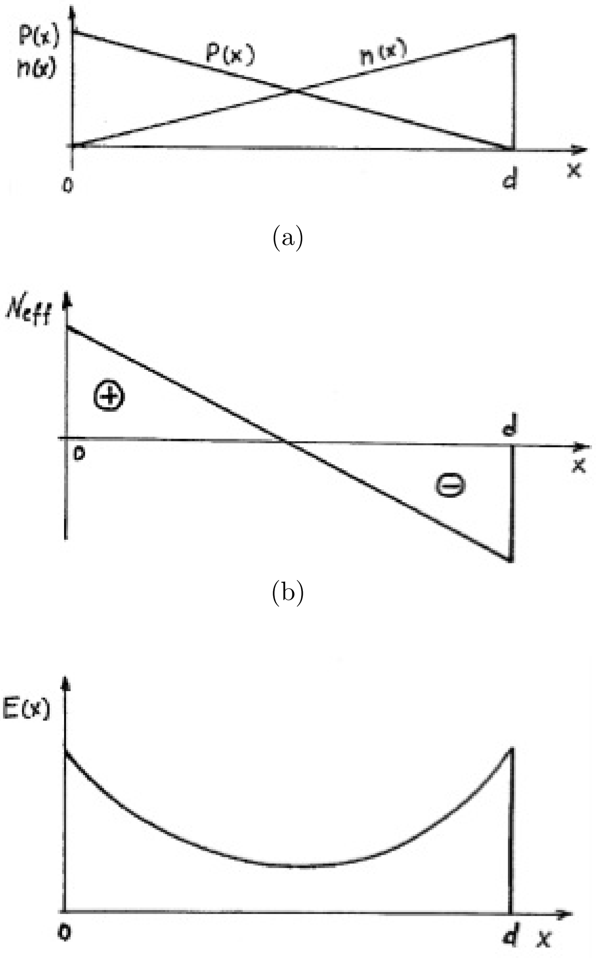

(a)

(b)

(c)

Figure 5.2: Schematic drawing of the model of the origin of the double junction or double peak effect. The x -axis denotes the depth of a n-type diode, with the p^+ electrode located at $x = 0$ and the n^+ electrode at $x = d$. The free electron $n(x)$ and hole $p(x)$ concentrations are shown in (a), the contribution of the deep donors and acceptors to N_{eff} in (b) and (c) shows the resulting electric field E, taken from [Ere02].

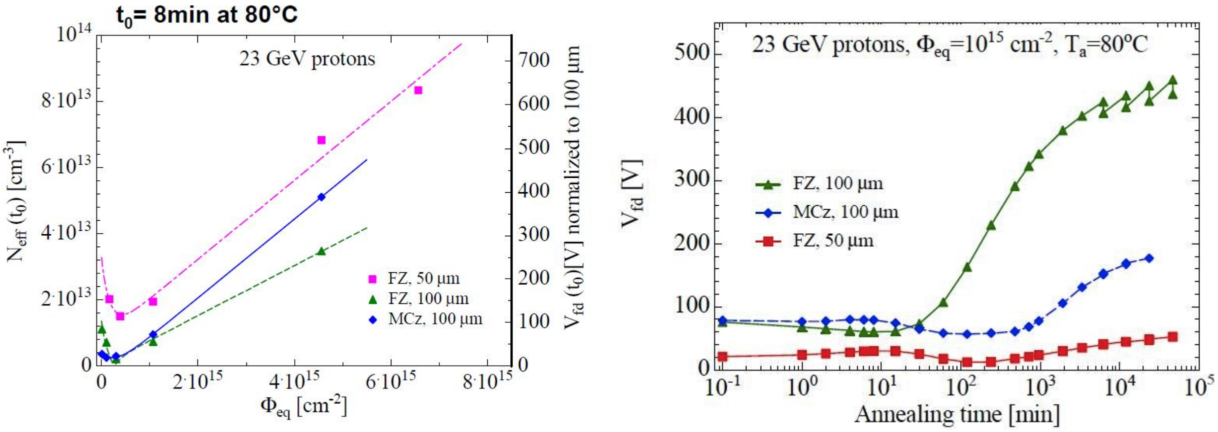

(a) (b)

Figure 5.3: Effective doping concentration and the depletion voltage of RD50 diodes normalized to the volume as a function of the 23 GeV proton fluence (a). Annealing behavior of these materials after a fluence of $\Phi_{eq} = 1 \times 10^{15}$ cm^{-2}, taken from [Eck08].

the left-hand side N$_{eff}$ and U$_{dpl}$ (denoted here as V_{fd}) are presented as a function of the 1 MeV neutron equivalent 23 GeV proton fluence. For 100 μm thick FZ a drop in N$_{eff}$ and U$_{dpl}$ close to zero denotes a SCSI. MCz does not show the strong decrease within the lower fluence range and the thinner FZ does not achieve such low values of N$_{eff}$ and U$_{dpl}$. This progress of |N$_{eff}$| is described in [Mol99] by

$$|N_{eff}(\Phi_{eq})| = N_{eff,0} \cdot \exp\left(-c \cdot \Phi_{eq}\right) \pm \beta\Phi_{eq} \tag{5.1}$$

where the *donor removal* is expressed in the first term by the so-called donor removal constant c. This leads to the decrease in N$_{eff}$ in the lower fluence range until the minimum is reached. After that the introduction rate of stable acceptors β expresses the increase. If the sensor undergoes type inversion, β has a negative sign, else the second term stays positive.

Whether a sensor changes the polarity of its SC during irradiation can be verified by the annealing behavior.

Annealing Behavior of N$_{eff}$

During *short-term annealing* or *beneficial annealing* the positive SC increases. It is not completely understood whether an increase of donors or a decrease of acceptors is responsible for this increase (compare [Mol99]). The effect on N$_{eff}$ can be seen in figure 5.4. For a "non-inverted" sensor (n-type) N$_{eff}$ and therefore U$_{dpl}$ increase before the creation of acceptors because the *long-term annealing* or *reverse annealing* (identified in [Pin08])

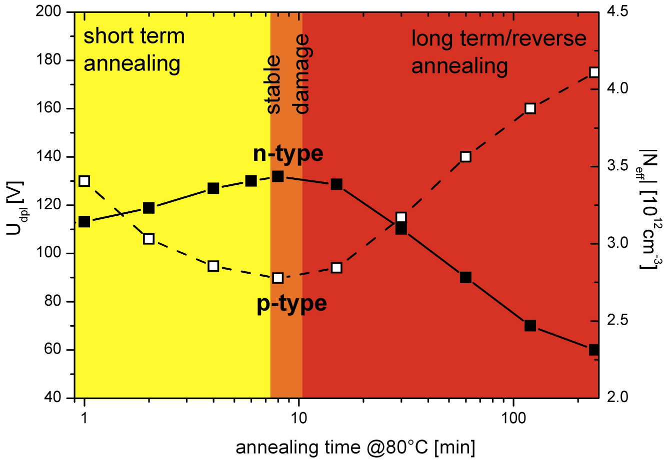

Figure 5.4: U_{dpl} and N_{eff} as a function of the annealing time at 80 °C. The full squares describe the behavior of an n-type sensor, while the open squares denote p-type annealing behavior. The yellow, orange and red color code in the background suggests the three annealing categories (short-term annealing, stable damage and long-term annealing), respectively.

becomes dominant and increases the negative SC. For an "inverted" sensor (p-type) the impact is contrary. Within the *short-term annealing* its negative SC is reduced and N_{eff} decreases until the acceptor generation dominates the annealing behavior. Therefore, the behavior of N_{eff} with annealing is used as an indicator to identify "type-inverted" sensors. The change of the effective doping concentration introduced by irradiation is often described by $\Delta N_{eff} = N_{eff,0} - N_{eff}$.

When the short term annealing is completed, the so-called *stable damage* is reached, before the *long-term annealing* starts. This is the most important value because it is the main part of the damage introduced by irradiation.

In figure 5.3b the annealing behavior of the RD50 materials is shown for a fluence of $\Phi_{eq} = 1 \times 10^{15}$ cm^{-2} 23 GeV proton irradiation. While the thin FZ and the MCz show an increase in U_{dpl} in the first minutes of annealing, the annealing curve of the FZ (100 μm) decreases. The conclusion is that during irradiation a high number of acceptors is created, compensating the initial doping concentration, while the other materials still have a mainly positive space charge. The difference between the FZ (50 μm) and FZ (100 μm) is only partially explainable by the twice as high oxygen concentration of the thinner FZ. It might be an effect due to the thickness of the sensor, but this is not understood yet (see [Eck08]).

5.2 Increase of Dark Current - *Deep Levels*

The probability to generate electron-hole pairs is highest for defect levels near the middle of the band gap, called deep defects. A few cluster-related defects can be identified as current generators, like the $V_3^{-/0}$ defect which lies near the middle of the band gap (activation energy $\Delta E_a = 0.46$ eV).

To understand the additional currents generated by these radiation induced defects, one first has to describe the current in general. The reverse current density is a function of the generation and diffusion current density. The diffusion current density describes the current flow through an ideal diode (by the Shockley equation [Sze01]) and the generation current density describes the generation of e/h-pairs and their flow due to deep mid-gap bulk defects generated in the diode,

$$J_{rev} = J_{diff} + J_{gen}. \tag{5.2}$$

Due to the fact that only the defects in the depleted region contribute to the generation of dark current $I_{gen} \propto W \propto \sqrt{U}$, the dark current increases with increasing bias voltage for $U \leq U_{dpl}$ and saturates when U_{dpl} is reached. Thus, the dark current can be approximated by

$$I_{dpl} \approx I_{gen} = \frac{q_0 n_i W(U) A}{\tau_g}, \tag{5.3}$$

with the intrinsic charge carrier concentration n_i and the generation life time τ_g, the probability of thermally stimulated emission of e/h-pairs. A temperature scaling of the dark current with respect to 20 °C is given by [Chi95]

$$I_{T_{20^\circ C}} = I_T \cdot \left(\frac{T_{20^\circ C}}{T}\right)^2 \exp\left(-\frac{1.21eV}{2k_B}\left[\frac{1}{T_{20^\circ C}} - \frac{1}{T}\right]\right) \tag{5.4}$$

In this work IV measurements have been preferably performed at 20 °C. As a rule of thumb, a change of 1 °C increases or decreases the current by 8 %.

The forward current is the current measured while applying a forward bias. It provides information about the series resistance R_S of the diode. It can be described by the sum of the diffusion current and the recombination current. The recombination of charge carriers is caused by defects in the band gap. The resistivity is related to the forward current by

$$I_{fw}(U) \propto exp\left(\frac{q_0 U - I_{fw} \cdot R_S}{\eta k_B T}\right) \tag{5.5}$$

where η is the so-called *ideality factor* which is 1 if the ideal diffusion current dominates and 2 if the generation current is dominat. When both are comparable $1 < \eta < 2$. Detailed information can be found in [Sze01] or [Mol99].

A typical IV characteristic is shown in figure 5.5 for a non-irradiated sensor. The forward current increases from a certain voltage up to several mA. For high currents and high-resistivity materials the voltage drop $I_{fw} \times R_S$ has to be taken into account. In reverse direction the dark current increases in the range of pA until the whole volume is depleted and then saturates. Above a certain reverse voltage, the diode becomes conductive. This voltage is called breakdown voltage.

The resistivity of an irradiated diode changes with the fluence, typically it increases. Therefore, the current as function of the voltage under forward bias is lower than in the case of non-irradiated sensors.

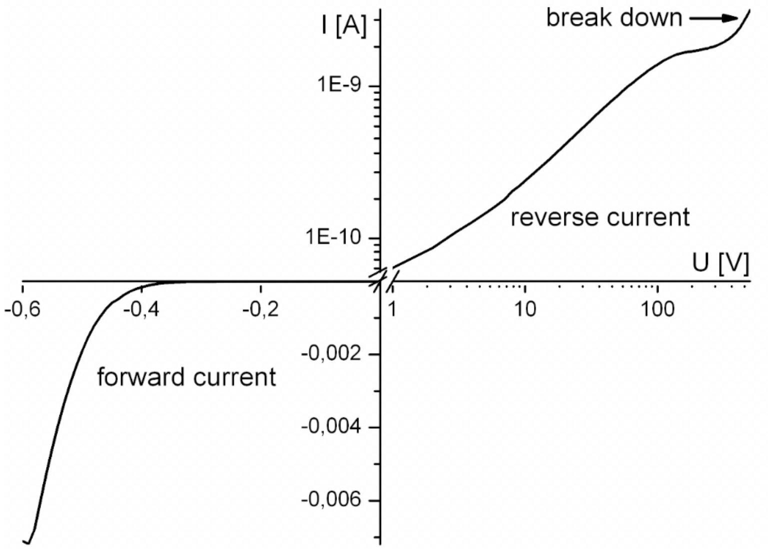

Figure 5.5: IV characteristic of a non-irradiated diode, measured at 20 °C.

5.3 Increase of Trapping - *Deep Levels*

A second effect of deep levels is an increase of *trapping*. While charges captured by defects at the edges of the band gap recombine quickly, deep levels have a high capture cross section and a large emission/detrapping time constant with respect to the charge collection time. Thus, the trapping causes a decrease in the charge collection efficiency (see also chapter 6.2). That is the reason for the radiation induced decrease in signal height.

Chapter 6

Parameters under Investigation

The work focusses on the investigation of radiation-induced defects in the crystal bulk of silicon diodes and their influence on the electrical properties. This chapter addresses the methods used in order to extract the electrical (macroscopic) parameters of the sensor such as the depletion voltage, U_{dpl}, the dark current at full depletion, I_{dpl}, and the Charge Collection Efficiency (CCE) as well as the characterization of defects in the bulk (microscopic parameters) by means of Deep Level Transient Spectroscopy (DLTS) and Thermally Stimulated Current (TSC).

6.1 Electrical Characterization of Silicon Sensors

As explained in chapter 5.2 a very important change of the sensor parameters due to irradiation is the generation of acceptors or donors in the silicon bulk. The voltage at full depletion (U_{dpl}) gives a measure of the effective doping concentration (compare equation 3.4). The second influence of defects in the bulk is the increase of dark current. Both parameters can be obtained by means of *Capacitance-Voltage (CV)* and *Current-Voltage (IV) characteristics*. Here, the use of the GR is essential to define the depleted volume by the geometrical pad area. Thus, effects on the dark current and the capacitance can be neglected. In order to ensure a constant temperature during the measurements, the Cold Chuck PT100 (ATT-Systems[6]) with a temperature stability of 0.5 °C was used.

6.1.1 IV Measurement Method

A DC voltage is applied via the cold chuck to the back plane of the sensor and the p^+ contacts of pad and GR are connected to two amperemeter. The dark current of the pad is

---

[6] ATT Advanced Temperature Test Systems GmbH, Munich (Germany)

recorded by an electrometer (Keithley 6517[7]) and the GR currents by a pico-amperemeter (Keithley 6485). The dark current is recorded during a voltage ramp. The polarity of the applied voltage leads to either an increase of the SCR (reverse bias) or to an increase of the forward current flow (compare [Sze01]). As the detectors will be designed for high voltages, a measurement of the IV characteristic allows to determine the break down voltage and the contribution of shot noise to the total noise of the detector read-out electronics.

The change of the generation current due to irradiation is described by $\Delta I = I_{dpl} - I_0$, with the initial dark current I_0 and after irradiation at full depletion I_{dpl}. In previous studies by M. Moll the linear dependence of the dark current with the particle fluence was investigated (see figure 6.1). This relation between the volume generation current and the neutron fluences is independent on the material type. The increase of the dark current with fluence can be described by

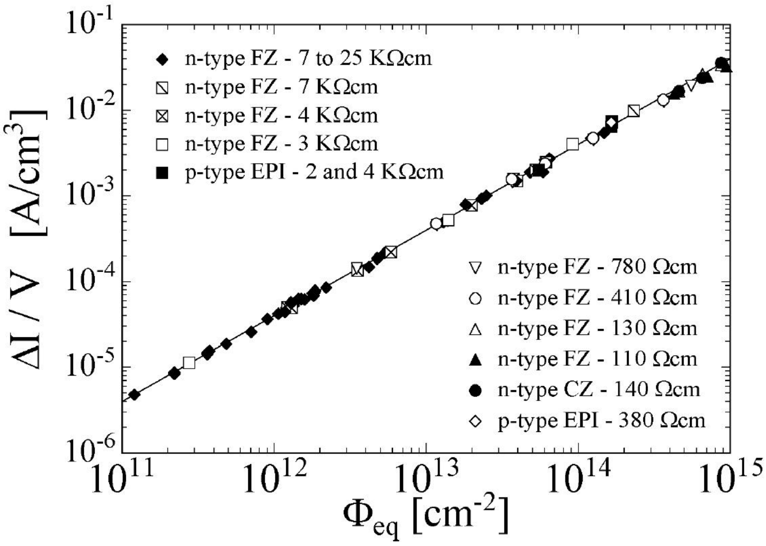

Figure 6.1: The current points were taken from different material types after neutron irradiation for each sensor at the stable damage point of an annealing of 80 minutes at 60 °C. All currents have been normalized to 20°C, taken from [Mol99]

$$\Delta I = \alpha \Phi_{eq} V \tag{6.1}$$

where α is the current related damage rate and V the depleted volume of the sensor. The calculated slope of the linear equation leads to a damage rate of
α(80min@60°C)= $(3.99 \pm 0.03) \cdot 10^{-17}$ A/cm.

---

[7] TEKTRONIX GMBH Keithley Instruments, Germering (Germany)

6.1.2 CV Measurement Method

The inductance (**L**) capacitance (**C**) and resistance (**R**) meter is calibrated for additional capacitances of cables and an isolation box with the GR connected and the pad connection needle lifted. In the following, the pad is connected. Both the impedance Z or admittance $Y = Z^{-1}$ of the diode can be measured by the LRC meter. The equivalent circuit of a reverse-biased diode is presented in figure 6.2 and described by a capacitor (C), a parallel resistor (R_P) that represents the dark current and a series resistor (R_S) representing the bulk resistance of the diode. However, this equivalent circuit does not reflect the frequency-dependent contribution to the signal arising from defects in the bulk. Highly irradiated sensors with a high concentration of defects are strongly dependent on the frequency of the AC-signal because of the frequency dependence of the charging and discharging of the different defect levels.

In case of a non-irradiated diode the series resistor R_S can be neglected. For this reason the admittance is given by $Y = \frac{1}{R_P} + i\omega C_P$ (parallel mode), with the measured detector capacitance C_P, i the imaginary unit and $\omega/2\pi$ the measurement frequency of the AC signal. Within the serial mode the leakage current ($R_p \to \infty$) is neglected and the impedance is given by $Z = R_S - i\frac{1}{\omega C_S}$ (series mode), with the measured detector capacitance C_S.

In this work, the parallel mode has been chosen if not stated otherwise, because it represents the irradiated diodes very well. Moreover, due to the large number of deep defects in irradiated sensors, the capacitance measurements become frequency and temperature dependent. Therefore, one agreed for comparability on standard measurement parameters: at 20 °C with frequencies of 10 kHz and 1 kHz, at 0 °C with 1 kHz and -20 °C with 455 Hz and 1 kHz. Previous investigations showed that the extracted depletion voltage at 20 °C is comparable with the one obtained from charge collection measurements [Lan09].

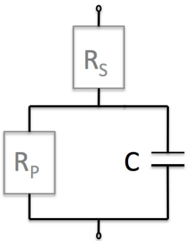

Figure 6.2: Equivalent circuit representing a real diode, biased in reverse direction. Description see text.

The determination of U_{dpl} was done using the program *detwndVI*, by fitting two straight lines to the decreasing part of the CV curve and the saturation part (geometrical capacitance C_{end}) of the CV curve represented in log-log scale as presented in Fig. 6.3. The intersect is defined as the depletion voltage U$_{dpl}$. I$_{dpl}$ is given by the current value at the corresponding voltage in the IV curve.

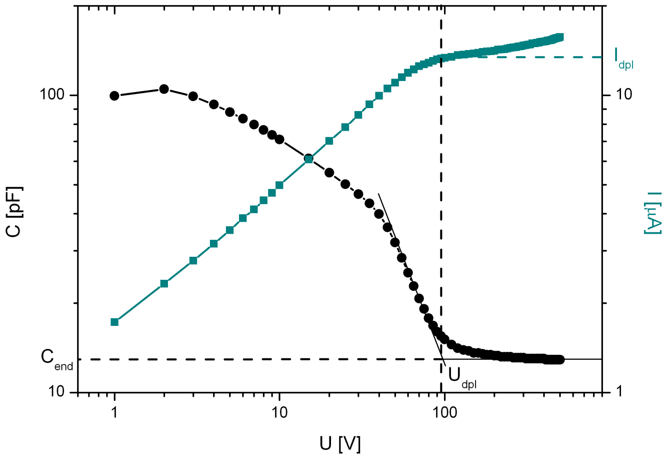

Figure 6.3: Capacitance and dark current as a function of the applied reverse voltage for a diode irradiated with 23 GeV protons to $\Phi_{eq} = 3 \times 10^{14}$ cm^{-2}, measured directly after irradiation at 0 °C with 1 kHz.

6.2 Determination of the Electric Field Distribution and Charge Collection Efficiency

In order to understand the impact of different particle energies on the radiation induced damage in silicon sensors, it is imperative to understand the electrical field distribution inside the sensors and the Charge Collection Efficiency (CCE). A powerful tool to investigate the signal formation as a function of time and correlated parameters, like the electric field (E), charge carrier lifetime (τ) and the CCE, is the transient current technique (TCT).

6.2.1 Transient Current Technique (TCT)

TCT is based on the measurement of the induced current transient of drifting charge carriers in the silicon bulk under the influence of an electric field E. Technically, e/h-pairs are created by illumination of a reversely biased sensor with 70 ps laser light pulses. Influenced by the electric field the charge carriers drift towards their respective electrode and induce a current signal that can be measured as a function of time (current transient). According to Ramo's Theorem [Ram38], the induced current signal can be expressed by

$$I_{e,h}(t) = \frac{q_0 N_{e,h}(t)}{d} v_{drift_{e,h}}(t) \tag{6.2}$$

for a fully depleted sensor. Here $N_{e,h}$ is the number of charge carriers and $v_{drift_{e,h}}$ the drift velocity. The drift velocity is dependent on E and the mobility of the charge carriers $\mu_{e,h}$

$$v_{drift_{e,h}} = \mu_{e,h}(E)E. \tag{6.3}$$

Depending on the creation region of the charge carriers, different parameters may be obtained by means of TCT. If created directly underneath the contacts of the sensor one type of charge carriers immediately reaches the near electrode, while the other type of charge carrier has to pass the whole bulk volume. For example a red laser with a wavelength of 670 nm and an absorption length of 3.3 μm in silicon at room temperature would lead to such a generation of charge carriers underneath the surface. Depending on front or back illumination, it is possible to extract τ and CCE separately for electron and hole signals. However, the illumination with an infrared laser (λ = 1063 nm) and an absorption length of about 1000 μm would create charge carriers homogeneously in the whole sensor depth. Therefore, the signals of both charge carriers contribute to the current transient.

According to Eq. 6.2 and 6.3, the induced current is proportional to the drift velocity of the charge carriers and $v_{drift_{e,h}}$ is higher in high electric fields. Therefore, at high E the current signal is high. For a non-irradiated n-type MCz diode as presented in figure 6.4a the high field is located at the pn-junction on the front (compare Poisson equation 3.1). TCT pulses for a non-irradiated diode (MCZ200N) illuminated from the front and back side with a red laser and with the infrared laser from the front are shown in figure 6.4a. The purple curve illustrates the combined electron/hole signal (illumination by infrared laser), the solid black curve the electron signal (illumination of the front with red laser) and the dashed grey curve the hole signal (illumination from behind with red laser).

However, the irradiation with hadrons creates defects in the silicon bulk. They affect the current generation, N_{eff} and the charge carrier trapping and therefore also the electrical field shape of the sensor. In some cases, the field distribution develops a double peak shape (see [Lin01][Ere02]). This double peak is a sign for the position dependence of the occupation of deep donors and acceptors in the SCR, as described in chapter 5.1. In such a case the polarity of the space charge changes inside the depletion region. If the negatively charged region dominates, the former n-type bulk becomes type-inverted

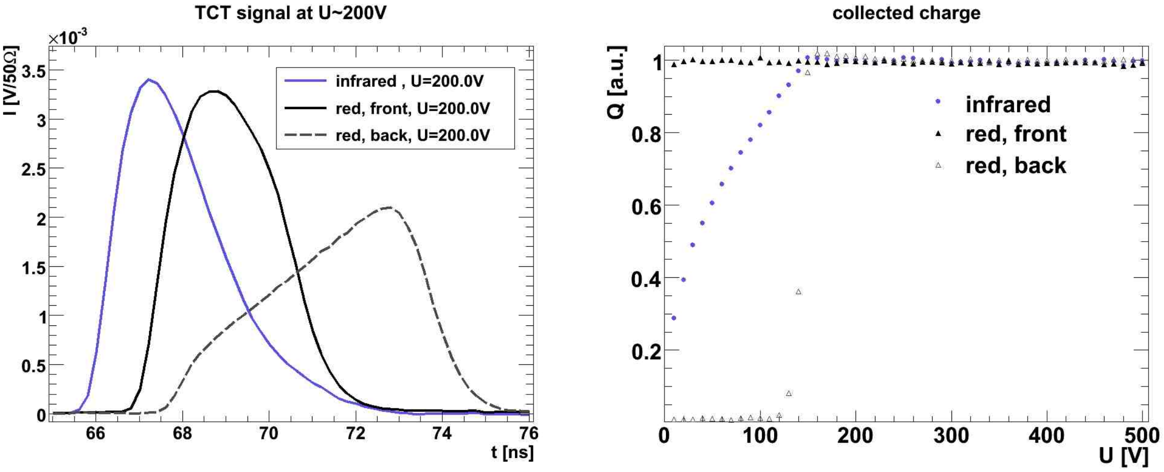

(a) (b)

Figure 6.4: TCT pulses of a non irradiated n-type MCz diode (MCZ200N) for different types of illumination are shown in (a). Description see text. The CCE is presented in (b) for respective TCT pulses.

(p-type). Effectively, the pn-junction is then on the back (n^+ electrode) of the sensor and therefore the high field is located on the back. For brevity we will refer to n-type sensors with a high field at the n^+ electrode and a p-type bulk after irradiation as *type inverted.*
For a HEP detector the most interesting value is the collected charge Q, because it has a preset threshold, which depends on the noise of the complete detector module. The collected charge is given by the integrated current transients

$$Q = \int \mathrm{I}_e(t)\,\mathrm{d}t + \int \mathrm{I}_h(t)\,\mathrm{d}t. \tag{6.4}$$

The charge collection efficiency (CCE) is defined as the ratio between the injected and collected charge

$$CCE = \frac{Q}{Q_0} \tag{6.5}$$

with the deposited number of charge carriers $Q_0 = q_0 N_0$. This value is extracted from a non-irradiated diode of the same material type and volume. The CCE of the non-irradiated diode and biased to total depletion is assumed to be 1 and taken as a reference for the irradiated sensors. In figure 6.4b the CCE for a non-irradiated diode is shown. The curves — founded on the measurements of the same material as in (a) — show the CCE for infrared light injection in purple, for red laser illumination on the front in black and for red laser illumination on the back as black open triangles.
The signal for injection on the back with a red laser is very low for voltages up to U_{dpl}.

At voltages higher then U_{dpl} it increases instantaneously. This is because the electric field of a non-irradiated sensor grows from the front, and only when it reaches the back where charges are deposited, they can drift to the respective electrodes and induce a current.
In this work TCT measurements were only used qualitatively. For additional detailed information and information about the *trapping* mechanism and related calculations see [Kra01], [Lan09] or [Poe13].

6.3 Defect Properties

To investigate electrically active defects in silicon, two microscopic methods were used. The Deep Level Transient Spectroscopy (DLTS) and the Thermally Stimulated Current Technique (TSC). Both methods can be used to extract the most important properties of defects: the defect concentration N_t, the activation energy ΔE_a and the capture cross section σ_t. While DLTS records capacitance transients, TSC measures the current due to emission of trapped charge carriers from the defects. Because both are influenced by the electrically active defects, both provide information on the emitted or captured charge carriers and the activation energy of the defects.

6.3.1 Deep Level Transient Spectroscopy (DLTS)

This method is the most powerful and widely used spectroscopy technique to study electrically active defects in semiconductors. However, this method is limited by the trap concentration (concentration of defects) compared to the initial doping concentration $N_t \ll N_{eff,0}$, which is not any longer the case for highly irradiated sensors. The maximum proton fluence for HPK MCZ sensors of $N_{eff,0} \approx 4 \times 10^{12}$ cm^{-3} is $\Phi_{eq} \approx 4 \times 10^{11}$ cm^{-2}. The Deep Level Transient Spectroscopy records capacitance transients as a function of the temperature of the diode. The shape of the transient depends on the emission of charge carriers from the traps into the conduction/valence band.

DLTS Principle

The DLTS principle for detecting an electron and a hole trap is shown for a n-type diode in figure 6.5. For *electron traps*, the first step is to apply a reverse bias to create a depleted region $W \propto \sqrt{U}$ (see formula 3.2). Because of the ionized phosphorus a positive space charge is created. When decreasing the bias voltage (step 2) the depleted region shrinks and electrons flow into the space charge region (majority carriers) and the defects with a level below the Fermi level are filled by electrons. Therefore, the positive space charge is compensated by the negative charge of electrons. By increasing the reverse bias again (step 3) the capacitance decreases and the captured electrons are emitted to the conduction band (if the thermal excitation is high enough). This emission can be measured as a change in the capacitance. Recorded as a function of time this is called a capacitance transient.

Hole traps (energy levels below the Fermi level) can capture majority carriers (electrons) under the applied reverse bias. But they are only occupied by electrons before they catch holes. Within the second step a forward bias is applied, thus the bulk is filled by minority and majority carriers. Then the reverse bias is applied again and the change of the capacitance with the time is recorded (step 3). The hole trap will catch holes, but like already explained in section 4.3.5 also electrons. With a high forward current ($n \approx p$) a capture of holes is given by the ratio of the electron and hole capture coefficients $p_t = (1+\frac{c_n}{c_p})^{-1}$. In case c_p is too small to guarantee the filling of hole traps, other methods like injection with light have been used (more about that in section 6.3.2).

In comparison, the capacitance transient for an electron trap has a negative and for a hole trap a positive polarity due to the capture of electrons (negative SC)/holes (positive SC) which leads to a smaller/larger capacitance then the initial capacitance C_R.

Determination of Defect Parameters

According to the Shockley-Read-Hall statistics the capture and emission of charge carriers of a defect level can be described as a statistical process. As a result, the emission time constant τ_i or the inverse of the emission rate e_i ($i = n$ for electrons or $i = p$ for holes) is given by

$$\tau_i = \left(\sigma_i v_{th,i} N_{C,V} \cdot \exp\left(-\frac{\Delta E_a}{k_B T}\right)\right)^{-1}, \; i = e, h \tag{6.6}$$

with σ_i the capture cross section for electrons (holes), $v_{th,i} = \sqrt{\frac{3k_BT}{m_{eff,i}}}$ the so-called thermal velocity of the electrons (holes) with the effective electron (hole) masses $m_{eff,i}$.

$N_{C,V}$ denotes the effective density of states in the conduction (valence) band and the activation energy $\Delta \mathrm{E}_a$. With the help of an *Arrhenius-plot*

$$\ln\left(\tau_i v_{th,i} N_{C,V}\right) = -\ln\left(\sigma_i\right) + \frac{\Delta E_a}{k_B T} \tag{6.7}$$

the activation energy can be extracted by the slope of $\ln\left(\tau_i v_{th,i} N_{C,V}\right)$ versus 1/T and the capture cross section from the intersection with the ordinate.

The defect concentration N_t is proportional to the amplitude of the capacitance transient

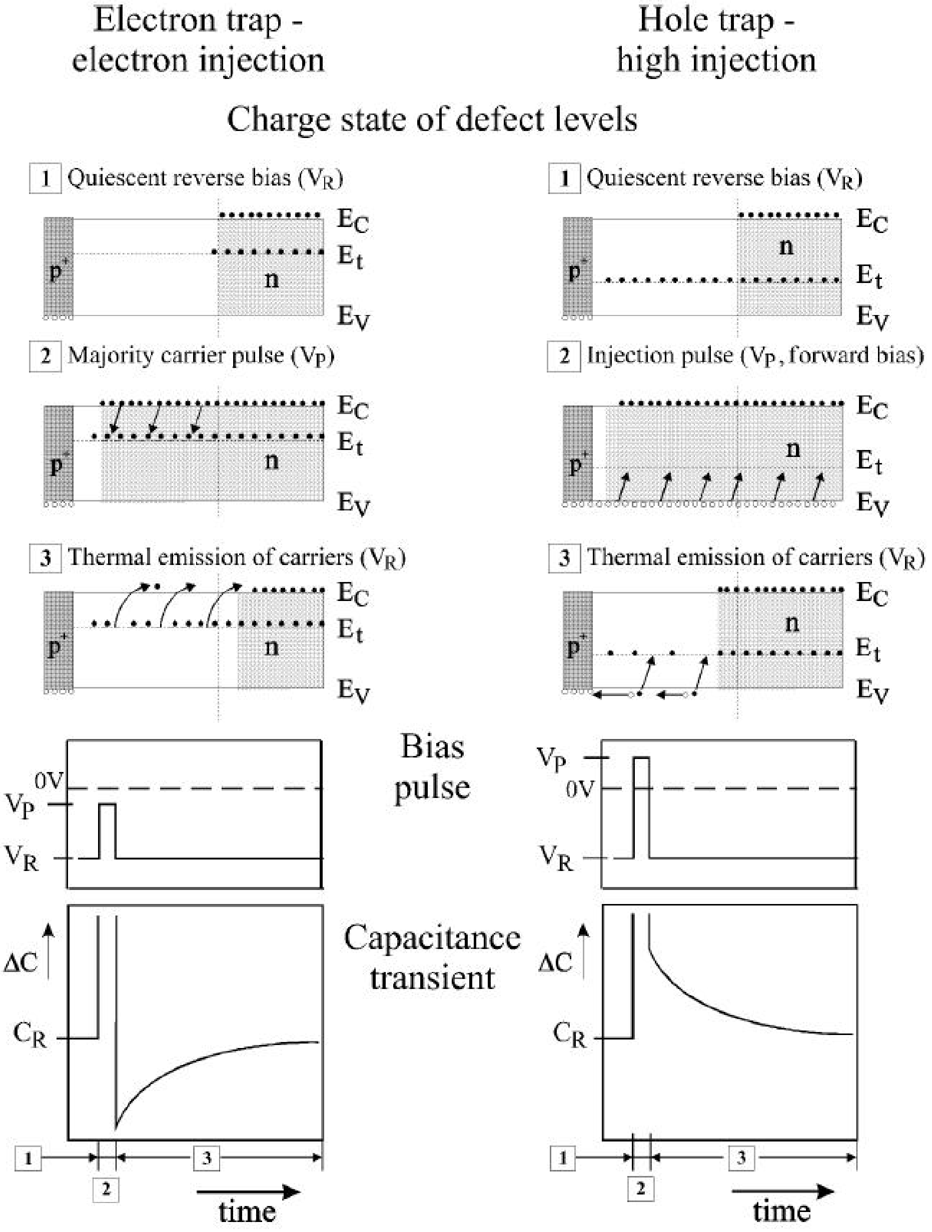

Figure 6.5: The DLTS principle demonstrating the development of the capacitance and bias pulse during the loading and re-loading of an electron trap (left hand side) and a hole trap (right hand side), taken from [Mol99].

$\Delta C_0 = C(t=0) - C_R$ and can be approximated to

$$N_t \approx 2N_{eff,0}\frac{\Delta C_0}{C_R}. \tag{6.8}$$

With the capture cross section, the emission time constant and the amplitudes of the capacitance, all important defect parameters are described.
The measured capacitance transients follows an exponential behavior

$$C(t) = \Delta C_0 \cdot \exp\left(-\frac{t+t_0}{\tau_i}\right) + C_R \tag{6.9}$$

where t_0 denotes the delay to avoid pulse overload recovery of the measurement bridge. The most important measurement modus in this work has to be mentioned, that is the temperature scan *Tempscan*. With the variation of the temperature the band gap is scanned from the mid-gap levels to the band edges. Near the energy level, the emission time constant matches the time window T_W. T_W is the time within the transient is measured and which is chosen for each specific measurement. When energy and emission time and time window match perfectly, the emission is highest.
The capacitance transients are folded within a time window T_W with correlation functions and plotted as a spectrum. The commercially available DLTS program from PhysTech[8], developed by S. Weiss during his PhD-work [Wei91] is used with 30 different folding functions. However, in this work the b1-correlator was the choice to extract the defect concentrations. The b1-correlator is the folding of the transient with a sine function and given by

$$b1 = \frac{2\Delta C_0}{T_W}\int_0^{T_W} \exp\left(-\frac{t+t_0}{\tau_i}\right)\sin\left(\frac{2\pi}{T_W}\cdot t\right)dt. \tag{6.10}$$

In this work three different values for T_W have been chosen; 20 ms, 200 ms and 2 s, which allows to record the emission rates over a large temperature range and a precise evaluation of the activation energy and capture cross section.
The above introduced formulae are taken from [Mol99], where the method of DLTS is well described and an explanation of the analysis method is given in detail.

6.3.2 Thermally Stimulated Current (TSC) Technique

Compared to DLTS, this method can be used for highly irradiated sensors up to $\Phi_{eq} \approx 5 \times 10^{14}$ cm^{-2}.

---

[8] PhysTech GmbH, Moosburg (Germany)

TSC Principle

This technique is based on a current measurement. The first step is to cool down the sample to very low temperatures (our setup was able to achieve 10 K) and then fill the traps with free charge carriers. This can be done with a forward bias to inject electrons and holes or with light injection. In this work green laser diodes with a wavelength of 530 nm with a short absorption length in silicon were used to produce electron-hole pairs directly underneath the electrodes. Thus, within the electric field for illumination from the front (in n-type diodes) only electrons drift through the bulk and get (mostly) captured by electron traps, while the illumination from behind fills hole traps. However, the precise absorption length of the green light is not known at that low temperatures (below 30 K). What is known, however, is that with lower temperature the absorption length increases, which is visible in the recorded spectra by a (low) filling of hole traps also for electron injection. Therefore (and because of a not clearly identified injection volume for the beam spot) this measurements can only be used qualitatively and in order to identify the position of the defect, either in the upper or the lower part of the band gap. With the forward current injection the volume is well defined by the GR and the only difficulty for this method is to inject enough charge carriers to make sure that the charge density for filling all defects is sufficiently high. Only in that case it is possible to compare different spectra. In this work a forward current of 1 mA was aimed at, which is not trivial anymore for high proton fluences. After the injection the sample is heated with a constant heating rate (here 0.183 K/s) under reverse bias. Due to defect levels at specific temperatures, trapped charges are emitted to the conduction or valence band which gives rise to the current signal. Thus, current peaks at a temperature corresponding to the activation energy of the defect level in the band gap appear in the measured spectra. A plot of these steps is shown in figure 6.6

Determination of Defect Parameters

In the following, the determination of defect parameters by means of TSC spectra is briefly described. The equations are taken from [Mol99], where an explanation is given in more detail.

For a single defect level filled by electrons at a temperature T_0 in a fully depleted sensor, the current measured with the constant heating rate $\beta = dT/dt$ can be described by

$$I_{TSC}(t) = \frac{q_0 A d}{2} e_n(t) n_t(t) \tag{6.11}$$

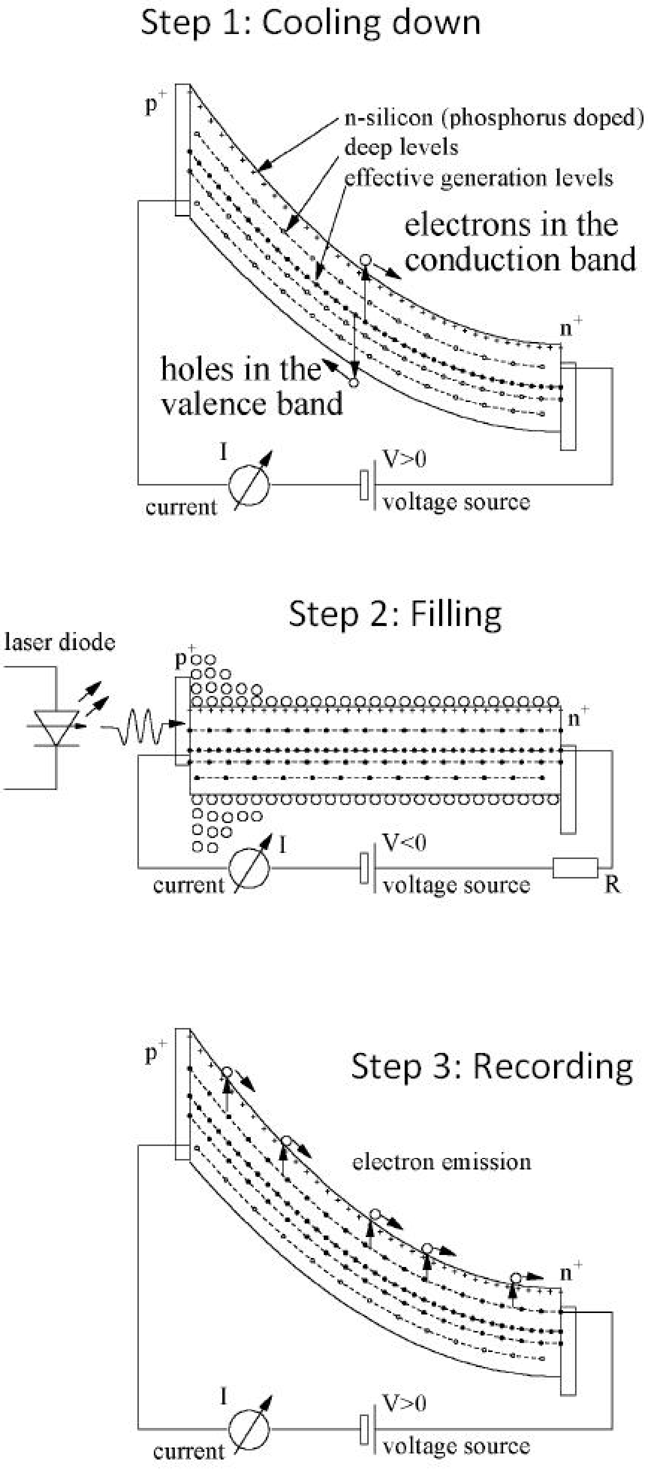

Figure 6.6: The TSC principle for a n-type diode [Mol99].

with $n_t(t) = n_{t,0} \exp\left(-\int\limits_0^t e_n(t')dt'\right)$. The fraction of occupied defects during the filling process is given by n$_{t,0}$ and with the substitution $T = T_0 + \beta t$, the current follows to

$$I_{TSC}(T) = \frac{q_0 A d}{2} e_n(T) n_{t,0} \cdot \exp\left(-\int_{T_0}^{T} dT' \frac{e_n(T')}{\beta(T')}\right). \tag{6.12}$$

The concentration of occupied defects can be calculated by the integration over the TSC current peak

$$n_{t,0} = \frac{2\int dt\, I_{TSC}(t)}{q_0 A d} \tag{6.13}$$

which is the total concentration N$_t$ if the defect was completely filled during the filling process. For defects with field-enhanced emission rates, the TSC spectrum is dependent on the applied reverse bias. With the TSC technique the three dimensional *Pool-Frenkel Effect* (see section 4.4) is observable and the description of the spectrum has to be corrected to

$$I_{TSC}^{PFE}(T) = \frac{q_0 A N_t}{2} \int_0^d dx \left(e_{n,p}^{PFE}(x,T) \cdot \exp\left(\frac{1}{\beta}\int_{T_0}^{T} dT'\, e_{n,p}^{PFE}(x,T')\right)\right), \tag{6.14}$$

see [Pin08] and [Jun11]. As the above introduced formulae indicate, to determine defect parameters by TSC measurements it is essential to make sure that the detector is fully depleted at all temperatures and that the traps are completely filled.

6.4 Error Estimation

A detailed estimation of the errors of the used measurement methods can be found in [Fei97]. The results are shortly summarized here.

- **Fluences**
  The error of the fluences was estimated to be ±10 % (see chapter 4.6). The Proton Synchrotron at CERN quote for the 23 GeV proton irradiation fluence an error of ±7 % (from dosimetry), which did not take other sources of errors like the possibility of dislocated cardboards etc. into account.

- **Annealing**
  Annealing has been performed in an oven which has a temperature uncertainty of about ±1 %. The error of the annealing time is estimated to be ±30 s, which is an overstatement of uncertainties for the first short annealing steps.

- **CV-IV measurements**
  The error of the capacitance and current measurements are approximately 2 %, the equipment error of ±0.1-0.15 % and the uncertainty of the temperature control included. All measurements were done on the *cold chuck*, which has an accuracy of ±0.5 °C.

- **Analysis of CV-IV measurements in double logarithmic presentation**
  This provides the biggest uncertainty for the depletion voltage and the dark current at full depletion. For non-irradiated diodes the CV curves follow a straight homogeneous behavior (±2 %), but after irradiation the curve becomes more complicated (additional frequency and temperature dependence) and the analysis becomes more difficult (±5 %).

- **TCT measurements**
  The major uncertainty is the laser stability, which is estimated to be 1 %. To achieve this small error the laser is warmed up for several hours. The overall error of the CCE is determined to be 3 %, included are effects due to electronic interferences. Further information about the error estimation can be found in [Poe13].

- **DLTS measurements**
  The temperature uncertainty of the temperature controller is ±0.5 K. Additionally, during the tempscan (cooling down and heating up again et cetera) the temperature

range of each capacitance transient measurement might reach ΔT=1.6 K. The reference temperature is usually the starting temperature. The capacitance amplitude and thus the defect concentration has an uncertainty of 5 %.

- **TSC measurements**
  The uncertainty results from the current and temperature measurement plus the evaluation. The equipment is highly precise, but the evaluation of the spectra by fitting the curve plays a major role in estimating the error. This error is estimated to be around ±10 %.

Chapter 7

Macroscopic Results

In the following section macroscopic results are presented for sensors irradiated with two different proton energies.

7.1 Fluence Dependence of the Reverse Current

Two different materials (n-type MCz and FZ) have been irradiated with several fluences. In figure 7.1 $\Delta I = I_{dpl} - I_0$ of all sensors normalized to the detector volume V for an annealing time of 8 minutes at 80 °C is shown as function of the 1 MeV neutron equivalent fluence given by dosimetry of the irradiation facilities Φ^*_{eq}.
The current values of highest fluence of $\Phi^*_{eq} = 3.17 \times 10^{14}$ cm^{-2} for 23 GeV proton irradiated sensors show a large variation of the expected current value (straight red line). This might be due to a problem in the setup of the irradiation. All HPK sensors were stacked together in one support frame and irradiated at the same time. A displacement of the samples inside the cardboards or a shift of the proton beam with respect to the center of the sample stack might have led to such derivation in the accumulated fluence. So far there has not been observed any material dependence of the radiation-induced current generation for MCz or FZ material. However, in chapter 8 there will be a discussion about material defects with less concentration in FZ than in MCz, and maybe here is a hint towards a material dependence as reason for the discrepancy. However, also the RD50 MCz diodes irradiated with 23 MeV protons show higher currents then expected from the fluences resulting from the dosimetry. The measurements for both proton energies are fitted by equation 6.1 with the resulting damage factors $\alpha_{MeV} = 4.21 \pm 0.15 \times 10^{-17}$ Acm^{-1} and $\alpha_{GeV} = 4.32 \pm 0.23 \times 10^{-17}$ Acm^{-1}. The high errors of the α values result from the spread of the measured currents at high fluences, which is due to the dosimetry values of Φ^*_{eq}. If these current values are not taken into account for the fits, the error of

α decreases by half. The deviations of the measured volume generation currents from the expected ones have to be taken into account. Therefore, the fluences Φ^*_{eq} are corrected by $\alpha_{MeV}/\alpha_{GeV}$ instead of the α value from [Mol99], and are denoted in the following chapters as Φ_{eq}.

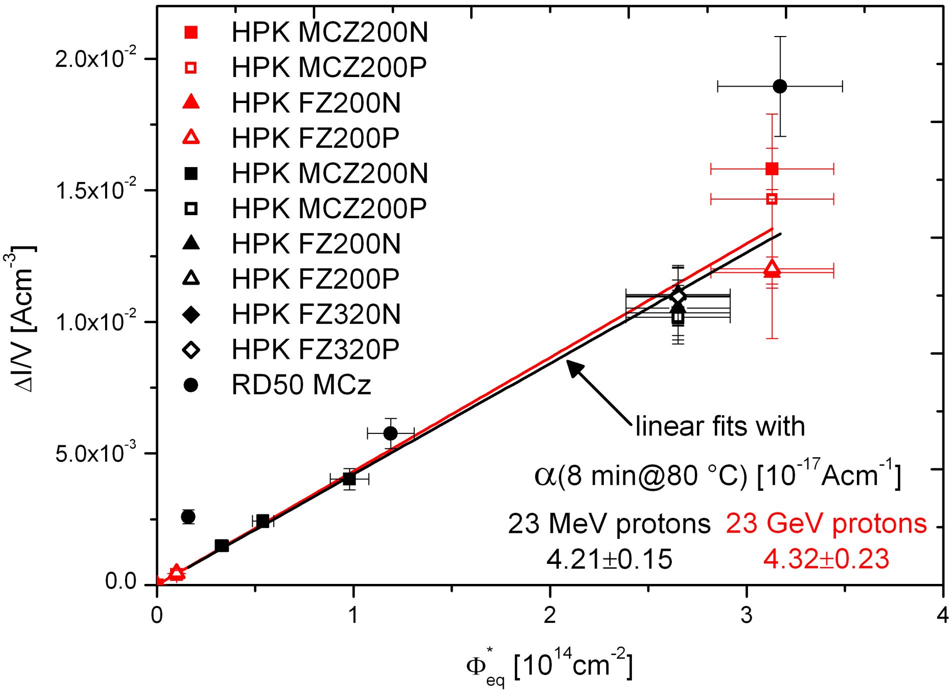

Figure 7.1: The volume generation current measured at 20 °C as a function of the 1 MeV neutron equivalent fluence. Fluences as given by dosimetry. α-values were extracted by two fits to the 23 MeV and 23 GeV data, separately.

7.2 Annealing Behavior and Fluence Dependence of U$_{dpl}$ and N$_{eff}$

Within the CMS tracker upgrade campaign with Hamamatsu Photonics it was observed that all materials under investigation undergo type-inversion after neutron and 23 MeV proton irradiation [Erf12]. It raises the question of why the HPK MCz sensors do not behave like most of the RD50 MCz sensors, building a very in-homogeneous N_{eff} with the depth but remaining n-type after 23 GeV proton irradiation (see figure 5.3).

In the following the detailed study of U$_{dpl}$ and N$_{eff}$ as a function of annealing time and fluence is presented for two different proton energies and two materials with slightly different oxygen content. Starting with MCZ200N material, irradiated with 23 MeV protons, figure 7.2a presents the annealing behavior of N$_{eff}$ for four different fluences up to an annealing time of 30 minutes at 80 °C. Within those 30 min the short term annealing, the point of stable damage and the beginning of the reverse annealing can be observed. Up to a fluence of $\approx 1 \times 10^{14}$ cm^{-2} (black circles with dashed line) all curves show an initial increase in the depletion voltage which is due to an increase of donor or decrease of acceptor concentration. The initial increase is followed by a maximum at 8 minutes and a subsequent decrease of U$_{dpl}$. This is the typical behavior of non-inverted n-type sensors. The curve for the fluence of $\Phi_{eq} = 2.4 \times 10^{14}$ cm^{-2} (black stars with solid line) demonstrates an oppositional behavior. This is a hint to a change of the effective doping concentration from positive to negative SC (p-type). For a p-type sensor holes are majority charge carriers, thus the beneficial annealing (generation of positive SC) would result in the decrease of U$_{dpl}$ in contrast to the increase in n-type material.

Similar changes of the SC could also be observed for the RD50 MCz diodes after irradiation with three different fluences of 23 MeV protons. The curves for the annealing of those sensors are given in figure 7.2b. Here, the p-type behavior is seen after an equivalent fluence of $\Phi_{eq} = 4.5 \times 10^{14}$ cm^{-2} and the change in the sign of the effective doping concentration lies between $\Phi_{eq} = 7.4 \times 10^{13}$ and $\Phi_{eq} = 4.5 \times 10^{14}$ cm^{-2}. The annealing behavior of U$_{dpl}$ for the fluence of $\Phi_{eq} = 1.4 \times 10^{14}$ cm^{-2} is not as significant, it can only be detected a slight increase in the first minutes.

MCZ200N irradiated with 23 GeV protons does not show p-type annealing behavior. For three different 23 GeV proton fluences the annealing behavior of N$_{eff}$ is investigated up to an annealing time of 30 minutes at 80 °C and shown in figure 7.2c. All three curves increases within the first minutes of annealing reach a maximum after approximately 8 minutes at 80 °C and then U$_{dpl}$ starts to decrease. The zig-zagging of the red triangles with solid line of the highest proton fluence of $\Phi_{eq} = 3.8 \times 10^{14}$ cm^{-2} seems to be a result

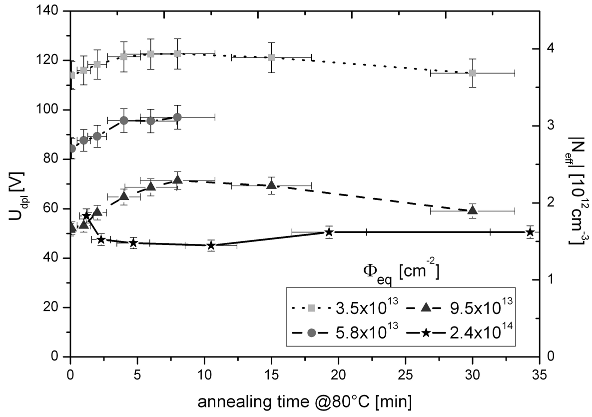

(a) 23 MeV protons

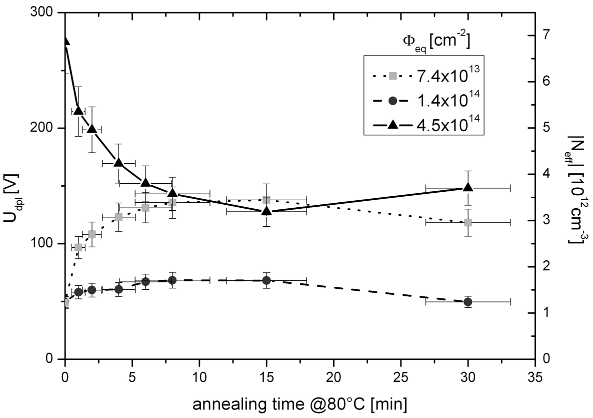

(b) 23 MeV protons

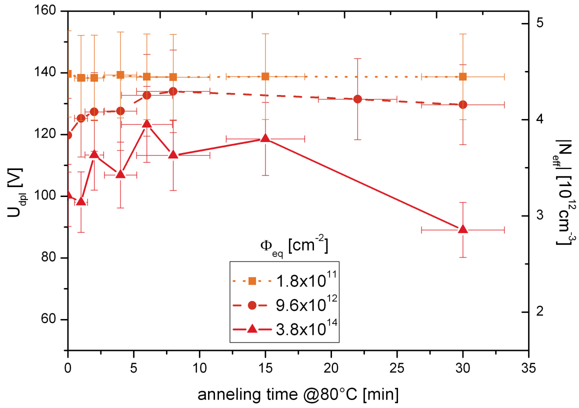

(c) 23 GeV protons

Figure 7.2: Evolution of U_{dpl} and N_{eff} with annealing time for different fluences, proton energies and diodes from different vendors. (a) 23 MeV, MCZ200N (HPK) (b) 23 MeV, MCz 230 μm (RD50) (c) 23 GeV, MCZ200N (HPK).

of numerous measurements at one annealing step, which compressed the annealing curve.

To exclude an influence of the processing by the two vendors on the results, the annealing behavior of MCZ200N diodes from HPK and those from RD50 are compared after 23 MeV and 23 GeV proton irradiation and a fluence of $\Phi_{eq} \approx 3 \times 10^{14}$ cm^{-2} in figure 7.3. The fluences calculated from the dark current are given in the figure 7.3. This comparison confirms that also RD50 MCz diodes undergo type-inversion after 23 MeV proton irradiation while MCZ200N from HPK remains n-type annealing behavior after 23 GeV proton irradiation. Additionally, it is observed that U_{dpl} increases with the fluence. Summing up the information the annealing studies and from TCT measurements (see section 7.3) the sign of N_{eff} is found to become negative for n-type MCz material after 23 MeV proton irradiation. However, N_{eff} remains positive after 23 GeV proton irradiation. In conclusion, it is possible to proof that different proton energies lead to a difference in the effective doping concentration of MCz sensors, independent of the producer.

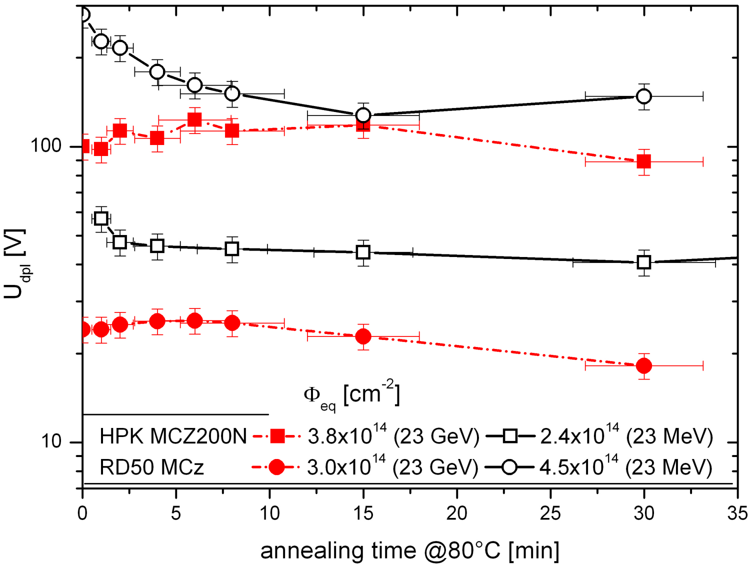

Figure 7.3: Annealing behavior of RD50 MCz material of 230 μm after 23 MeV proton and 100 μm thickness after 23 GeV proton irradiation in comparison to HPK MCZ200N material after 23 MeV and 23 GeV proton irradiation. Precise fluences are given in the figure.

In figure 7.4 the development of $|\mathrm{N}_{eff}|$ with the 23 MeV proton fluence of MCZ200N and RD50 MCz is shown and fitted according to equation 5.1. It has to be mentioned that except the value of MCZ200N irradiated with 1×10^{15} cm^{-2} 23 MeV protons (corresponding to 10 minutes at 60 °C), all values were determined after 8 minutes annealing at 80 °C. Thus the fact that this exceptional value lies above the fit is comprehensible and it is expected that the value would decrease after 8 minutes at 80 °C due to the beneficial annealing. RD50 MCz sensors show a slightly higher fluence needed to reach inversion of N_{eff} ($\Phi_{inv} = 2.0 \times 10^{14}$ cm^{-2}) than the MCZ200N samples ($\Phi_{inv} = 1.8 \times 10^{14}$ cm^{-2}) due to the homogeneous oxygen concentration in the silicon bulk (compare figure 3.3). Some attention has to be drawn to the slope of the fits in figure 7.4. A clear difference is observed between the slope of HPK MCz and RD50 MCz material for the increase of U_{dpl} at higher fluences. This might be an effect of material defects (see chapter 8).

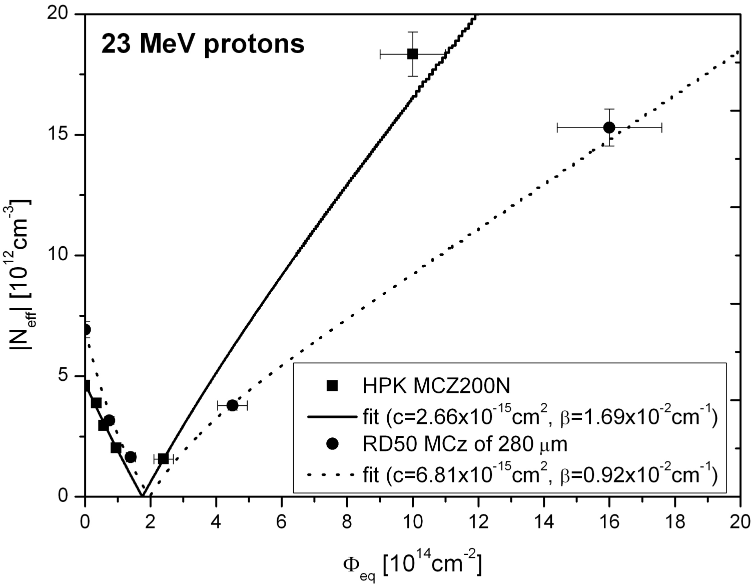

Figure 7.4: $|\mathrm{N}_{eff}|$ as a function of the equivalent fluence for the annealing step of 8 minutes at 80 °C, except the measurement of MCZ200N at $\Phi_{eq} = 1 \times 10^{15}$ cm^{-2}, which was taken after 1 minute at 80 °C and not used for the fit. The measurement parameters: T=20 °C, f=10 kHz. Fits according to equation 5.1.

7.2.1 Oxygen-rich Float Zone

As already mentioned in section 3.3 (page 15) the FZ diodes from Hamamatsu have an extraordinary high oxygen concentration ($[O] = 3 \times 10^{17}$ cm^{-3}). Since the influence of the proton energy on the change of the effective doping concentration is expected to be a result of high oxygen concentration, it is interesting to study this behavior in comparison to MCZ200N sensors as another very oxygen-rich material ($[O] = 5 \times 10^{17}$ cm^{-3}). The annealing curve of a FZ200N sensor irradiated with 23 GeV protons is compared to a MCZ200N diode in figure 7.5a. Based on the fact that the maximum $|N_{eff}|$ was already measured after an annealing step of 2 minutes at 80 °C, which is expected after 8 minutes, the annealing time was corrected by additional 6 minutes. This shift can be due to a heating process during the irradiation at 28 °C at the PS, or a delay caused by handling or the TCT measurements performed in between the CV-IV measurements. The fluence is corrected by the current value at 2 minutes at 80 °C which results in $\Phi_{eq} = 2.9 \times 10^{14}$ cm^{-2}. In comparison with the value given by dosimetry $\Phi_{eq} = 3.1 \times 10^{14}$ cm^{-2}, the correction fits quite well. Especially because the current values decrease with annealing and the fluence extracted at 8 minutes would be much smaller. Considering the first increase within the short term annealing and subsequent decrease after 8 minutes respectively 14 minutes at 80 °C, the FZ200N material seems to remain n-type after GeV proton irradiation, similar to the behavior of MCZ200N material. This will be discussed in more detail in section 7.3. Figure 7.5b presents the comparison of the annealing of U_{dpl} after 23 MeV and 23 GeV proton irradiation. The same distinct annealing behavior for inverted sensors is found for 23 MeV irradiation as seen for the MCZ200N material, i.e. the typical curve for inverted sensors.

Finally, the fluence dependence of $|N_{eff}|$ is presented in figure 7.6a and 7.6b. The fluence necessary to reach inversion after 23 MeV protons is $\Phi_{inv} = 0.68 \times 10^{14}$ cm^{-2} for FZ200N compared to $\Phi_{inv} = 1.75 \times 10^{14}$ cm^{-2} for MCZ200N. This shift is mainly due to the 50 % lower initial doping concentration of FZ200N. However, it cannot be excluded that the higher oxygen content in MCZ200N leads to an additional shift of the type inversion. As seen in the comparison of RD50 MCz and HPK MCz in figure 7.4 for 23 MeV irradiations, the slope of the HPK MCZ200N indicates the highest value for high fluences. It should be noted that it is even steeper than observed for the somewhat less oxygen-rich FZ200N sensors. Additionally, it has to be noted that except for MCZ200N and FZ200N irradiated with 1×10^{15} cm^{-2} 23 MeV protons (corresponding to 10 minutes at 60 °C), all values are determines after an annealing of 8 minutes at 80 °C. Therefore the fact that these values lie above the fit is comprehensible and it is expected that they decrease after 8 minutes at 80 °C due to the beneficial annealing of type inverted sensors.

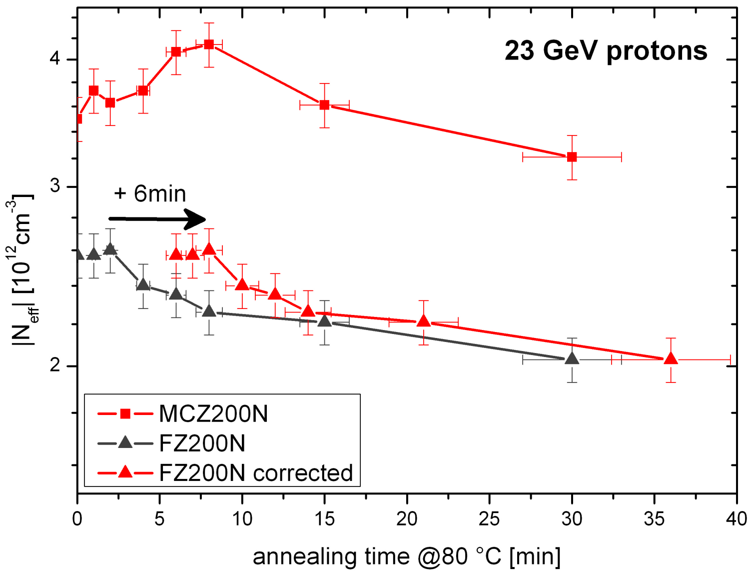

(a) Corrected annealing time of FZ

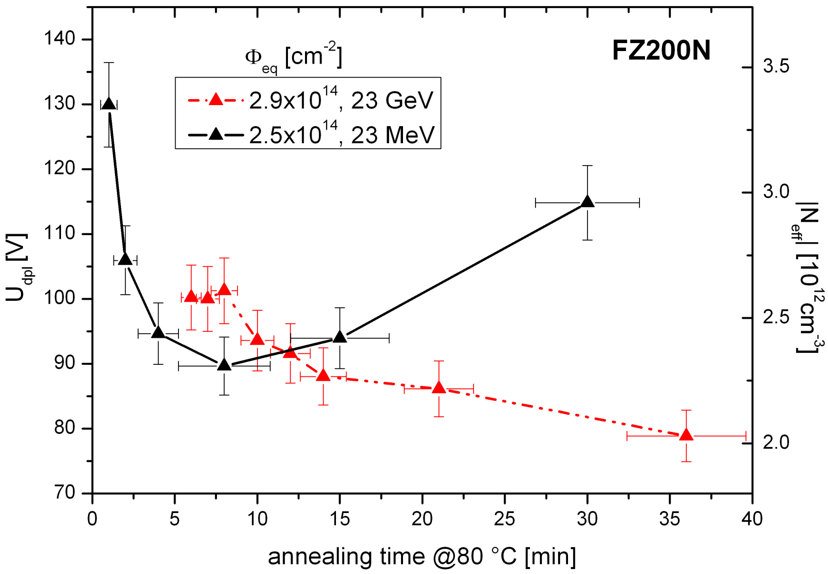

(b) 23 MeV and 23 GeV protons

Figure 7.5: |N$_{eff}$| as a function annealing for MCZ200N and FZ200N after an equivalent fluence of 2.5 and 2.9 × 10^{14} cm^{-2} 23 GeV protons, for FZ200N the curve was corrected for the stable damage point (see [Mol99]) (a), and comparison of U$_{dpl}$ versus annealing time for 23 GeV and 23 MeV proton irradiated FZ200N (b).

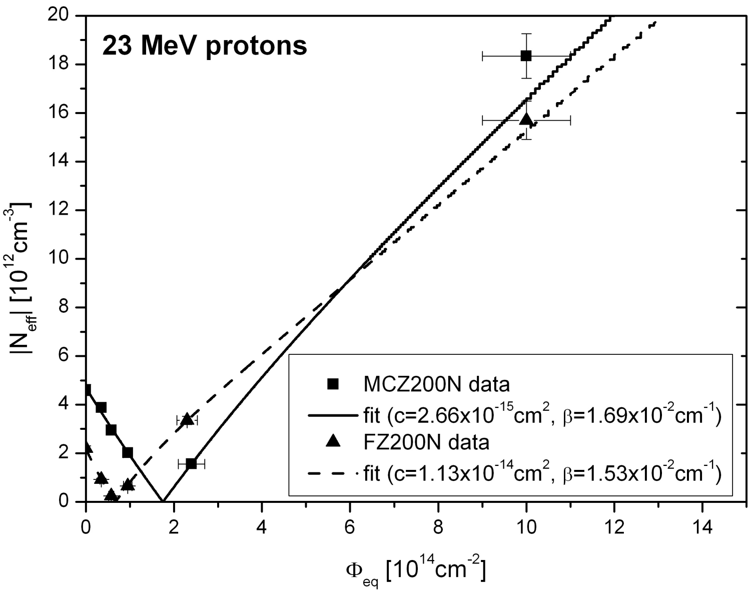

(a) 23 MeV protons

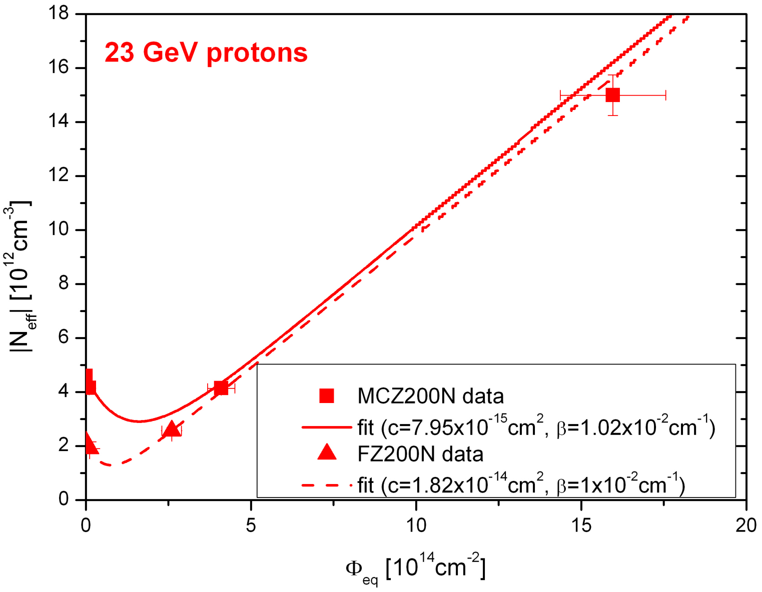

(b) 23 GeV protons

Figure 7.6: $|\mathrm{N}_{eff}|$ for the irradiated MCZ200N and FZ200N sensors as a function of the equivalent fluence for 23 MeV protons (a) and 23 GeV protons (b). The annealing step is 8 minutes at 80 °C, except the measurements of MCZ200N and FZ200N at $\Phi_{eq} = 1 \times 10^{15}$ cm^{-2} 23 MeV protons, which were taken after 1 minute at 80 °C and not used for the fits. Measurement parameters: T=20 °C, f=10 kHz, fits according to equation 5.1.

The results of the U_{dpl} respectively N_{eff} measurements are summarized for all investigated materials and proton irradiations in table 7.1. In conclusion, the donor removal is stronger (larger c) for 23 GeV than for 23 MeV proton irradiation and decreases in general with increasing oxygen concentration (compare FZ and MCz). The introduction rate β is negative (dominant acceptor creation) for 23 MeV protons and positive for 23 GeV protons (dominant donor generation). Therefore a negative β leads to type-inversion and all materials type-invert for 23 MeV proton irradiation. Φ_{inv} depends on the initial doping and the oxygen concentration, which could be the reason why the RD50 MCz sensors require the highest fluence for changing their sign of the SC.

Material	Proton energy	c [cm^2]	β [cm^{-1}]	Φ_{inv} [cm^{-2}]
HPK MCZ200N	23 MeV	2.66×10^{-15}	-1.69×10^{-2}	1.8×10^{14}
HPK MCZ200N	23 GeV	7.95×10^{-15}	$+1.02 \times 10^{-2}$	—
RD50 MCz of 230 μm	23 MeV	6.81×10^{-15}	-0.92×10^{-2}	2.0×10^{14}
HPK FZ200N	23 MeV	1.13×10^{-14}	-1.53×10^{-2}	0.7×10^{14}
HPK FZ200N	23 GeV	1.88×10^{-14}	$+1.00 \times 10^{-2}$	—

Table 7.1: Summary of the results from the N_{eff} fits for al investigated materials. Further explanations can be found in the text.

7.3 TCT Current Pulses and Charge Collection Efficiency

In the following the current pulses and the charge collection efficiency CCE or the collected charge Q are presented for red laser light illumination in different materials after 23 MeV and 23 GeV proton irradiation. The current pulses have not been corrected for trapping as described in [Kra01]. Although the pulse shape might change significantly even by small changes in the trapping times, there is no method available that allows to extract this value with sufficient accuracy [Li10][Kas09][Pac10]. It is therefore preferred to present raw data. The change of the pulse shape due to the trapping correction will be discussed for certain measurements.

Some of the presented TCT pulses are normalized to the total number of injected charge Q_0, to be able to compare the pulse heights even for different measurements at different annealing times. These pulses are given in arbitrary units.

It has to be mentioned, that all TCT measurements presented in this work were performed at 0 °C. Measurements were also performed at -20 °C, but because no difference could be observed between the measurements at 0 °C and -20 °C for the red laser light injection [Poe13], only results from measurements at 0 °C are presented.

Additionally, for every measurement of an irradiated sensor a measurement of a non-irradiated sensor (of the same type) was performed directly one after another to make sure that the laser light output and the electronics are in stable operation. In the following figures these measurements are denoted as "reference".

The goal of these measurements was to develop a better understanding about the electric field distribution in the space charge region of the irradiated sensors and the charge collection dependence on the proton energy and the annealing.

7.3.1 MCZ200N

23 MeV Proton Irradiation

The TCT signals for different bias voltages are shown in figure 7.7. These are taken after illumination from the front of the sensor, which was exposed to a fluence of $\Phi_{eq} = 2.4\times10^{14}$ cm^{-2} 23 MeV protons and annealed to 1 minutes at 80 °C. The pulse shapes show a clear double peak visible up to 100 V (U$_{dpl}$ = 57 V). The double peak can be explained by the electric field maximum at the p$^+$ and n$^+$ electrode. This effect is well known and described in detail in [Ere02] and [Li10]. At high bias voltages (>100 V) the peak at the end of the pulse vanishes and the pulse shape becomes similar to that expected for sensors with a uniform negative space charge. Another observation is that the double peak shape changes significantly with annealing (see Appendix).

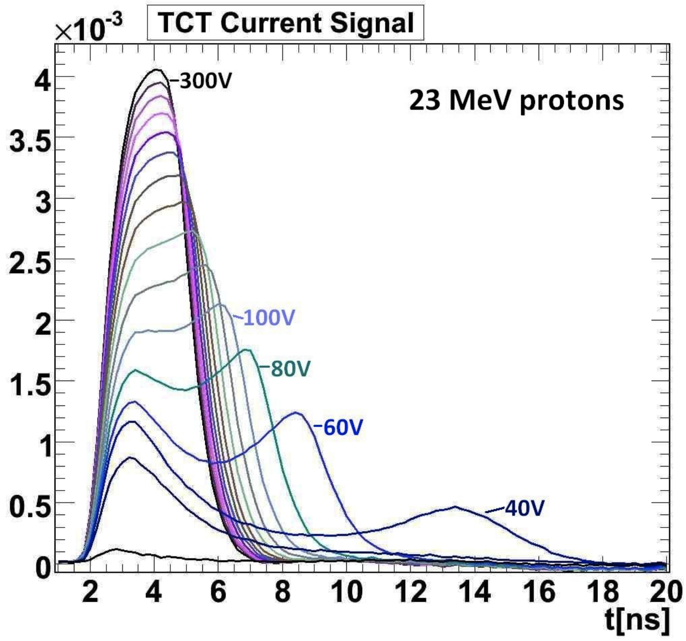

Figure 7.7: TCT pulse evolution with higher voltages for MCZ200N after 23 MeV proton irradiation($\Phi_{eq} = 2.4 \times 10^{14}$ cm^{-2}), measured after an annealing of 1 minute at 80 °C in 20 V steps, measurement performed at 0 °C, illumination with a red laser from the front. The sensor is fully depleted at 60 V.

In figure 7.8 the pulse shapes of MCZ200N after 23 MeV proton irradiation demonstrate the inversion of the sensor to p-type for a fluence of 2.4×10^{14} cm^{-2}. In the electron signals (see 7.8a) the TCT pulses show an increase of amplitude for larger annealing times and the slope of the pulse shapes change slightly in the drift region. The slope of the pulse after an annealing of 1 minute at 80 °C is positive, after 11 minutes the pulse shape becomes negative, and essentially zero after 34 minutes. Here one has to be reminded of the trapping effect. Trapping reduces the signal height in particular at the end of the drift time. A trapping correction would therefore lead to an increase of the current near to the end of the current pulse.

In figure 7.8b, the hole signals are shown as a function of the annealing time. The pulses show a decrease in amplitude between 1 and 11 minutes of annealing at 80 °C and an increase after 34 minutes at 80 °C. The slopes are clearly negative, which is contrary to what happens for non-irradiated sensors. With increasing annealing times it is observed

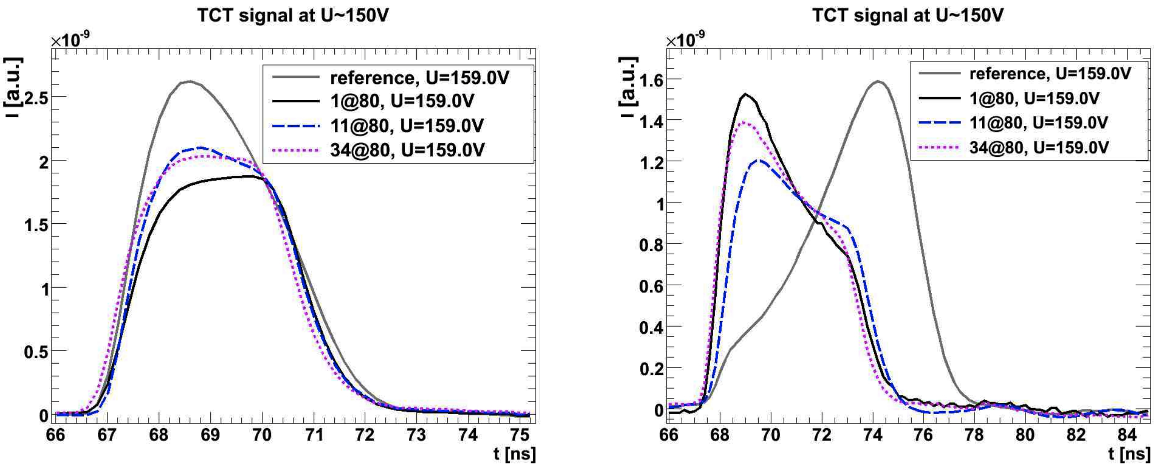

(a) Electron signal

(b) Hole signal

Figure 7.8: TCT pulses of MCZ200N diode after 23 MeV proton irradiation ($\Phi_{eq} = 2.4 \times 10^{14}$ cm^{-2}) annealed to 1,11 and 34 minutes at 80 °C, TCT pulses taken for red laser illumination, from the front (electrons) and back (holes) of the sensor, measured at 0 °C.

that the slope becomes less negative.

The trapping corrected pulses would show an approximately 20 % higher current signal at the end of the drift time [Lan09]. Thus the electron pulse shapes would be positive and the hole pulse shapes stay negative. The electric field height would be strengthened at the back of the sensor. We conclude that the sensor is type inverted.

The CCE for this sensor is shown in figure 7.9 as a function of the bias voltage for illumination from the front and from behind the sensor. The electron collection efficiency (see 7.9a) shows a fast increase with increasing bias voltage and its maximum is increasing with longer annealing time. This sensor has a CCE for electrons at 500 V of ≈ 95 % after an annealing of 34 minutes at 80 °C.

The hole collection efficiency (see 7.9b) shows a slower increase with bias voltage. The maximum in efficiency varies with the annealing time. After 1 min at 80 °C a CCE of ≈ 100 % is achieved at 500 V.

In conclusion, the CCE shows also the effect of inversion i.e. higher field at the p$^+$ side.

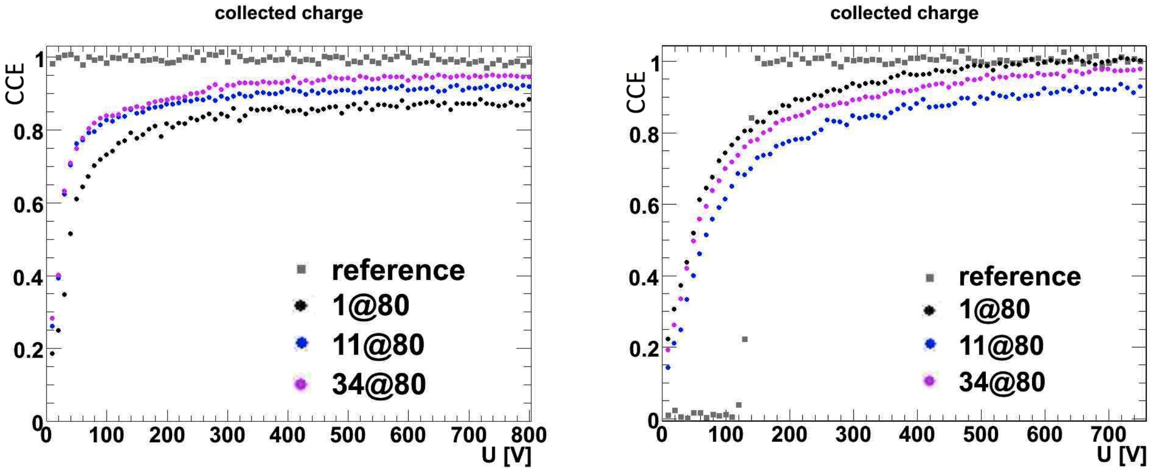

(a) Electron charge collection (b) Hole charge collection

Figure 7.9: CCE taken for red laser illumination, from the front (electrons) and the back (holes) of a MCZ200N sensor after 23 MeV proton irradiation ($\Phi_{eq} = 2.4 \times 10^{14}$ cm^{-2}) annealed to 1,11 and 34 minutes at 80 °C, measured at 0 °C.

23 GeV Proton Irradiation

The same measurements were performed after a comparable 1 MeV neutron equivalent fluence of 23 GeV proton irradiation. The TCT signals from front illumination for different bias voltages of MCZ200N irradiated with $\Phi_{eq} = 3.8 \times 10^{14}$ cm^{-2} 23 GeV protons is shown in figure 7.10 for an annealing of 1 minute at 80 °C. The pulse shapes show a double peak up to 80 V (U$_{dpl}$ = 98 V), which vanishes with higher voltages. The electric field peaks at the p$^+$ and n$^+$ side, but the electric field on the p$^+$ side is larger. Thus the slope gets negative at high voltages like for a sensor with uniform positive space charge.

In figure 7.11 the pulse shapes of the electron and hole signals are shown as a function of the annealing time. The electron signal amplitude of the pulses (a) increases with larger annealing time whereas the pulse slope increases slightly at short drift times with annealing. The reason is a higher electric field on the p$^+$ electrode.

The amplitude of the hole signals (b) shows a decrease to 8 minutes at 80 °C and with annealing times above 8 minutes at 80 °C an increase is seen. The shape of the pulses show a double peak effect with a higher signal at the beginning of the pulse (n$^+$ side) and an a little bit lower at the end (p$^+$ side). But like mentioned before, this shape would change after the trapping correction.

The CCE for the same sensor at different annealing steps is shown in figure 7.12 as a function of the bias voltage. The CCE of electrons (a) shows a strong increase with in-

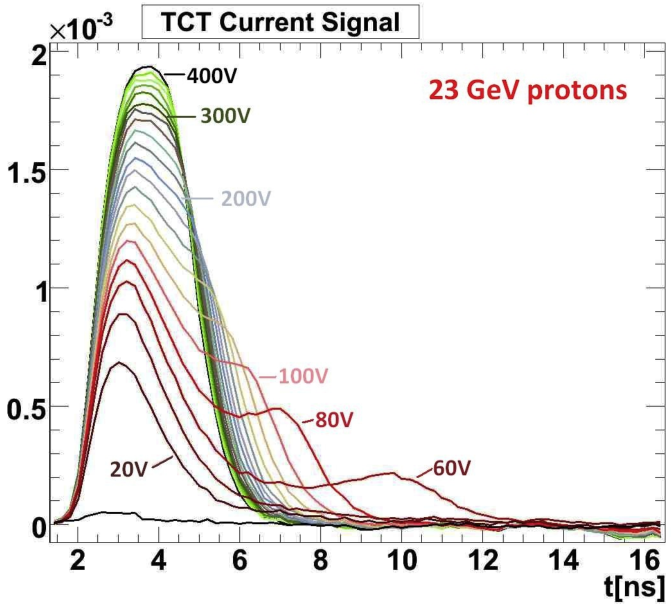

Figure 7.10: TCT pulse evolution with increasing bias voltage in 20 V steps up to 400 V for MCZ200N irradiated with $\Phi_{eq} = 3.8 \times 10^{14}$ cm^{-2} 23 GeV protons annealed to 1 minute at 80 °C , measured at 0 °C, illumination from front. The sensor is fully depleted at 100 V.

creasing bias voltage up to 100 V. Then the efficiency raises slightly up to 600 V. With larger annealing times the maximum efficiency gets higher, for 30 minutes at 80 °C at 500 V an efficiency of circa 90 % is achievable.

The CCE of holes (b) starts to increase rapidly for $U > U_{dpl} \approx 100$ V, which denotes the moment of contact of the two depletion regions grown from both sides of the sensor.

In summary, the MCZ200N diode shows a strong double peak effect. But with an electric field distribution with its maximum on the front. Therefore the sensor is not type inverted.

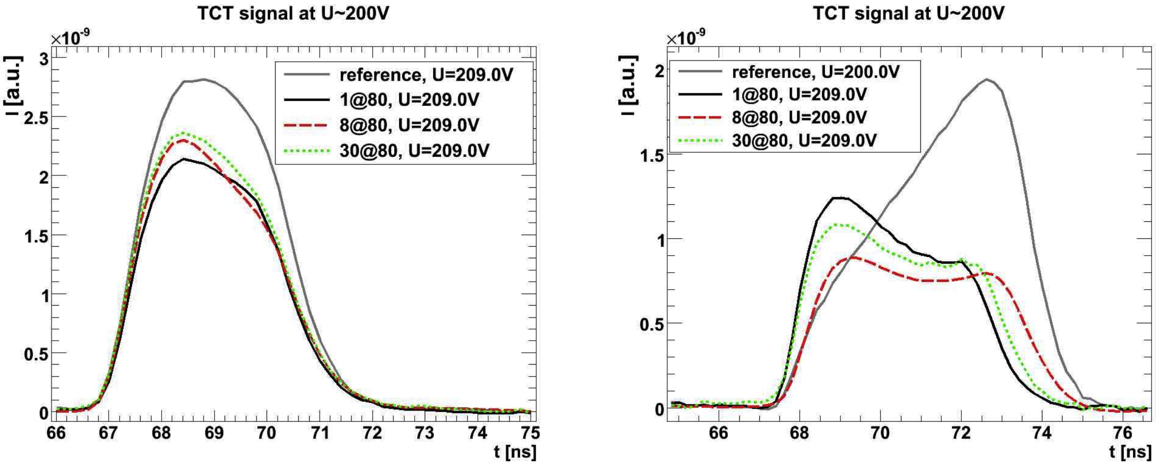

(a) Electron signal (b) Hole signal

Figure 7.11: TCT signals for MCZ200N after 23 GeV proton irradiation of $\Phi_{eq} = 3.8 \times 10^{14}$ cm^{-2}, annealed to 1, 8 and 30 minutes at 80 °C, TCT pulses taken for red laser illumination, (a) from the front (electrons) and (b) the back (holes) of the sensor.

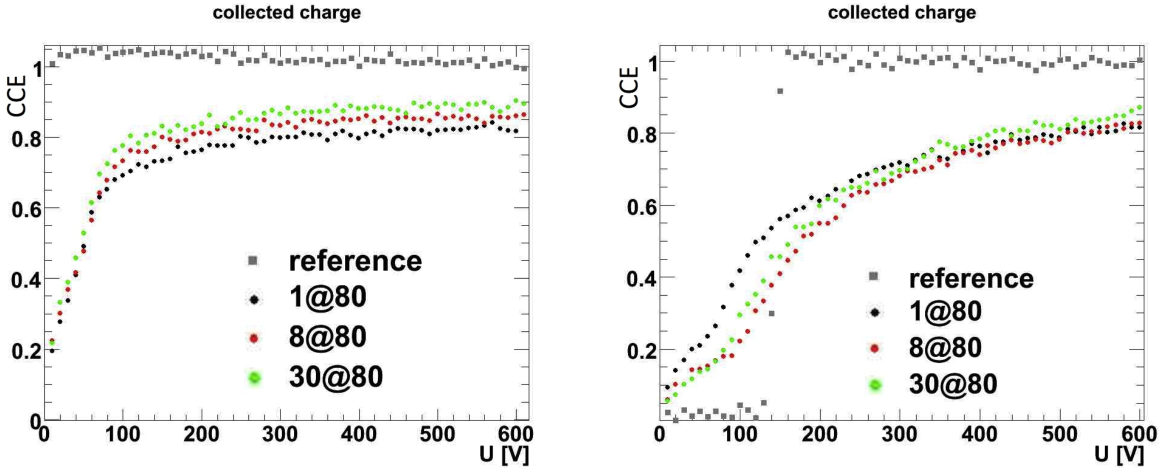

(a) Electron charge collection (b) Hole charge collection

Figure 7.12: CCE for red laser illumination, (a) from the front (electrons), and (b) the back (holes) of a MCZ200N sensor after 23 GeV proton irradiation of $\Phi_{eq} = 3.8 \times 10^{14}$ cm^{-2} annealed to 1, 8 and 30 minutes at 80 °C.

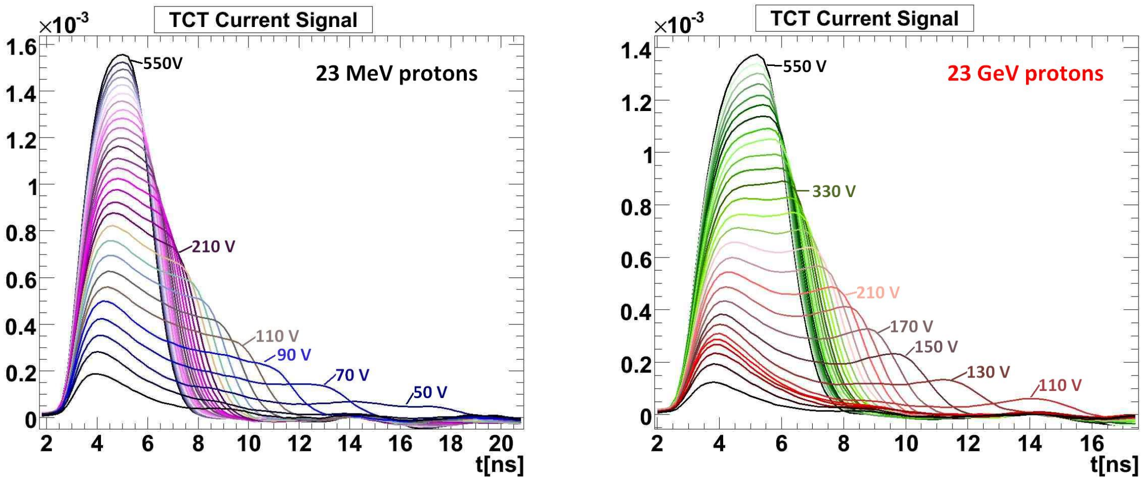

(a) Hole signal (b) Hole signal

Figure 7.13: Comparison of the evolution of TCT hole signals for MCZ200N irradiated with (a) 23 MeV protons, and (b) 23 GeV protons, $\Phi_{eq} = 2.4 \times 10^{14}$ cm^{-2} and $\Phi_{eq} = 3.8 \times 10^{14}$ cm^{-2}, annealed to 8 minutes at 80 °C, measured at 0 °C from 10 V up to 550 V in 20 V steps.

Comparison between 23 MeV and 23 GeV Proton Irradiations

In figure 7.13 the hole-signal evolution with increasing bias voltage is presented for the 23 MeV and 23 GeV irradiated MCZ200N diodes. The hole signals of the 23 MeV irradiated MCZ200N diode have a negative slope, thus the highest signal for short drift times occurs at the n$^+$ electrode. The sensor is type inverted.

The hole signals after 23 GeV irradiation show a double peak structure of the pulse shape, but for U >300 V the slope gets positive. The charge is collected at the p$^+$ electrode and the sensor stays n-type (no type-inversion).

In figure 7.14 the CCE is shown as a function of bias voltage for 23 MeV and 23 GeV proton irradiation. The CCE after 23 MeV proton irradiation compared to the CCE after 23 GeV proton irradiation of MCZ200N sensors describes a higher efficiency of the inverted sensor for electrons (a) and holes (b). This can be explained to some extent by the difference in fluence of $\Delta\Phi_{eq} = 1.4 \times 10^{14}$ cm^{-2}. But also might be affected by the proton energy, for prove further samples and measurements are needed.

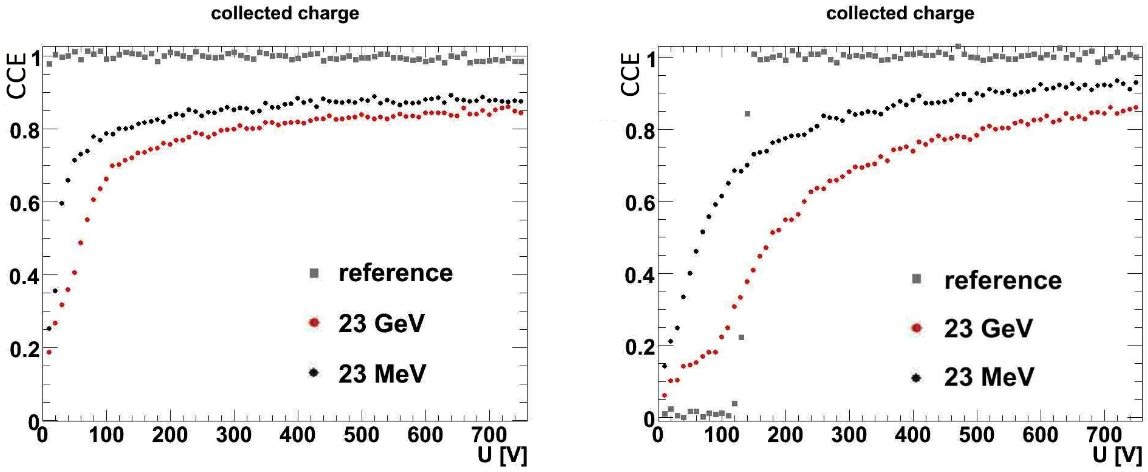

(a) Electron charge collection

(b) Hole charge collection

Figure 7.14: Comparison of CCE for (a) electron collection and (b) hole collection for MCZ200N irradiated with an equivalent fluence of $\Phi_{eq} = 2.4 \times 10^{14}$ cm^{-2} (23 MeV) and $\Phi_{eq} = 3.8 \times 10^{14}$ cm^{-2} (23 GeV), annealed to 8 minutes at 80 °C, measured at 0 °C.

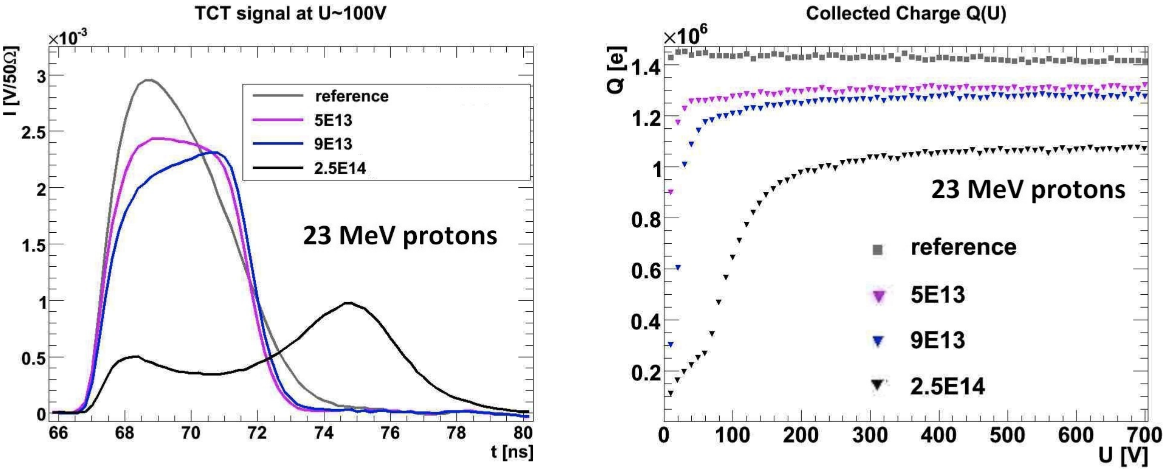

(a) Electron signal (b) Electron charge collection

Figure 7.15: FZ200N after different equivalent fluences of 23 MeV protons ($\Phi_{eq} = 5 \times 10^{13}$, 9×10^{13} and 2.5×10^{14} cm^{-2}), measured as irradiated at 0 °C after red laser illumination from the front.

7.3.2 Oxygen-rich Float Zone

23 MeV Proton Irradiation

Unfortunately for the FZ200N sensors it was not possible to generate hole signals because of the large deep diffusion layer on the back. The absorption length of the red laser is too short to create electron hole pairs in the active volume. Therefore only electron signals are presented.

TCT pulses and collected charge Q for FZ200N diodes after 23 MeV proton irradiation are presented in figure 7.15 for three different fluences. From the TCT pulses (a) it is observed that the signal amplitude decreases with increasing proton fluence. Furthermore, the maximum in the pulse shapes shift with larger fluences from the beginning to the end of the signal (n$^+$ electrode). Already after 9×10^{13} cm^{-2} 23 MeV proton fluence the slope of the TCT pulse is positive.

The collected charge as a function of the bias voltage (b) shows a fast increase for the two lower fluences and a rapid increase for the highest fluence of 2.5×10^{14} cm^{-2} after full depletion (U_{dpl} =120 V). The maximum achievable charge collection decreases with increasing fluence. The sensor irradiated with 2.5×10^{14} cm^{-2} collects around 1 million electrons, which corresponds to an electron collection efficiency of 65 %.

FZ200N undergoes type inversion between $3 \times 10^{13} > \Phi_{inv} < 9 \times 10^{14}$ cm^{-2}. This is consistent with the results from CV measurements $\Phi_{inv} = 0.7 \times 10^{14}$ cm^{-2}.

23 GeV Proton Irradiation

The TCT signals for a FZ200N diode irradiated with $\Phi_{eq} = 2.4 \times 10^{14}$ cm^{-2} 23 GeV protons are presented in figure 7.16 for an annealing of 8 minutes at 80 °C. The shapes of the pulses show a double peak up to 80 V (U$_{dpl}$=88 V), but the electron signal is for all bias voltages the highest at the beginning of the drift time (p$^+$ electrode). When taking trapping into account, the peak at the end of the drift time becomes higher, thus the double peak effect would become stronger. But the electric field remains stronger at the p$^+$ than at the n$^+$ side. Additionally, the annealing behavior of the FZ200N diode after a fluence of $\Phi_{eq} = 2.4 \times 10^{14}$ cm^{-2} is investigated by the TCT pulse shapes and the CCE for electron injection (see Appendix, figure 5).

FZ200N does not undergo type inversion after 23 GeV proton irradiation.

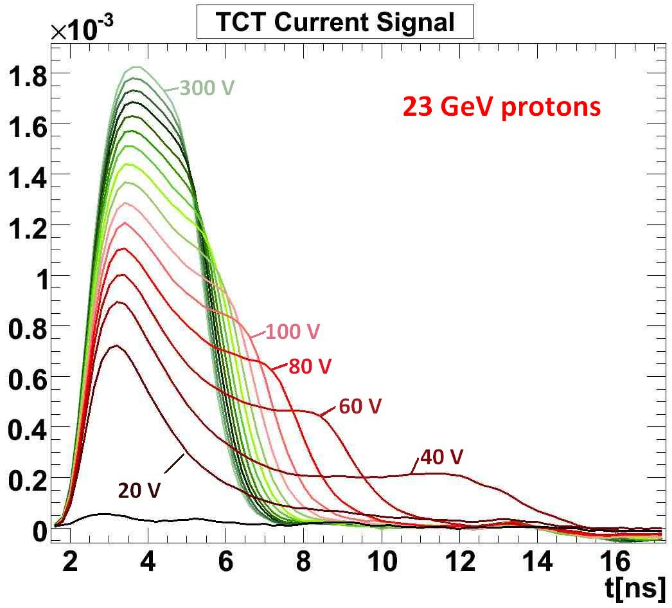

Figure 7.16: TCT pulse evolution with increasing bias voltage in 20 V steps up to 300 V for FZ200N irradiated with $\Phi_{eq} = 2.4 \times 10^{14}$ cm^{-2} 23 GeV protons annealed to 8 minutes at 80 °C , measured at 0 °C, illumination from the front.

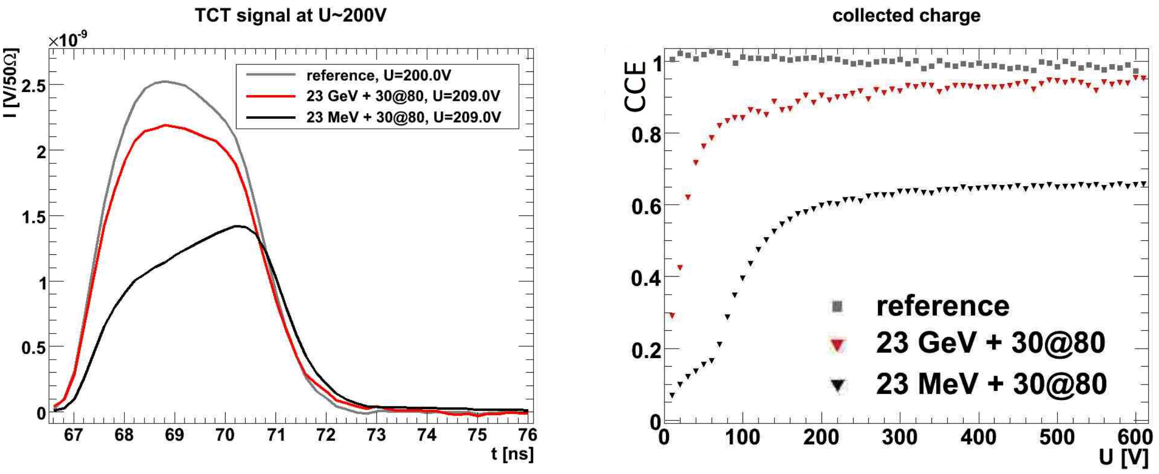

(a) Electron signal

(b) CCE (electron charge collection)

Figure 7.17: FZ200N after 23 MeV and 23 GeV proton irradiation of $\Phi_{eq} = 2.5 \times 10^{14}$ cm^{-2} and $\Phi_{eq} = 2.9 \times 10^{14}$ cm^{-2} after annealing to 30 minutes at 80 °C, measured at 0 °C.

Comparison between 23 MeV and 23 GeV Proton Irradiation

In comparison with the 23 MeV protons (see figure 7.17) the differences in pulse shapes and therefore in the electric field distributions are significant and also the charge collection efficiency is influenced by the proton energy. While an annealing of 30 minutes at 80 °C yields after 23 GeV proton irradiation a CCE of 90 %, the maximum efficiency of FZ200N after MeV irradiation does not exceed 60 %, also after annealing.

7.4 Conclusion from the Macroscopic Results

To make a reasonable conclusion it must be remembered what was expected for the radiation damage effects induced by protons of different energies. First within the community of the CMS tracker upgrade campaign no difference between 23 MeV and 23 GeV radiation damage was expected for the sensors were exposed to the same fluences when normalized to 1 MeV neutron equivalent values. Previous studies have shown, that especially for 23 MeV and 23 GeV protons no differences in the damage effects could be found for sensors manufactured on oxygen-lean high-resistivity FZ material [Aff10]. In this work differences between 23 MeV and 23 GeV proton irradiation are observed for MCz and also for FZ material.

Using macroscopic measurements it was observed that both the MCz and FZ oxygen-rich diodes undergo space charge sign inversion (SCSI) for 23 MeV proton irradiation like oxygen-lean ones, while for 23 GeV protons SCSI was not observed.

The current pulses recorded for MCZ200N and FZ200N by the TCT method for 660 nm laser light injection at the p^+ electrode show for bias voltages below and near to U_{dpl} a double peak shape after irradiation with protons of both energies. This double peak in the current pulse shape reflects a double peak electric field distribution. However, for 23 MeV protons the E-field maximum on the back (n^+ electrode) increases much faster with increasing bias compared to that at the p^+ electrode. Contrary to that, after 23 GeV proton irradiation the electric field strength on the front becomes larger with increasing bias voltage compared to the field on the back. This picture does not change considerably if charge carrier trapping would be taken into account.

The effect of the proton energy on N_{eff} is investigated as a function of the oxygen content and the producer of the Si sensors. In conclusion an oxygen dependence could be proven and a dependence on the producer excluded.

The results from the macroscopic measurements are summarized in table 7.2.

The results of U_{dpl} respectively N_{eff} extracted from CV measurements and the annealing studies allowed an extrapolation of the sensor performance to higher fluences. The slope of the N_{eff} versus Φ_{eq} (after inversion/minimum) in figure 7.18 shows that the 23 MeV proton irradiation leads to a stronger increase of U_{dpl} and N_{eff} with the fluence than the 23 GeV proton irradiation. For the CMS Phase II upgrade the strip sensors 20 cm from the interaction point must withstand a fluence of 3×10^{15} cm^2. The expected radiation field will not only consist of protons, therefore mixed irradiations with neutrons will be/are also performed by the tracker upgrade campaign. The influence of an additional neutron fluence on the already proton irradiated sensors will be an additional negative SC.

This negative SC has a different influence on a type-inverted sensor than on a non-type inverted one. U_{dpl} of a sensor, type-inverted after 23 MeV proton irradiation, will increase after neutron irradiation. U_{dpl} of a non-type inverted sensor, after 23 GeV protons, will decrease due to the negative SC introduced by the neutron irradiation.

Material	Proton energy	Φ_{eq} [cm^{-2}]	U_{dpl} [V]	Annealing behavior of N_{eff}	CCE [%]	Φ_{inv} [cm^{-2}]
HPK MCz	23 MeV	2.4×10^{14}	50	p-type	90	1.8×10^{14}
HPK MCz	23 GeV	3.8×10^{14}	110	n-type	80	—
RD50 MCz	23 MeV	4.5×10^{14}	150	p-type	70	2.0×10^{14}
HPK FZ	23 MeV	2.9×10^{14}	90	p-type	65	0.7×10^{14}
HPK FZ	23 GeV	2.4×10^{14}	100	n-type	80	—

Table 7.2: Summary of macroscopic results for different material and proton energies for fluences between 2 and 5×10^{14} cm^{-2}. U_{dpl} after irradiation taken after 8 minutes at 80 °C, CCE for electrons (illumination from the front) for 660 nm taken at 500 V.

A microscopic explanation for the influence of proton energies on the sensor properties could be, that either more acceptor-like defects or less donor-like ones are created after 23 MeV proton irradiation compared to 23 GeV. What one expects from lower energy is a larger ratio of point to cluster defects, because at lower energies the Coulomb scattering dominates resulting in recoil atoms with low energies which create predominantly point defects (see chapter 4.2). To study this, the Deep Level Transient Spectroscopy and the Thermally Stimulated Current Technique are used. In the following chapter you can find the results.

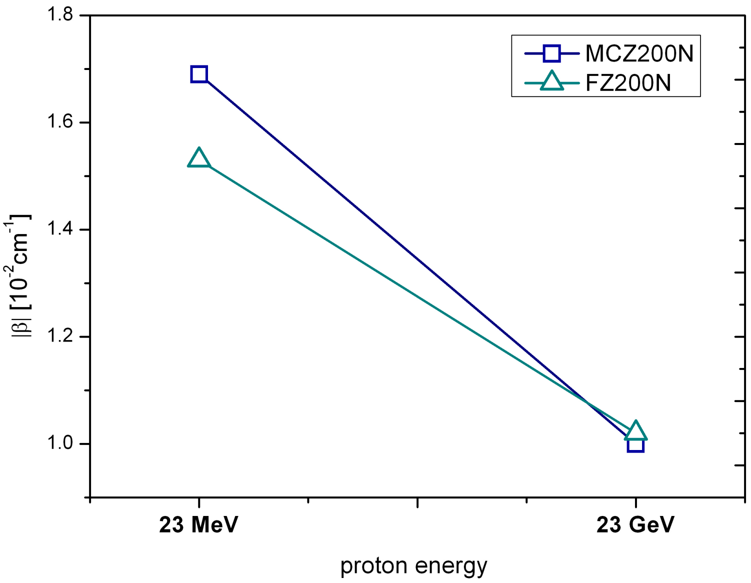

Figure 7.18: The slope of the $N_{eff}(\Phi_{eq})$ curve after the inversion respectively the minimum, for 23 GeV and 23 MeV proton irradiation, is given by the absolute value of β, see equation 5.1. This can be used for extrapolations of N_{eff}/U_{dpl} to higher fluences.

Chapter 8

Microscopic Results

This chapter addresses the identification and characterization of defects with impact on the space charge. We focus on the defect generation dependence on the energy of the irradiating particles, in particular on protons with different energies. In chapter 8.1 Deep Level Transient Spectroscopy (DLTS) spectra are presented for MCZ200N and FZ200N sensors. Both material defects and radiation induced defects created by 23 GeV protons are investigated and compared for MCz and FZ.
Afterwards Thermally Stimulated Current (TSC) measurements are presented in chapter 8.2. Here TSC spectra are shown for irradiated MCZ200N of 23 MeV and 23 GeV proton irradiation as well as RD50 MCz spectra after 23 MeV proton irradiation.

8.1 DLTS Measurements

The DLTS method allows to directly measure defect parameters. In the following, defect concentrations are presented extracted from DLTS spectra of non-irradiated sensors as well as of sensors irradiated with $\Phi_{eq} \approx 1 \times 10^{11}$ cm^{-2} 23 GeV protons.

8.1.1 Defects introduced during the Fabrication Processes

Several of the materials investigated in this work contain production-induced material defects, as seen previously for the materials from the same manufacturer (Hamamatsu Photonics) (as explained in section 3.1.1). The high oxygen concentration in MCz material leads to a generation of Thermal Donors (TD) during high temperature processes like the Thermal Double Donor E(61K) (compare [Jun11]). Thermal double donors (TDD) belong to a group of thermal donors, which are oxygen-related defects formed in oxygen-rich materials within a temperature range of 300-550 °C. These defects are mostly generated

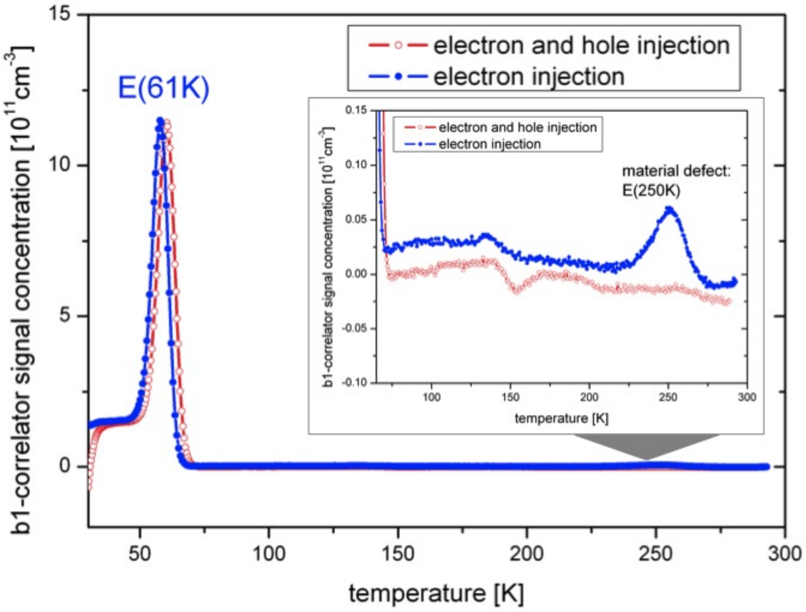

Figure 8.1: DLTS spectra illustrating the bulk defects in non-irradiated MCZ200N material, for electron traps (reverse bias U_R=-20 V, majority carrier pulse U_p= -0.1 V) and electron + hole traps (U_R=-20 V and injection pulse U_p= 3 V). The defect concentration is taken from the peak maximum of the b1-correlator.

during the production processes. The TDD exists in two different structural configurations: $TDD^{+/++}$ at $E_a = E_C - 0.07$ eV and $TDD^{0/++}$ at $E_a = E_C - 0.22$ eV [Jun11] [Pin09]. Figure 8.1 shows a DLTS spectrum for a non-irradiated Hamamatsu MCZ200N diode, for electron (majority carrier) and electron+hole injection. The electron trap E(61K) is seen in the first 80 μm from the front of the sensor. With a -20 V reverse bias 80 μm can be depleted, the SCR is calculated by the measured capacitance of 34 pF. The average concentration of the E(61K) is $N_{E(61K)} = 1.2 \times 10^{12}$ cm^{-3}, thus by assuming a constant distribution in the whole bulk volume the E(61K) concentration is contributing with 54 % to the initial doping concentration of $N_{eff,0} = 4.38 \times 10^{12}$ cm^{-3} (see table 3.1). Another observation is the material defect E(250K), that was detected only in a small concentration of about $\sim 10^9$ cm^{-3}.

For comparison, the DLTS spectra for FZ200N are shown in figure 8.2. The E(61K) defect is seen as well, but in a much smaller concentration than in MCZ200N. Here, the average concentration of E(61K) in the first 110 μm is about $N_{E(61K)} = 1.9 \times 10^{10}$ cm^{-3}. This is small compared to the average doping concentration $N_{eff,0} = 2.2 \times 10^{12}$ cm^{-3}. This difference between MCZ and FZ material was not expected, since the oxygen concentration for MCZ200N and FZ200N is similar. An interaction of those material defects with

irradiation-induced defects is not likely, but will be discussed in the following.
It has to be mentioned that the shift between the electron and electron+hole injection spectra for MCZ200N as well as for FZ200N is comprehensible. In this work the electron injection spectra are always measured with a tempscan from 300 to 5 K and the electron+hole injection spectra from 5 to 300 K. By starting the heating up process, the compressor is switched off at 5 K and the temperature rises immediately, but the sample temperature cannot follow the fast increase of the sample holder which is recorded by the temperature sensor. Therefore during the measurements at low temperatures the capacitance transients are actually recorded at higher values which shifts the electron+hole injection spectra to higher temperatures. The electron injection spectra are more precise in the low temperature range and therefore used for evaluation of the defect parameters. Below temperatures of 25 K all spectra are not meaningful, because the phosphorus dopants are not ionized, they "freeze-out" and the assumption that $N_t << N_{eff}$ is not valid anymore. Therefore all spectra are shown for the temperature range of 25-300 K.

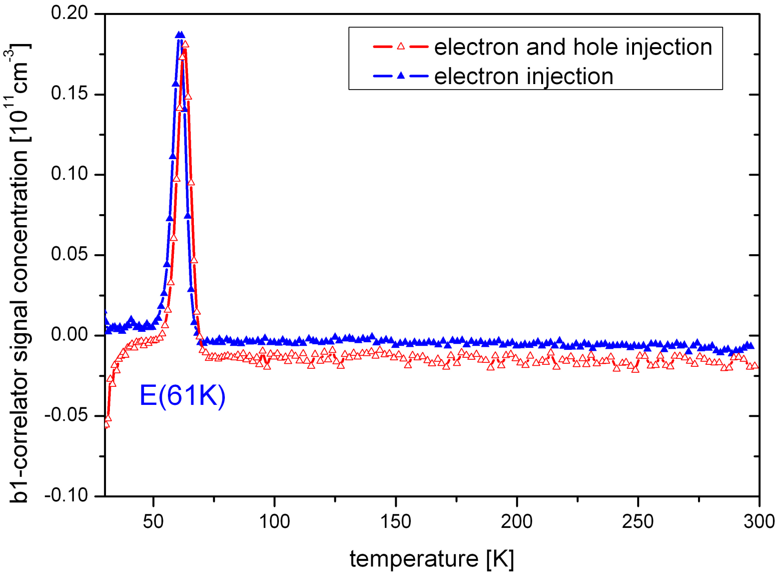

Figure 8.2: DLTS spectra illustrating the bulk defects in non-irradiated FZ200N material, for electron traps (U_R=-20 V and U_p= -0.1 V) and electron and hole traps (U_R=-20 V and U_p= 3 V). The defect concentration is taken from the peak maximum of the b1-correlator.

8.1.2 23 GeV Proton Irradiation

Both above mentioned materials are investigated by means of DLTS after $\Phi_{eq} \approx 1{-}2{\times}10^{11}$ cm^{-2} 23 GeV proton irradiation. Defect concentrations of electron and hole traps have been investigated.

MCZ200N

The DLTS spectra for a MCZ200N diode are presented in figure 8.3 for a fluence of $\Phi_{eq} = 1.8 \times 10^{11}$ cm^{-2} 23 GeV protons. The upper figure (a) presents electron traps (electron injection) while a mixture of electron and hole traps (electron and hole injection) is seen in the lower figure (b). The results from the non-irradiated sensor are shown as solid black line, directly after irradiation as blue (e$^-$ injection)/grey (e$^-$ and h$^-$ injection) and the annealing steps of 8 minutes at 80 °C as a dashed purple/green line and the 15 minutes at 80 °C as a dotted-dashed pink/cyan line. The electron traps: VO, V$_2$ and E4 (V$_3^{=/-}$)/E5 (V$_3^{-/0}$) appear as a result of the irradiation. The V$_2^{=/-}$ amplitude increases with annealing. That is a typical effect seen in neutron-irradiated diodes, which is caused by a reduction of the "cluster potential barrier". The so-called "cluster effect" describes the potential barrier surrounding clusters, which leads to a reduced occupation of the V$_2^{=/-}$ [Mon02]. The broad peak at ~210 K is a superposition of V$_2^{-/0}$, E5 and the E(205a) defect (see [Mol99], [Jun11]). E4/E5 belong to V$_3$ in different charge stages E4=V$_3^{=/-}$ and E5=V$_3^{-/0}$. The V$_3$ is a bistable defect, which transforms with annealing of 80 °C from planar to the fcc configuration. The E5 is responsible for a part of the dark current, for more details see [Neu10]. None of these defects has an impact on the SC (see also [Jun11]). An increase of the peak of E(61K) with irradiation and with annealing ($\mathrm{N}_{t,15min} - N_{t,non-irr} = 0.32 \times 10^{12}$ cm^{-3}) is observed.

The C$_i$O$_i$ defect appears after irradiation for e$^-$ and h$^+$ injection (figure 8.3b). The concentration increases with annealing due to the available carbon interstitials in the silicon which then can react with the oxygen. The signal amplitude of E(61K), however, stays constant. This indicates that the E(61K) after irradiation could be a superposition of the material defect TDD with a different radiation-induced defect. A possible candidate would be the IO$_2$ defect [Hoe07] or the bistable donor in the configuration BD$_A$ as observed in TSC spectra [Pin09].

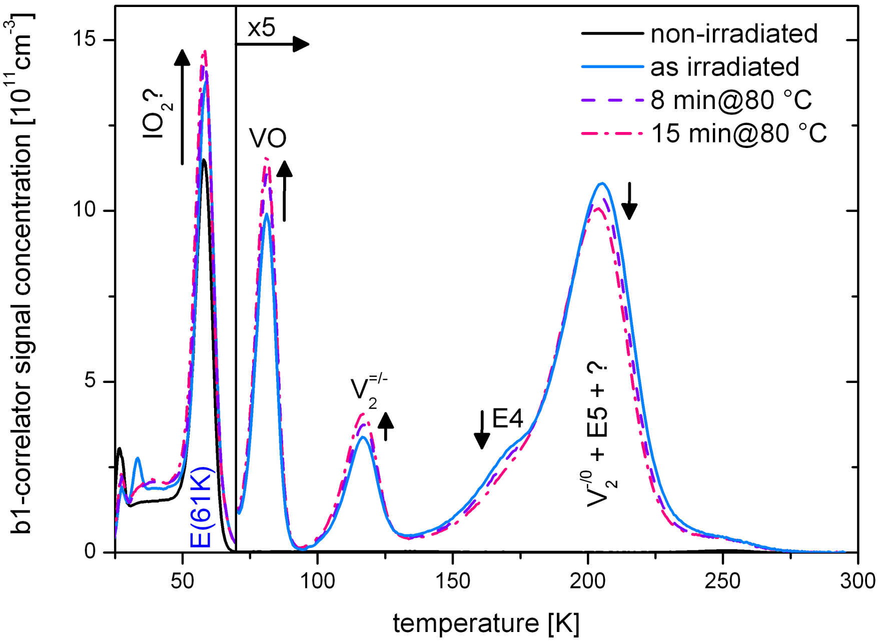

(a) Electron injection

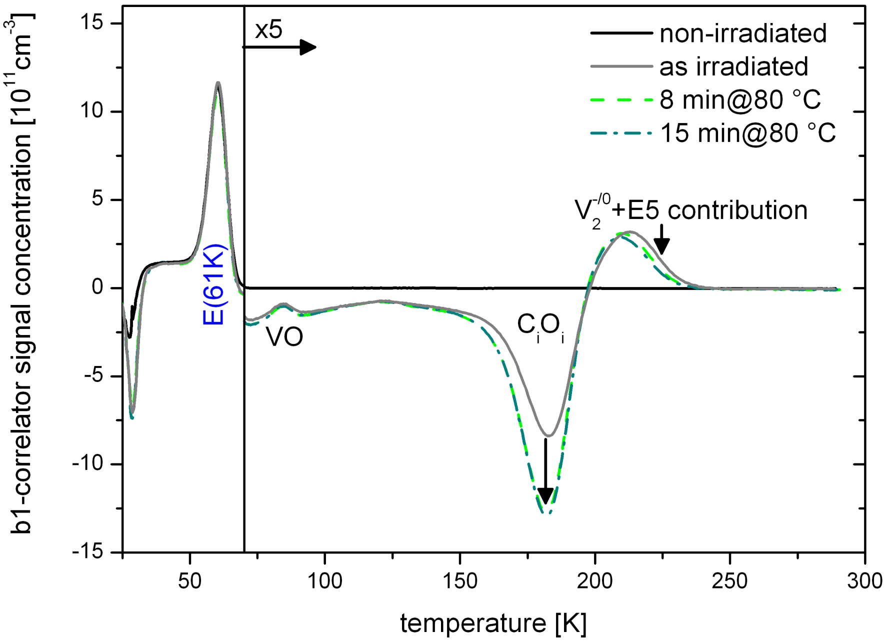

(b) Electron and hole injection

Figure 8.3: DLTS spectra illustrating the bulk defects in MCZ200N material irradiated with $\Phi_{eq} = 1.8 \times 10^{11}$ cm^{-2} 23 GeV protons for electron traps (U$_R$=-20 V and U$_p$= -0.1 V) and electron and hole traps (U$_R$=-20 V and U$_p$= 3 V).

FZ200N

The radiation induced defects in the FZ200N diode after $\Phi_{eq} = 1.1 \times 10^{11}$ cm^{-2} 23 GeV proton irradiation are shown in figure 8.4. For the non-irradiated sensor the spectra are shown as solid black lines, for the diode as irradiated as solid blue/grey line and for annealing steps at 80 °C: 6 minutes as dashed purple/green line, 15 minutes as dash-dotted pink/cyan line and 30 minutes as dotted light-grey/orange line. In the electron spectra (see figure 8.4a) the E(61K) peak increases with irradiation and annealing up to 6 minutes at 80 °C and decreases after 30 minutes at 80 °C ($\mathrm{N}_{t,6min} - N_{t,non-irr} = 6 \times 10^{10}$ cm^{-3}). The VO and V_2 defects appear during irradiation and change their concentrations slightly during the annealing. The E4 and E5 show a strong annealing effect. Possibly the E(30K) donor as observed in TSC spectra (see chapter 8.2) appears at 37.5 K in the DLTS spectrum. This defect overlaps with another electron trap at 33 K in the as irradiated spectrum, but this defect disappears after a few minutes of annealing. As expected for the E(30K) defect the concentration increases with annealing time to 1.9×10^{10} cm^{-3} after 30 minutes at 80 °C. This behavior is also observed for the overlapping electron and hole traps, see figure 8.4b. The concentration of E(61K) does not change in the DLTS spectra after electron and hole injection, which indicates that the E(61K) after electron injection is not the same after irradiation. Again the $\mathrm{C}_i\mathrm{O}_i$ appears, but decreases with annealing times larger 6 minutes at 80 °C, which could be an artifact due to annealing of the E5. Because the $\mathrm{C}_i\mathrm{O}_i$ amplitude is influenced by the broad peak of $\mathrm{V}_2^{-/0}$+E5 and E(205a).

Comparison of MCZ200N and FZ200N

The DLTS spectra reveal a high thermal double donor (E(61K)) concentration in the MCZ200N diode before irradiation. This donor is also found in the FZ200N diode but in a much smaller concentration. After irradiation both sensors show an increase of the E(61K) peak, which is nearly 20 times higher for the MCZ sensor. If this increase is due to the IO_2 induced by irradiation, the higher concentration in MCz can be explained by the higher oxygen concentration. Generally, defects created by the 23 GeV proton irradiation appear in the FZ in a much smaller concentration then in the MCz material. On the one hand this is an effect of the 60 % lower 23 GeV proton fluence and on the other hand of the higher impurity content in MCZ which seems to amplify the generation of the TDD and other defects. The $\mathrm{V}_2^{-/0}$+E5+E(205a) concentration should be the same in MCZ200N and FZ200N if normalized to the same fluence, because they are intrinsic defects. The same would hold for the $\mathrm{V}_2^{=/-}$, while the VO could be different because of the slightly difference in oxygen content.

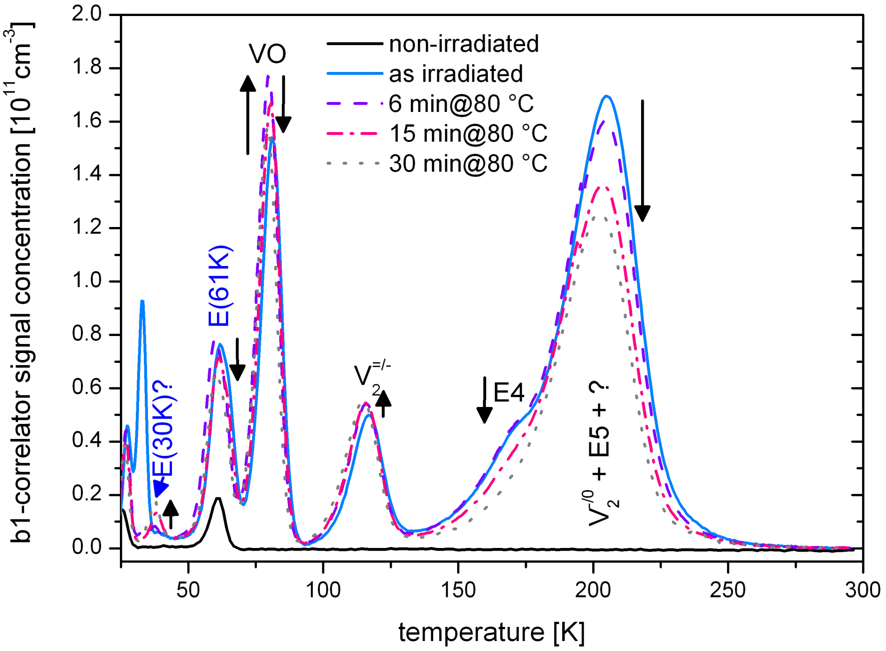

(a) Electron injection

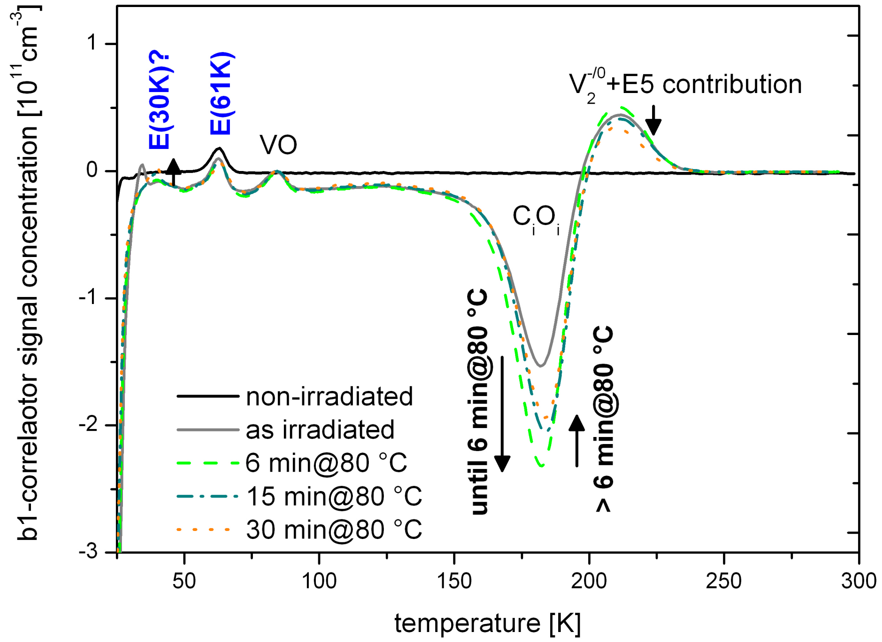

(b) Electron and hole injection

Figure 8.4: DLTS spectra illustrating the bulk defects in FZ200N material irradiated with $\Phi_{eq} = 1.1 \times 10^{11}$ cm^{-2} 23 GeV protons for electron traps (U$_R$=-20 V and U$_p$= -0.1 V) and electron and hole traps (U$_R$=-20 V and U$_p$= 3 V).

8.2 TSC measurements

The TSC measurements concentrate on the radiation-induced defects with impact on the SC. Therefore the known defects with impact on the SC are described in following:

Donors

- E(30K): The labeling uses an E for an electron trap and the temperature where the defect peak appears in the TSC spectrum (30 K). This defect is a shallow donor showing enhanced field emission (Poole-Frenkel effect) and is characterized to be very likely a cluster related defect [Rad12], because it does not appear after Co-γ or low energy electron irradiation. The E(30K) is a candidate to be reason for the beneficial annealing and was first recorded by [Mol99] as E(28K) with $E_a = E_C - 0.079$ eV, $\sigma_n = 1.68 \times 10^{-14}$ cm^2. Later, more detailed characterizations were performed by [Jun11] and [Pin06] with the results: $E_a = E_C - 0.1$ eV, $\sigma_n = 2.3 \times 10^{-14}$ cm^2.

- BD: The BD center is a bistable point defect in the upper half of the band gap, which is generated in oxygen-rich material and shows also the Poole-Frenkel effect. It appears in two charge states the $BD_A^{0/++}$ and $BD_B^{+/++}$ [Fre07] after Co-γ, electron and hadron irradiation. The BD center is associated to the thermal double donor (TDD2 [Pin09]) because of its bistability with a lower introduction rate for hadron irradiated sensors, donor activity and energy levels:
  $BD_A^{0/++}$: $E_a = E_C - 0.26$ eV, $\sigma_n = 6 \times 10^{-15}$ cm^2 and
  $BD_B^{+/++}$: $E_a = E_C - 0.15$ eV.

Acceptors

A group of deep acceptors was discovered and characterized by [Mol99] and [Pin09] and described in more detail by [Jun11]. These defects are cluster related and very likely independent of the material type.

- H(116K): $E_a = E_V + 0.33$ eV, $\sigma_p = 4 \times 10^{-14}$ cm^2
- H(140K): $E_a = E_V + 0.36$ eV, $\sigma_p = 2.5 \times 10^{-15}$ cm^2
- H(151K): $E_a = E_V + 0.42$ eV, $\sigma_p = 2.3 \times 10^{-14}$ cm^2

Previously, the defect generation after 23 GeV proton irradiations was studied in detail and compared to the radiation damage caused by neutron irradiation. Within those studies the so-called *compensation effect* was investigated [Jun11]. This compensation effect explains the difference between the effective doping concentration as seen after neutron and 23 GeV proton irradiation. Basically, mainly deep acceptors (H(116K), H(140K) and H(151K)) are generated after neutron irradiation, generating a negative SC. While after proton irradiation a high amount of positive SC is generated by shallow donors (E(30K) and BD-center), see figure 8.5. After 23 GeV proton irradiation the positive "compensates" the negative SC. This effect is held responsible for epitaxial material from CiS to not undergo type inversion after 23 GeV proton irradiation. While the smaller generation of the E(30K) (in comparison to the H-defects) leads to type inversion after neutron irradiation.

In the following the defects created by 23 MeV proton irradiation in oxygen-rich materials are presented. The expectation is to find a similar defect generation as after neutron irradiation, or at least a higher acceptor or smaller donor generation then after 23 GeV proton irradiation.

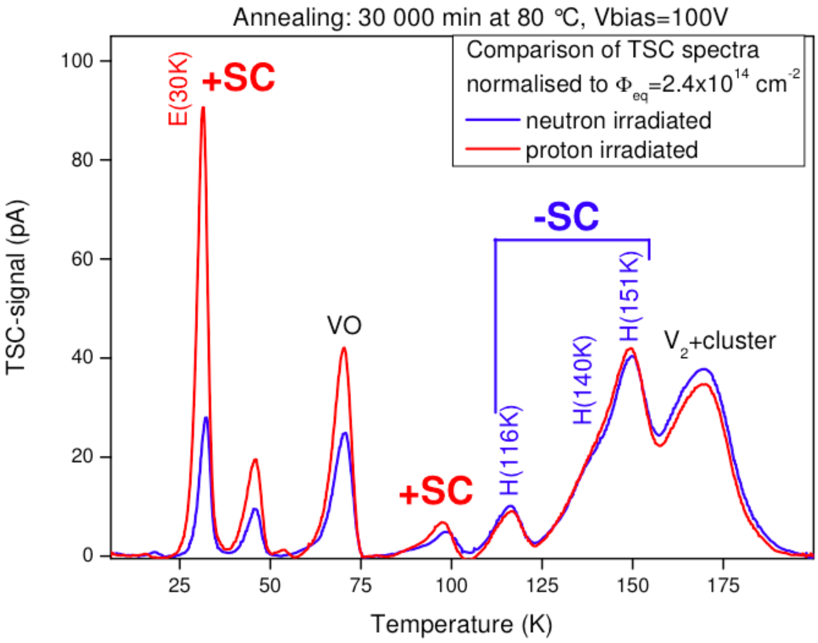

Figure 8.5: TSC spectra for oxygenated epitaxial pad diodes after $\Phi_{eq} = 2.4 \times 10^{14}$ cm^{-2} neutron and 23 GeV proton irradiation, annealed to 30000 minutes at 80 °C, $U_{rev} = 100$ V, taken from [Pin09].

8.2.1 MCZ200N irradiated with 23 MeV Protons

Three 23 MeV proton fluences of $\Phi_{eq} = 3.5$, 5.8 and 9.5×10^{13} cm^{-2} were available for defect analysis by means of TSC measurements. As shown in section 7.2 a fluence of $\Phi_{inv} = 1.75 \times 10^{14}$ cm^{-2} of 23 MeV protons is needed to invert MCZ200N sensors. Thus none of the sensors under investigation in this section is inverted yet.

In figure 8.6 the TSC spectrum is given for the MCZ200N diodes irradiated with three different fluences. Measurements were performed after an annealing of 8 minutes at 80 °C and the charge injection was done at 20 K to ensure a filling current of 1 mA. The defect concentrations in the TSC spectra, reflected by the area of the defect peak, increase with fluence. The donor E(30K) and the BD-center appear, but the BD_B might only be visible in the shoulder of the IO_2. In contrast to previous measurements, a stable (not vanishing with the annealing) hole trap can be observed at 40 K. The thus H(40K) labelled defect has a high defect concentration making it a candidate for the origin of the negative SC in 23 MeV irradiated oxygen-rich sensors. Therefore, H(40K) will be analyzed in more detail in the following section.

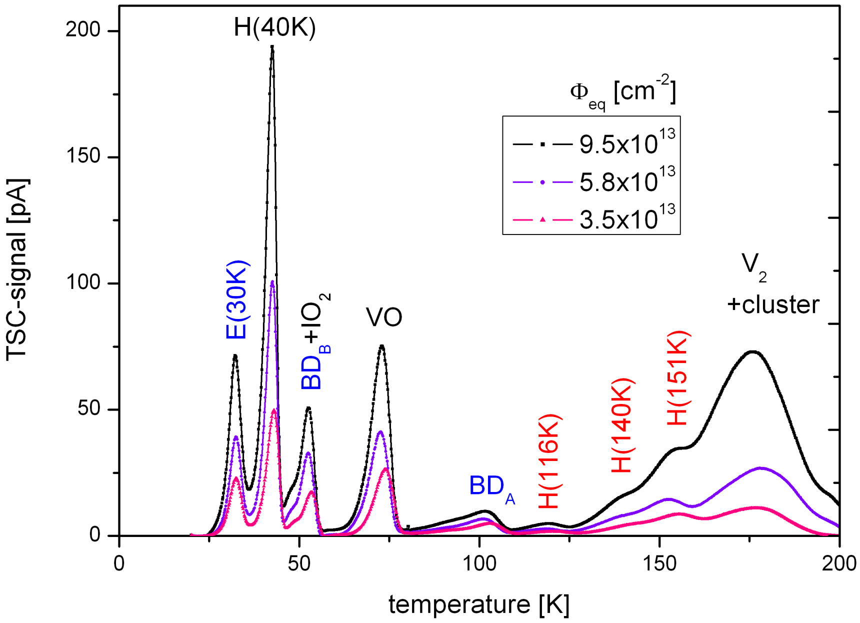

Figure 8.6: TSC spectra for MCZ200N sensor for different fluences after an annealing of 8 minutes at 80 °C, measurement parameters: $T_{fill} = 20$ K, $t_{fill} = 60$ s, $I_{fill} = 1$ mA and $U_{rev} = 300$ V.

N$_{eff}$ calculated from Defect Concentrations

The shape of the defect peaks in the spectra are simulated to extract the defect concentrations, activation energy and capture cross section of the defects. The defect concentrations of the donors and acceptors and the H(40K) are shown in figure 8.7a as a function of the 23 MeV proton fluence. The red full squares denote the concentration of acceptors and the blue squares the one of donors. The lines are linear fits, their slopes describe the introduction rates of the defects. The introduction rates (IR) are shown in table 8.1. The highest IR is found for the H(151K) defect. It has to be mentioned that the concentrations of E(30K) and H(151K) increase strongly with annealing, which has a strong impact on the IR calculated after annealing times larger than 8 minutes at 80 °C.

The effective doping concentration is calculated by summing the initial doping concentration and the defect concentrations to

$$N_{eff}^{calc} = N_{eff,0} + N_{donors} - N_{acceptors} \tag{8.1}$$

with N$_{donors} = \sum \left(N_t^{E(30K)}, N_t^{BD_A}, N_t^{BD_B} \right)$ and N$_{acceptors} = \sum \left(N_t^{H-defects} \right)$.
The evolution of the donor and acceptor concentration as well as N$_{eff}^{calc}$ with the proton fluence is shown in figure 8.7b. Because of the higher IR of acceptors compared to donors, the negative space charge dominates with increasing proton fluence, which results in type inversion after $\Phi_{inv}^{calc} = 2.2 \times 10^{14}$ cm^{-2}. The calculated type inversion occurs 4×10^{13} cm^{-2} below the value extracted from CV measurements, which can be explained by the *donor removal*. Radiation induced vacancy defects create the V$_i$+P$_s$ → VP complex with phosphorus inactivating the P$^+$ atom. In oxygen-rich material this reaction ends with the generation of V$_i$+O$_i$ → V$_i$O$_i$. The more oxygen-rich the material the more likely is the formation of VO instead of VP. Since V$_i$O$_i$ does not influence the electrical properties of the sensor, while preventing positive SC from VP, oxygen-rich Si offers a significant benefit compared to oxygen-lean material.

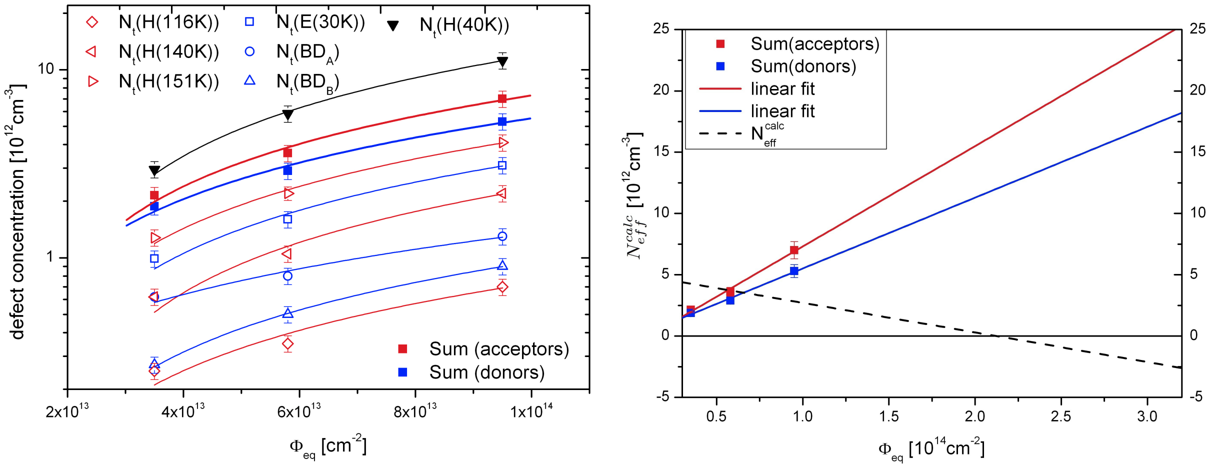

(a) (b)

Figure 8.7: Defect concentrations for MCZ200N after 8 minutes at 80 °C annealing shown as a function of Φ_{eq} for 23 MeV proton irradiation (a). Acceptor/donor concentration and the calculated effective doping concentration by equation 8.1 is shown in (b) as a function of Φ_{eq} as well as the extrapolation to higher fluences by linear fits.

Defects	IR [cm^{-1}]	
H(40K)	0.1399 ± 0.0045	
		IR (**Donors**) [cm^{-1}]
E(30K)	0.0367 ± 0.0034	0.0577 ± 0.0055
BD$_A$	0.0118 ± 0.0014	
BD$_B$	0.0106 ± 0.0002	
		IR (**Acceptors**) [cm^{-1}]
H(116K)	0.0080 ± 0.0012	0.0819 ± 0.0077
H(140K)	0.0278 ± 0.0030	
H(151K)	0.0482 ± 0.0026	

Table 8.1: Introduction rates (IR) of defects with impact on the space charge and of the H(40K) defect, extracted from MCZ200N sensors irradiated with 23 MeV protons, after annealing 8 minutes at 80 °C.

Analysis of H(40K)

As mentioned before, the H(40K) defect appears after 23 MeV proton irradiation in an extraordinary high concentration. Additionally, a shift of the peak maximum by different bias voltages and therefore different electric field strengths is observed. This is an indicator for the Poole-Frenkel effect, which again suggests a defect that is charged at room temperature and therefore has impact on the SC. In figure 8.8 the TSC spectra for MCZ200N irradiated with 9.5×10^{13} cm^{-2} 23 MeV protons are shown for different reverse biases. Two effects are observed: Firstly, an increase of the dark current and the overlapping deep defects and an increase of VO's peak height. Secondly, the shift of the peak maxima to lower temperatures with increasing bias voltage of the E(30K), H(40K), BD$_A$ and H(116K) peaks. While the shift of the BD$_B$ is mostly covered by the IO$_2$, the shift of the H(140K) and H(151K) is concealed by the dark current. The shift is strongest for the E(30K) (see figure 8.9), which also shows a change in peak shape. The E(30K) peak broadens and decreases with larger bias voltages. While the H(40K) peak increases up to 200 V and then shifts with a constant peak height and width.

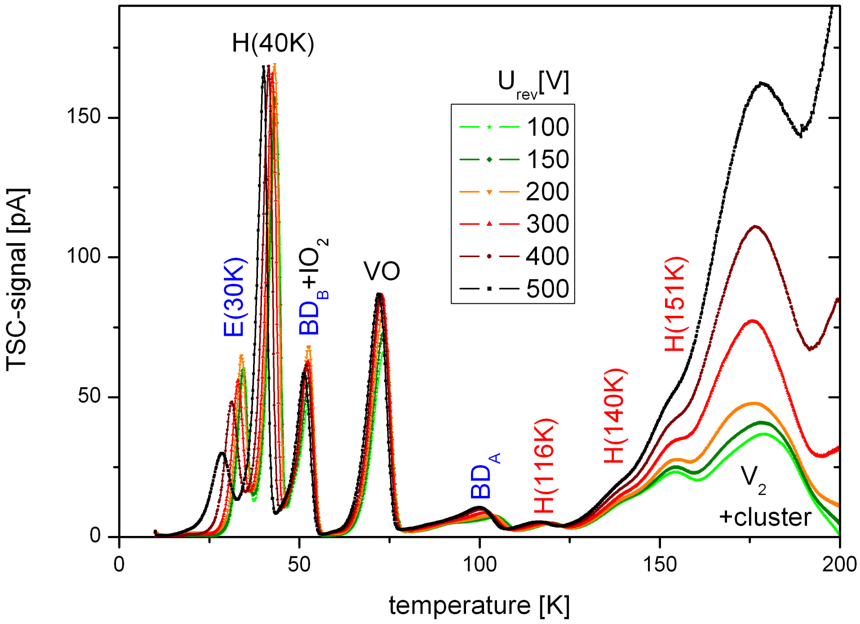

Figure 8.8: TSC spectra of MCZ200N irradiated with $\Phi_{eq} = 9.5 \times 10^{13}$ cm^{-2} 23 MeV protons annealed to 8 minutes at 80 °C for various reverse bias voltages from 100 V up to 500 V, measurement parameter: T$_{fill}$ = 10 K, t$_{fill}$ = 30 s and I$_{fill}$ = 1 mA.

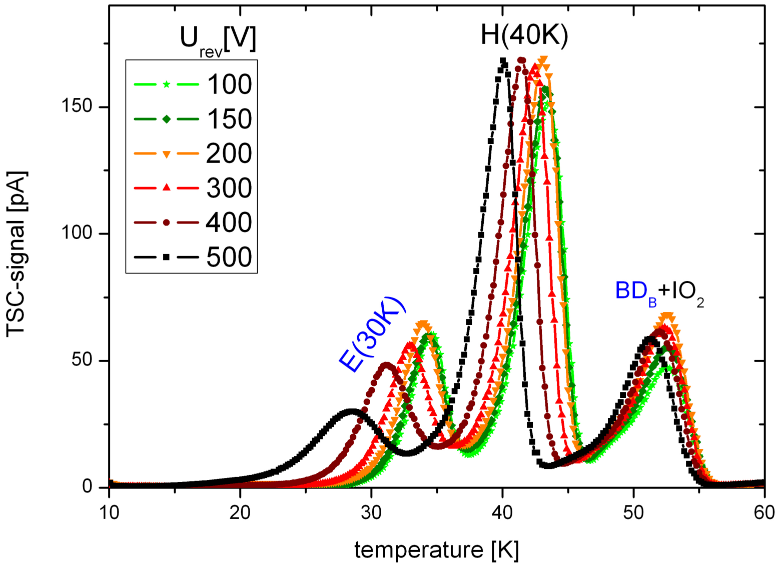

Figure 8.9: Field-emission effect of E(30K) due to the Poole-Frenkel effect and H(40K), same measurements as figure 8.8.

Parameters of Defects with Field Emission Effect

To determine the defect parameters of defects with field-emission effect the defect peak has to be analyzed for different reverse voltages. The emission rate dependence on the electric field are described by equation 4.13 in section 4.4 and the emission rate without applied electric field is approximated by equation 4.14. This parameter depends on the capture cross section and the activation energy of the defect level. To calculate the activation energy for E=0 V of the E(30K) and H(40K), the field dependent activation energy is simulated with constant capture cross section (taken from [Mol99]) and plotted as a function of the electric field in figure 8.10a. The E(30K) shows a larger variation of ΔE_a than the H(40K) and both curves do not look linear. The activation energies are calculated to $\Delta E_a(E(30K)) = -0.102 \pm 0.002$ eV and $\Delta E_a(H(40K)) = 0.108 \pm 0.003$ eV. For the sake of completeness, also the capture cross section was varied for a fixed ΔE_a to simulate the shifting defect peaks of E(30K) and H(40K). The results are presented in figure 8.10b and the capture cross sections are calculated to $\sigma_n(E(30K)) = 1.2 \pm 0.8 \times 10^{-13}$ cm^2 and $\sigma_p(E(40K)) = 4.3 \pm 3.9 \times 10^{-15}$ cm^2.

The defect concentration is not affected by field-emission effects, thus N_t should not change with increasing electric field. This is examined for the E(30K) and H(40K) concentrations

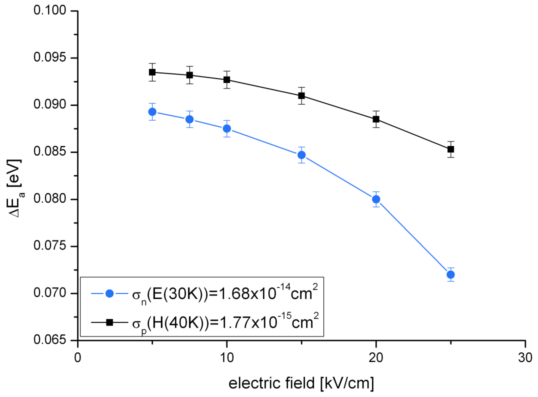

(a) Activation energy

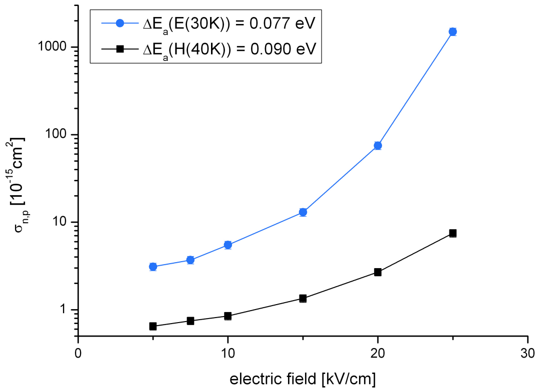

(b) Capture cross section

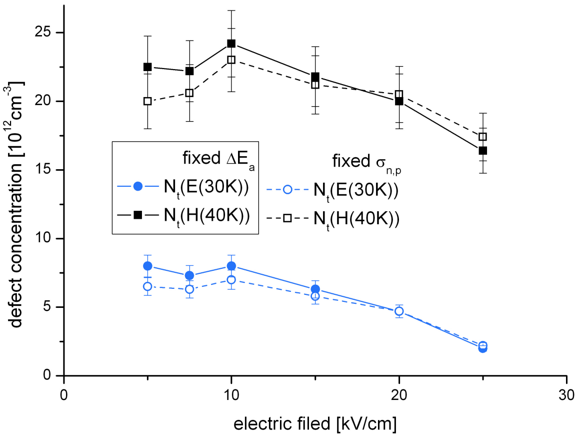

(c) Defect concentration

Figure 8.10: Activation energy calculated with fixed capture cross section for E(30K) and H(40K) as a function of the electric field (a), and increase of the capture cross section for fixed activation energy with increasing electric field (b). Comparison of corresponding defect concentrations of E(30K) and H(40K) as function of the electric field (c) for assuming the change of activation energy and the capture cross section from figure (a) and (b).

for fixed ΔE_a and $\sigma_{n,p}$ and presented in figure 8.10c. The results of the simulations for varying $\sigma_{n,p}$ and ΔE_a correspond with each other. The H(40K) concentration stays constant within the error bars, while the E(30K) concentration shows a decrease with increasing electric field. This can be explained by the fact, that the E(30K) peak height decreases and peak width increases with increasing electric field. The broadening of the peak cannot be simulated accurately. This lead to an increase of the error on the fit.

In the following the defect concentrations at 300 V respectively 15 kV/cm are taken for the calculations.

Annealing Behavior of Defects

For the 23 MeV fluences of 3.5 and 9.5×10^{13} cm^{-2} the annealing of the defects is recorded by TSC-signals up to an annealing of 30 minutes at 80 °C.

Sample irradiated with $\Phi_{eq} = 3.5 \times 10^{13}$ cm^{-2}

The spectra for the low fluence are shown in figure 8.11. Except for "as irradiated" all spectra have been recorded after a forward filling current of 1 mA at 20 K. Therefore the peak heights should only be compared for the measurements after annealing at 80 °C. The as irradiated spectrum shows a peak at 25 K, which is an electron trap (see figure 8.12) and which vanishes within the first minutes of annealing. Also the E(30K) is already seen, however the peak is quite small. All spectra after annealing at 80 °C show a much higher peak of the E(30K) (increasing with larger annealing times) compared to the H-defects. That was seen previously and led to the assumption that this behavior of the donor is responsible for the beneficial annealing [Jun11]. The H(40K) shows a much smaller increase, like the BD_B+IO_2. The VO slightly decreases while the BD_A concentration stays constant. The concentration of the H-defects, strongest the H(151K), increase. This is visible although the V_2+cluster peak decreases, which has an impact on the H-defects peak height because of their overlap.
To assign the peaks to special defects, separate charge carrier injection of electrons and holes are used: By illumination with a green laser diode of 660 nm on the front (p^+ electrode) *electron injection* and the back (n^+ electrode) *hole injection*. The spectra recorded after electron and hole injection for different annealing steps are presented in figure 8.12. Here, the electron traps appear in blue and hole traps in red. The peak heights are not comparable, as already described in section 6.3.2. Moreover, the electron current was always three orders of magnitude higher than the hole current. However, a qualitative statement can be made. The donors (E(30K) and BD center) can be identified as well as the acceptors (H(151K), H(140K) and H(116K)). Additionally the hole trap H(40K) could be identified and another hole trap is visible beneath the V_2+cluster peak. This defect might be the H(220K), which was previously recorded by [Mol99] and in [Jun11] identified as a current generator in p-type silicon sensors. It could also be that this hole trap has an impact on the SC.

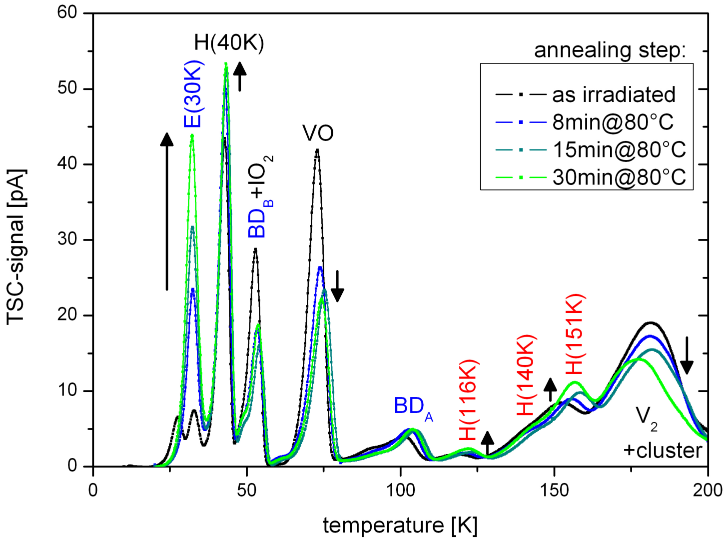

Figure 8.11: Evolution of TSC spectra during the annealing at 80 °C for MCZ200N irradiated with $\Phi_{eq} = 3.5 \times 10^{13}$ cm^{-2}, measurement parameter: T$_{fill}$ = 10 K (as irradiated) all others 20 K, t$_{fill}$ = 60 s, I$_{fill}$ = 0.87 mA (as irradiated) all others 1 mA and U$_{rev}$ = 300 V.

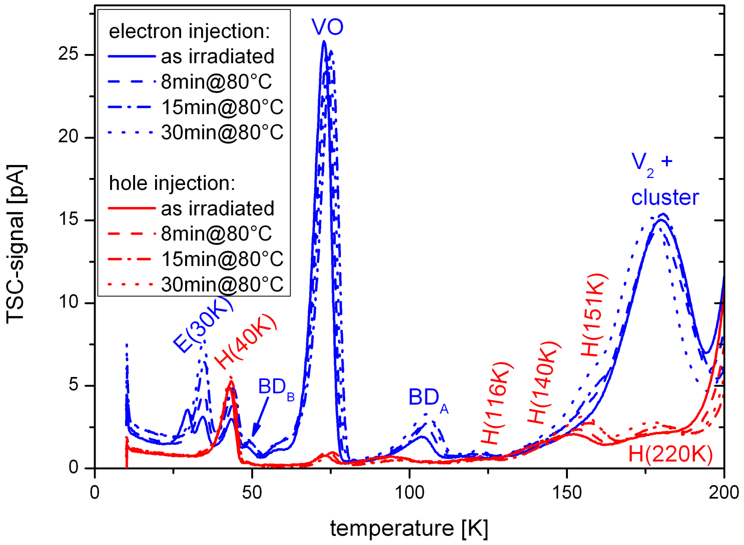

Figure 8.12: TSC-spectra for $\Phi_{eq} = 3.5 \times 10^{13}$ cm^{-2} after injection of electrons and holes separately with a green laser diode (530 nm) from the front and from behind to identify electron and hole traps, measurement parameters: T$_{fill}$ = 10 K, t$_{fill}$ = 30 s, I$_{fill}$ = (10 − 100) nA (electron injection) a few pA (hole injection) and U$_{rev}$ = 300 V.

Sample irradiated with $\Phi_{eq} = 9.5 \times 10^{14}$ cm^{-2}

The high fluence spectra for different annealing steps are shown in figure 8.13. This time all spectra were recorded after a filling current of 1mA at 10 K. Thus the as irradiated spectrum of the irradiated sensor can be compared with the ones recorded for some annealing steps. In comparison to the spectra shown for the low 23 MeV proton fluence the ratio between the E(30K) and H-defects peak height becomes more equal due to the higher introduction rate of acceptors as shown in figure 8.7. The E(30K) shows a strong increase in height with annealing, while only the H(151K) of the H-defects increases. Another observation is the higher ratio between the H(40K) and the E(30K) peak height compared to the lower fluence.

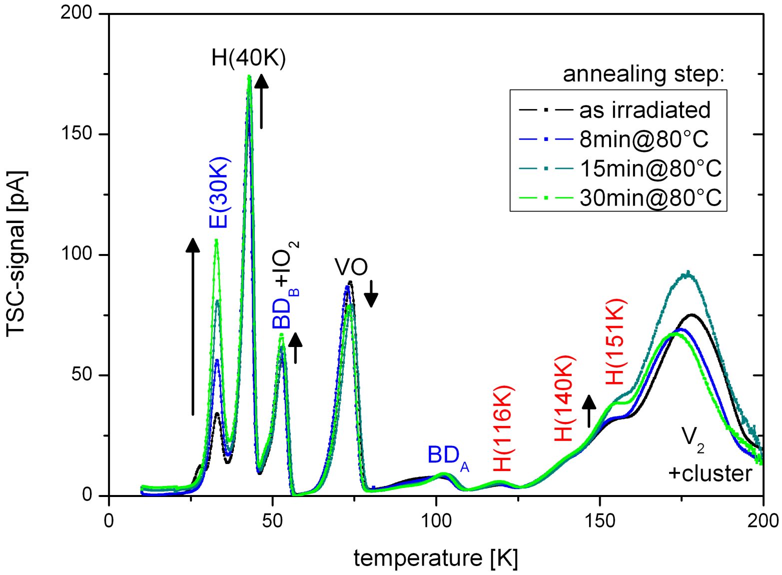

Figure 8.13: Evolution of TSC spectra during the annealing at 80 °C for MCZ200N irradiated with $\Phi_{eq} = 9.5 \times 10^{13}$ cm^{-2}, measurement parameters: $T_{fill} = 10$ K, different t_{fill}, $I_{fill} = 1$ mA, and $U_{rev} = 300$ V.

Comparison of N_{eff}^{calc} and N_{eff}

To verify if the analysis of the defects with impact on the SC is completely, N_{eff}^{calc} is compared with N_{eff} extracted from the CV measurements of U_{dpl}. In figure 8.14 this is done for three sensors after 23 MeV proton irradiation. Open symbols denote N_{eff}^{calc} while full symbols represents N_{eff} calculated from CV measurements. At all times N_{eff}^{calc} is higher than N_{eff}, which means that the defect analysis either overestimates the donor concentration or underrates the acceptor concentration. As described before, this is partly an effect of the donor removal that cannot be extracted from the spectra. But it could also be, that another effect is still missing. On the one hand there is a hole trap in figure 8.12, which could also be a defect with impact on the SC. This has to be investigated in more detail, by e. g. longer annealing studies. On the other hand the H(40K) could be responsible. By comparing N_{eff} and N_{eff}^{calc} it became very clear that the high concentration of the H(40K) cannot contribute with negative space charge. Otherwise N_{eff}^{calc} would become way too low. But the activation energy of the H(40K) lies near the one of the E(30K) defect. Therefore some kind of interaction or shielding could lead to a smaller contribution of the E(30K) concentration than expected.

Another explanation for the difference between N_{eff} extracted from CV measurements and N_{eff}^{calc} can be given by the fact that in case of a double peak shape of the electric field, the space charge is not uniform and U_{dpl} is smaller for the sensor with two depletion regions growing from both sides of the sensor, compared to a sensor with a uniform space charge region. On the other hand the deep defects ($\Delta E_a \approx 0.55$ eV) responsible for the double peak electric field distribution cannot be detected by the TSC method because they are hidden by the dark current. With the TSC method the maximum temperature for recording defect level due to emitted charge is approximately 200 K, which is equivalent to 0.48 eV [Fei97]. The evaluated defects from TSC measurements with impact on the SC have levels in the band gap that are not as deep as those responsible for the double peak in the electric field and it is assumed that they are distributed uniformly throughout the SCR. Therefore, N_{eff} from CV measurement could be expected to be smaller than N_{eff}^{calc}.

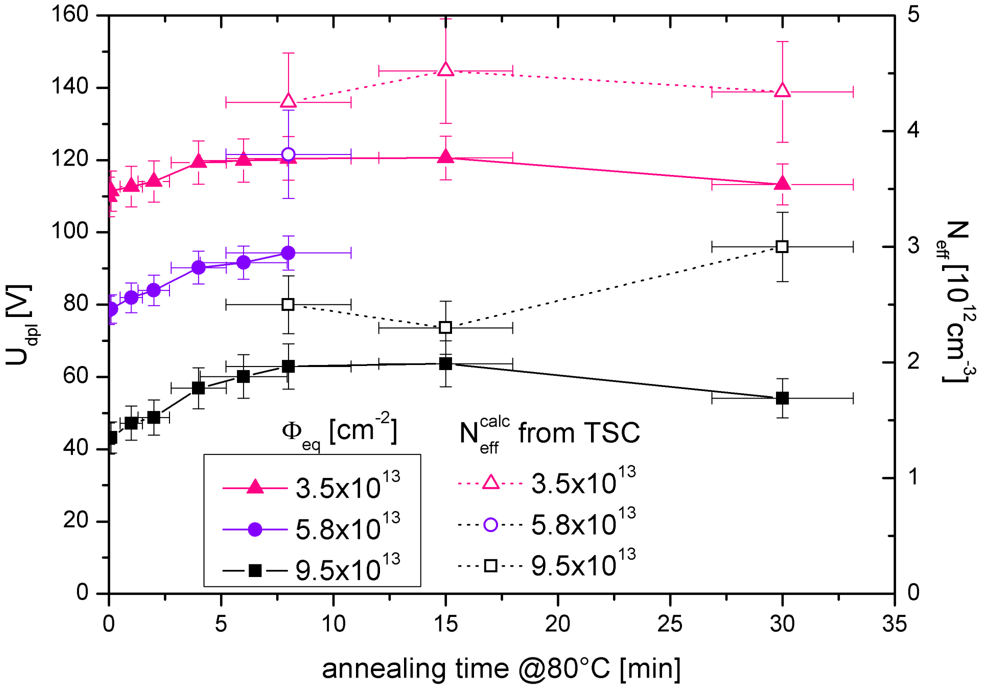

Figure 8.14: Comparison of U_{dpl}, N_{eff} (CV measurements) and N_{eff}^{calc} of MCZ200N irradiated with 3.5, 5.8 and 9.5×10^{13} cm^{-2} 23 MeV protons as a function of the annealing time at 80 °C.

8.2.2 Comparison of Defects in MCZ200N after 23 MeV and 23 GeV Proton Irradiation

A direct comparison of defect generation after 23 GeV and 23 MeV proton irradiation in TSC spectra was unfortunately only possible for a very low fluence of $\Phi_{eq} \approx 3 \times 10^{13}$ cm^{-2}. In this fluence range the space charge has not changed that much yet. N$_{eff}$ of the MCZ200N diode irradiated with $\Phi_{eq} = 9.6 \times 10^{12}$ cm^{-2} 23 GeV protons decreases during irradiation by about 0.42×10^{12} cm^{-3}, while the diode irradiated with $\Phi_{eq} = 3.5 \times 10^{13}$ cm^{-2} 23 MeV protons shows a decrease of N$_{eff}$ by about 1×10^{12} cm^{-3}. This are the effects of the donor removal. The difference might be due to the higher fluence of 23 MeV protons. From the TSC spectra in figure 8.15 the expected higher ratio between acceptors and donors after 23 MeV proton irradiation can not be confirmed. While the 23 GeV spectrum shows a slightly higher H-defect concentration, the E(30K) peak is much higher after 23 MeV proton irradiation. But another interesting peculiarity is the concentration of the H(40K) after 23 MeV proton irradiation. An assumption could be, that this defect in some kind constrains the effect of the E(30K).

The BD$_B$ + IO$_2$ complex disappears for 23 GeV proton irradiation after 30 minutes at 80 °C that this is not the case for the 23 MeV irradiated sample. This could be a result of a longer annealing due to the repetition of measurements.

By comparing N$_{eff}^{calc}$ and N$_{eff}$ from CV measurements in figure 8.16, obviously the defects used for the calculations of N$_{eff}^{calc}$ are not reproducing the N_{eff} from CV measurements. While only the N$_{eff}^{calc}$ point for the 23 GeV irradiated MCZ200N lies within the errors slightly above the expected N$_{eff}$, the N$_{eff}^{calc}$ points for the 23 MeV MCZ200N irradiated sample shows an approximately 1×10^{12} cm^{-3} higher N_{eff}. A contribution from donor removal might explain a major part of this deviation.

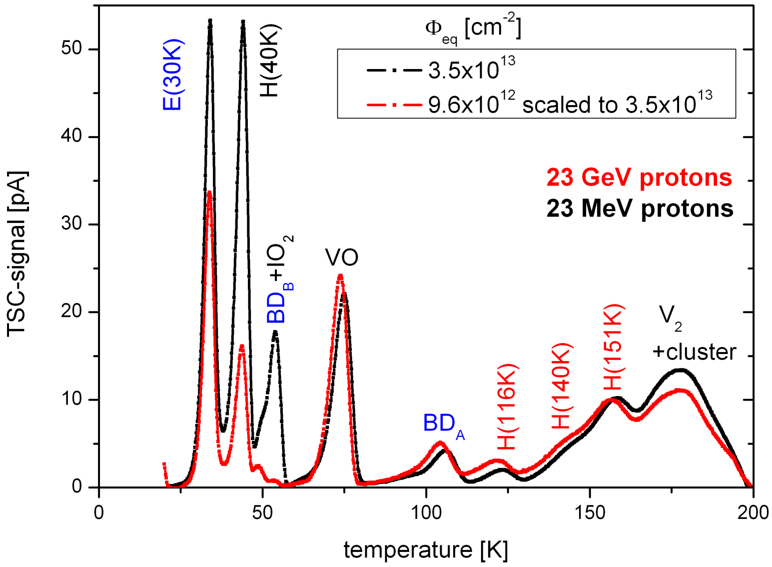

Figure 8.15: Comparison of TSC spectra for $\Phi_{eq} = 9.6 \times 10^{12}$ cm^{-2} 23 GeV and $\Phi_{eq} = 3.5 \times 10^{13}$ cm^{-2} 23 MeV proton irradiated MCZ200N diodes annealed to 30 minutes at 80 °C, measurement parameters: $T_{fill} = 20$ K, $t_{fill} = 60$ s, $I_{fill} = 1$ mA, and $U_{rev} = 150$ V.

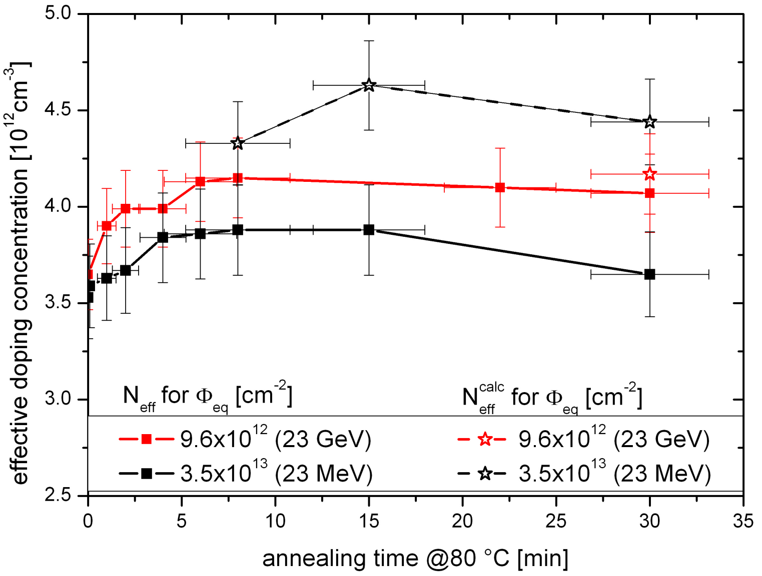

Figure 8.16: Comparison of N_{eff} (full squares) and N_{eff}^{calc} (open stars) for MCZ200N irradiated with 3.5×10^{13} cm^{-2} 23 MeV and 9.6×10^{12} cm^{-2} 23 GeV protons, N_{eff}^{calc} calculated according to equation 8.1.

8.2.3 RD50 MCz irradiated with 23 MeV Protons

In chapter 7.2 the macroscopic results of RD50 MCz after 23 MeV proton irradiation have been presented and $\Phi_{inv} = 1.97 \times 10^{14}$ cm^{-2} was determined. Two 23 MeV proton fluences, 7.4×10^{13} and 1.4×10^{14} cm^{-2}, were available for TSC measurements and the spectra after an annealing of 30 minutes at 80 °C are shown in figure 8.17. As expected the peak height increases with larger fluences, but a non proportional increase of the H(151K) peak appears. Because of the abnormal peak shape a type inversion due to the in- or activation of donors or acceptors at that temperature might be considered. Another effect could be a temporary non-depletion of the sensor, that might lead to an increase of the peak. Another observation is the ratio between E(30K) and H(40K), while the H(40K) shows an equal peak height after the lower fluence, after 1.4×10^{14} cm^{-2} the E(30K) peak is higher. The IR of H(40K) is much higher than the one of E(30K) (see chapter 8.2.1) for HPK sensors, therefore this material has a different response to the 23 MeV proton irradiation than the MCZ200N from HPK. Another explanation is the strong grow of E(30K) with annealing, which would lead to a higher IR extracted at larger annealing times.

Because it is not possible to achieve a sufficient filling current of 1 mA for proton fluences $\geq 3 \times 10^{14}$ cm^{-2}, the sensor irradiated with a fluence of 1.4×10^{14} cm^{-2} was the most suited sample to study the mechanism of type inversion. Therefore also the annealing behavior of this sensor was investigated by TSC measurement, see figure 8.18. The only big changes in defect concentration respectively peak heights are observed for the E(30K) and H(151K). Both are increasing and their space charge seems to compensate each others. In section 7.2 only a small change in U$_{dpl}$ and N$_{eff}$ is observed.

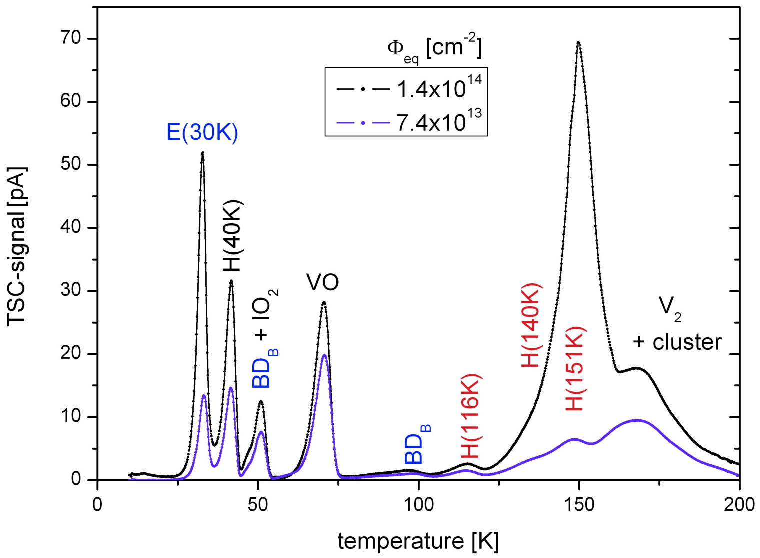

Figure 8.17: TSC spectra of RD50 MCz after 7.4×10^{13} and 1.4×10^{14} cm^{-2} 23 MeV protons annealed to 30 minutes at 80 °C, measurement parameters: $T_{fill} = 10$ K, $t_{fill} = 30$ s, $I_{fill} = 1$ mA, and $U_{rev} = 300$ V.

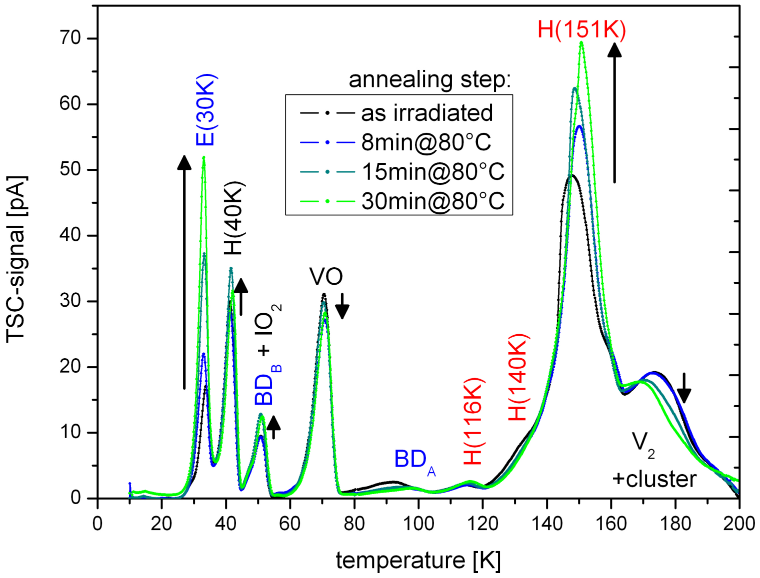

Figure 8.18: Evolution of TSC spectra during the annealing at 80 °C taken from RD50 MCz irradiated with 1.4×10^{14} cm^{-2} 23 MeV protons, measurement parameters: $T_{fill} = 10$ K, $t_{fill} = 30$ s, $I_{fill} = 1$ mA, and $U_{rev} = 300$ V.

8.3 Conclusion of the Microscopic Results

By means of DLTS measurements a very high concentration of the thermal double donor E(61K) is observed in non-irradiated MCZ200N, which contributes to N_{eff} with 54 %. While in FZ200N, which has a similar oxygen concentration as MCZ200N, the E(61K) concentration is not high enough to influence N_{eff} significantly.

After $\Phi_{eq} \approx 1 \times 10^{11}$ cm^{-2} 23 GeV proton irradiation this E(61K) concentration increases in both types of material. However, MCZ200N shows a stronger defect generation than FZ200N.

The defect generation by 23 MeV proton irradiation is investigated in detail by the TSC method, especially for HPK MCZ200N and RD50 MCz. Unfortunately diodes irradiated with fluences $> \Phi_{inv}$ could not be analyzed in a proper way because it was not possible to achieve a sufficient forward current to fill the defects. Which is a special problem for proton irradiation, previously seen [Jun11]. Therefore the emphasis is put on fluences 0.9×10^{13} cm^{-2} $< \Phi_{eq} <$ 2×10^{14} cm^{-2}. It was possible to identify the donors; E(30K) and BD-center like the acceptors; H(116K), H(140K) and H(151K). Additionally the H(220K) hole trap is seen in light injection spectra by illumination of the back (hole signal) of the sensor. This defect is not yet characterized, but could be a current generator or another acceptor, which then would contribute to N_{eff} with negative SC and would lead therefore to a better agreement of N_{eff}^{calc} with N_{eff}(CV measurements). In this work a further characterization of this defect was not possible, because of its overlap with the V_2 and other clusters. For a more detailed study, the annealing has to be expanded.

The hole trap H(40K) appeared after 23 MeV proton irradiation in a remarkably high concentration and with field-emission effect. Therefore this hole trap was studied in more detail to identify if this defect contributes with negative SC to N_{eff}. Within the investigation it could be excluded that the H(40K) does contribute with its high concentration, but there are hints that this defect does influence the impact of the E(30K) concentration. The field-emission effect might not be due to the Poole-Frenkel effect, but may be due to an other effect like e.g. tunneling.

The calculated defect parameters of the E(30K) and H(40K) are shown in table 8.2, where the errors are raised only statistically. The parameters of the E(30K) are in agreement with previous studies [Jun11] and the H(40K) could be further characterized. The introduction rate of the H(40K) defect is highest for all defects under investigation (see table 8.1), which makes it even more important to understand its influence.

defect	activation energy ΔE_a [eV]	capture cross section $\sigma_n[10^{-13}\ \mathrm{cm}^2]$	$\sigma_p[10^{-15}\ \mathrm{cm}^2]$	introduction rate IR $[\mathrm{cm}^{-1}]$
E(30K)	0.102 ± 0.002	1.2 ± 0.8	—	0.0367 ± 0.0034
H(40K)	0.108 ± 0.003	—	4.3 ± 3.9	0.1399 ± 0.0045

Table 8.2: Investigated defect parameters of the donor E(30K) and hole trap H(40K) in MCZ200N after 23 MeV proton irradiation.

Within the investigation of the defect generation of 23 MeV protons in RD50 MCz the high density of the H(151K) defect after a fluence of $\Phi_{eq} = 1.4 \times 10^{14}$ cm^{-2} can be interpreted as a cause for the type inversion after 23 MeV proton irradiation of oxygen-rich material due to the high introduction of negative SC by the H(151K). At a certain point it cannot be compensated by the positive SC of E(30K) any longer. Additionally the E(30K) maybe shielded by the H(40K). Anyway, these are just speculations.

Chapter 9

Summary and Conclusion

Within this work the influence of the particle energy on the radiation-induced damage (change of the effective doping concentration/dark current/charge collection efficiency) of Si sensors for protons was studied. Two proton energies, 23 MeV and 23 GeV, were available for the investigations. Taking into account that in previous studies all oxygen-lean n-type materials undergo type inversion after both 23 GeV and also 23 MeV proton irradiation this work focussed on oxygen-rich n-type Si sensors. Therefore MCZ200N and FZ200N from Hamamatsu (HPK) as well as MCz sensors from RD50 with about the same oxygen concentration were electrically characterized and the radiation induced electrically active defects analyzed.

It could be proven that oxygen-rich material shows type inversion after 23 MeV proton irradiation, while the high oxygen content prevents this effect for sensors after 23 GeV proton irradiation. Additionally, a dependence on the producer of the sensors could be excluded. Moreover it has been proven that the material defects found in HPK sensors do not affect the electrical properties of the sensors after irradiation in a crucial way.

By TCT measurements a double peak structure of the current pulse shapes was seen after 23 MeV and 23 GeV proton irradiation for MCz and FZ sensors. However, for high bias voltages the maximum peak height increases after 23 MeV proton irradiation on the back (n^+ electrode) and after 23 GeV protons on the front (p^+ electrode) of the sensors. The charge collection efficiency (CCE) of the sensors is highest for MCZ200N diodes from Hamamatsu after 23 MeV and 23 GeV proton irradiation compared to FZ200N.

Via DLTS spectra a thermal double donor the E(61K) defect was observed with high concentration in a non-irradiated MCZ200N diode. FZ200N also contains thermal double donors before irradiation, but in a much lower concentration.

The most relevant defects with impact on the space charge (SC) are the E(30K) defect, which introduce positive SC, and the group of H-defects, which generate negative SC, found in neutron and 23 GeV proton irradiated devices. For 23 MeV proton irradiation the concentration of the E(30K) was expected to be lower or the concentration of the H-defect to be higher than after 23 GeV proton irradiation. This could not be observed. Instead, by means of TSC spectra MCZ200N diodes after 23 MeV proton irradiation showed a high concentration of the H(40K) defect. This defect does not have an impact on the SC, but might influence the E(30K) defect.

More detailed conclusions of the results are given at the end of chapter 7 and 8.

Outlook

For the CMS tracker upgrade campaign investigating different sensor designs manufactured on different materials from Hamamatsu, a simulation of the conditions in the future CMS detector has highest priority. Therefore the impact of the proton energy on the radiation hardness of the sensors has to be predicted under most realistic conditions. The campaign decided to perform additional irradiations with 800 MeV protons on the HPK sensors, because most of protons and pions in the tracker region are in the range between 100 MeV and 1 GeV. The behavior of the oxygen-rich diodes after irradiation with 800 MeV will be crucial for the decision of the material used for the tracker upgrade.

First results indicate that 800 MeV proton irradiations have a similar impact on the effective doping concentration of oxygen-rich materials as 23 MeV protons. After a fluence of 3.5×10^{14} cm^{-2} 800 MeV protons RD50 MCz diodes provide hints for type-inversion [Jun12].

These observations are only a first hint for type-inversion of oxygen-rich sensors after 800 MeV proton irradiation, which will be further investigated by annealing studies also for Hamamatsu diodes. Additionally, the results have to be compared with pion irradiations, because the radiation field in the innermost part of the tracker is dominated by pions. It would be interesting to see if also the pion damage is energy dependent and if so, wether the energy range is comparable with that for protons.

List of Figures

List of Tables

Bibliography

[Akk01] A. Akkerman, J. Barak, M. B. Chadwick, J. Levinson, M. Murat, Y. Lifshitz, Updated NIEL calculations for estimating the damage induced by particles and γ-rays in Si and GaAs,
Radiation Physics and Chemistry 62 (2001) 301-310
doi:10.1016/S0969-806X(01)00207-9

[Aff10] A. Affolder, P. Allport, G. Casse, Collected charge of planar silicon detectors after pion and proton irradiations up to $2.2 \times 10^{16} \mathrm{n}_{eq}\mathrm{cm}^{-2}$,
Nucl. Instr. and Meth. in Phys. Res. A, v. 623, p. 177-179 (2010)
doi:10.1016/j.nima.2010.02.187

[Chi95] A. Chilingarov, H. Feick, E. Fretwurst, G. Lindström, S. Roe, T. Schulz, Radiation studies and operational projections for silicon in the ATLAS inner detector.
Nucl. Instr. and Meth. in Phys. Res. A, v. 360, p. 432-437 (1995)
doi:10.1016/0168-9002(95)00110-7

[Gut12] CMS Beam Conditions and Radiation Monitoring Group, personal communication with M. Guthoff

[cnx12] Connexions, `www.cnx.org/content/m32000/latest/`
(version: 20th september 17.24PM 2012)

[Eck08] D. Eckstein, L. Andricek, E. Fretwurst, J. Lange, G. Lindström, H.G. Moser, I. Pintilie, R. Richter, R. Röder, Comparison of proton damage in thin FZ, MCz and epitaxial silicon detectors, presented on 12th RD50 workshop in Ljubljana,
2nd to 4th June 2008
`https://rd50.web.cern.ch/rd50/12th-workshop/default.htm`

[Ere02] V. Eremin, E. Verbitskaya, Z. Li, The origin of double peak electric field distribution in heavily irradiated silicon detectors
Nucl. Instr. and Meth. in Phys., Res. A 476 (2002) 556–564
doi:10.1016/S0168-9002(01)01642-4

[Erf12] J. Erfle, Irradiation study on diodes of different silicon materials for the CMS tracker upgrade, presented on 20th RD50 workshop in Bari,
30st May to 1nd June 2012
`https://indico.cern.ch/conferenceDisplay.py?ovw=True&confId=175330`

[Die10] A. Dierlamm, Irradiations in Karlsruhe,
presented on 16th RD50 workshop in Barcelona,
31st May to 2nd June 2010
`http://indico.cern.ch/conferenceDisplay.py?confId=86625`

[Fre38] J. Frenkel, On pre-breakdown phenomena in insulators and electronic semiconductors,
Phys. Rev., 1938
doi:10.1103/PhysRev.54.647

[Fre07] E. Fretwurst, F. Hönniger, G. Kramberger, G. Lindström, I. Pintilie and R. Röder, Radiation damage studies on MCz and standard and oxygen enriched epitaxial silicon device,
Nucl. Instr. and Meth. in Phys., Res. A 583-1 (2007)
doi:0907.3050

[Fei97] H. Feick, Radiation Tolerance of Silicon Particle Detectors — microscopic defects and macroscopic properties —,
PhD thesis, University of Hamburg,
DESY THESIS F35D-97-08 (August 1997)

[Gil97] K. Gill, G. Hall, B. MacEvoy, Bulk damage effects in irradiated silicon detectors due to clustered divacancies,
Journal of Applied Physics 82(1) (1997) 126-136.
doi:10.1063/1.365790.

[Gos59] B. Gossick, Disordered Regions in Semiconductors Bombarded by fast Neutrons,
Journal of Applied Physics 30(8) (8) (1959) 1214-1218,
doi:10.1063/1.1735295.

[Hal52] R. N. Hall, Electron-Hole Recombination in Germanium,
Physical Review B, 87:387, 1952.

[Har68] J. L. Hartke, The Three-Dimensional Poole-Frenkel Effect,
Journal of Applied Physics 39 (1968) 4871
doi:10.1063/1.1655871.

[Hoe07] F. Hönniger, Radiation Damage in Silicon — Defect Analysis and Detector Properties —
PhD Thesis, University of Hamburg,
DESY-THESIS 2008-002 (January 2008).

[Huh02] M. Huhtinen, Simulation of non-ionising energy loss and defect formation in silicon,
Nucl. Instr. and Meth. in Phys., Res. A 491 (2002) 194-215,
doi:10.1016/S0168-9002(02)01227-5.

[Jun03] I. Jun, M. A. Xapsos, S. R. Messenger, E. A. Burke, R.J. Walters, G. P. Summers, T. Jordan, Proton Nonionizing Energy Loss (NIEL) for Device Applications,
IEEE Transactions on Nuclear Science, vol. 50, issue: 6, pages 1924-1928, Dec. 2003
doi:10.1109/TNS.2003.820760.

[Jun11] A. Junkes, Influence of radiation induced defect clusters on silicon particle detectors,
PhD thesis, University of Hamburg,
DESY-THESIS 2011-031 (October 2011).

[Jun12] A. Junkes, Measurements on 800 MeV proton irradiated diodes,
presented on 21th RD50 workshop at CERN,
14th to 16th November 2012.
`https://indico.cern.ch/conferenceDisplay.py?confId=200290`

[Kra01] G. Kramberger, Signal development in irradiated silicon detectors,
PhD thesis, University of Ljubljana, 2001.

[Kas09] K. Kaska, M. Moll, TCT measurements on MCz n- and p-type after proton and neutron irradiation,
presented on 15th RD50 workshop at CERN, Geneva (Switzerland),
16th to 18th November 2009.
`http://indico.cern.ch/conferenceDisplay.py?confId=65918`

[Lan09] J. Lange, Radiation Damage in Proton — Irradiated Epitaxial Silicon Detectors,
Diploma thesis, University of Hamburg,
DESY-THESIS 2009-022 (July 2009).

[Laz87] M. S. Lazo, D. M. Woodall, P. J. McDaniel, Silicon and silicon dioxide neutron damage functions,
In Proc. Fast Burt React. Workshop, 1986. Sandia National Laboratories, 1987. [Tech. Rep.] SAND, SAND87-0098 Vol. 1.

[Li10] Z. Li, W. Chen, V. Eremin, R. Gul, Y. H. Guo, J. Harkonen, P. Luukka, E. Tuovinen, E. Verbitskaya, Equal-double junctions in 24 GeV/ c proton-irradiated MCZ n- and p-type Si detectors: A systematic transient current technique investigation,
Nucl. Instr. and Meth. in Phys., Res. A , vol. 612, no. 3, pp. 539-548 (2010)
doi:10.1016/j.nima.2009.08.082.

[Lin01] G. Lindström et al., Radiation hard silicon detectors-developments by the RD48 (ROSE) collaboration,
Nucl. Instr. and Meth. in Phys., Res. A466 (2001) 308-326,
doi:10.1016/S0168-9002(01)00560-5

[Met09] J. Metcalfe, M. Hoeferkamp, S. Seidel, Capacitance Measurements and Depletion Voltage for Annealed Fz and MCz Diodes,
presented on 14th RD50 workshop in Freiburg, 3rd to 5th June 2009.
`https://rd50.web.cern.ch/rd50/14th-workshop/default.htm`

[Mol99] M. Moll, Radiation Damage in Silicon Particle Detectors — Microscopic Defects and Macroscopic Properties —,
PhD thesis, University of Hamburg,
DESY-THESIS 1999-040 (December 1999).

[Mon02] E. V. Monakhov, B. S. Avset, A. Hallén, B.G. Svensson, Formation of a double acceptor center during divacancy annealing in low-doped high-purity oxygenated Si.
Phys. Rev. B 65 233207
doi:10.1103/PhysRevB.65.233207.

[Neu10] C. Neubüser, Untersuchungen zur Stromgenerierung eines strahleninduzierten Defektes in Silizium (The mechanism of current generation in irradiated silicon diodes),
Bachelor Thesis, University of Hamburg, 2010.

[Pac10] N. Pacifico, D. Creanza, M. de Palma, N. Manna, G. Kramberger, M. Moll, A TCT and annealing study on Magnetic Czochralski silicon detectors irradiated with neutrons and 24GeV/c protons,
Nucl. Instr. and Meth. in Phys., Res. A612: 549-554 (2010)
doi:10.1016/j.nima.2009.08.019.

[Pin06] I. Pintilie, M. Buda, E. Fretwurst, G. Lindström, J. Stahl, Stable radiation-induced donor generation and its influence on the radiation tolerance of silicon diodes,
Nucl. Instr. and Meth. in Phys., Res. A556: 197-208 (2006)
doi:10.1016/j.nima.2005.10.013.

[Pin08] I. Pintilie, E. Fretwurst, G. Lindström, Cluster related hole traps with enhanced-field-emission — the source for long term annealing in hadron irradiated Si diodes,
Applied Physics Letters 92 (2008) 024101
doi:10.1063/1.2832646.

[Pin09] I. Pintilie, G. Lindström, A. Junkes, E. Fretwurst, Radiation Induced and Cluster-Related Defects with Strong Impact to Damage Properties of Silicon Detectors,
Nucl. Instr. and Meth. in Phys., Res. A61: 52-68 (2009)
doi:10.1016/j.nima.2009.09.065.

[Rad12] R. Radu, personal communication, 2012.

[Ram38] S. Ramos, Currents Induced by Electron Motion,
Proceedings of the IRE 27 (9): 584–585
doi:10.1109/JRPROC.1939.228757.

[Sve91] B. G. Svensson, B. Mohadjeri, A. Hallén, J. H. Svensson, J. W. Corbett, Divacancy acceptor levels in ion-irradiated silicon,
Physical Review B 43 (3) (1991) 2292-2298
doi: 10.1103/PhysRevB.43.2292.

[Sho52] W. Shockley, W. T. Read, JR. Statistics of the Recombinations of Holes and Electrons,
Physical Review, 87:835 (1952)
doi:10.1103/PhysRev.87.835

[Sze01] S. M. Sze, Semiconductor Devices, Physics and Technology,
Wiley, second ed., 2001.

[Poe13] T. Pöhlsen,
PhD Thesis, to be published in 2013.

[Wei91] S. Weiss, Halbleiteruntersuchungen mit dem DLTFS- (Deep Level Transient Fourier Spectroscopy) Verfahren,
PhD Thesis, Universität Kassel, January 1991.

[wiki1] Wikipedia, `http://de.wikipedia.org/w/index.php?title=Datei:Brillouin_Zone_(1st,_FCC).svg`
(version: 18th september 12.03PM 2012).

[wiki2] Wikipedia, `http://de.wikipedia.org/w/index.php?title=Datei:Band_structure_Si_schematic.svg`
(version: 18th september 12.31PM 2012).

[Wun92] R. Wunstorf, Systematische Untersuchungen zur Strahlenresistenz von Silizium-Detektoren für die Verwendung von Hochenergie-Experimenten,
PhD thesis, University of Hamburg, 1992.

Appendix

.1 TCT pulses

MCZ200N irradiated with 23 MeV protons

Here TCT pulses for MCZ200N irradiated with 2.4×10^{14} cm^{-2} 23 MeV protons are shown after annealing steps of 8 minutes and 30 minutes at 80°C. The shape of the pulses change not only for increasing bias voltages, but also for different annealing due to the changing effective doping concentration.

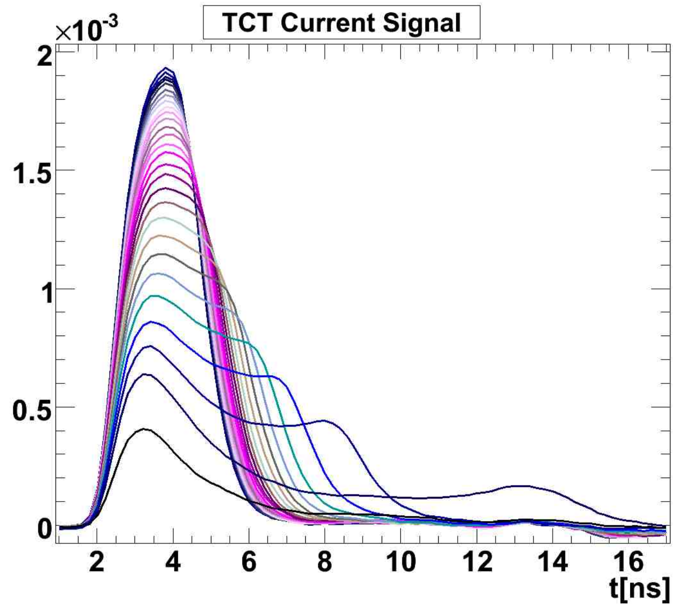

Figure 1: TCT pulses of MCZ200N irradiated with 2.4×10^{14} cm^{-2} 23 MeV protons annealed to 8 minutes at 80 °C, for different bias voltages, beginning from 10 V in 20 V steps up to 550 V.

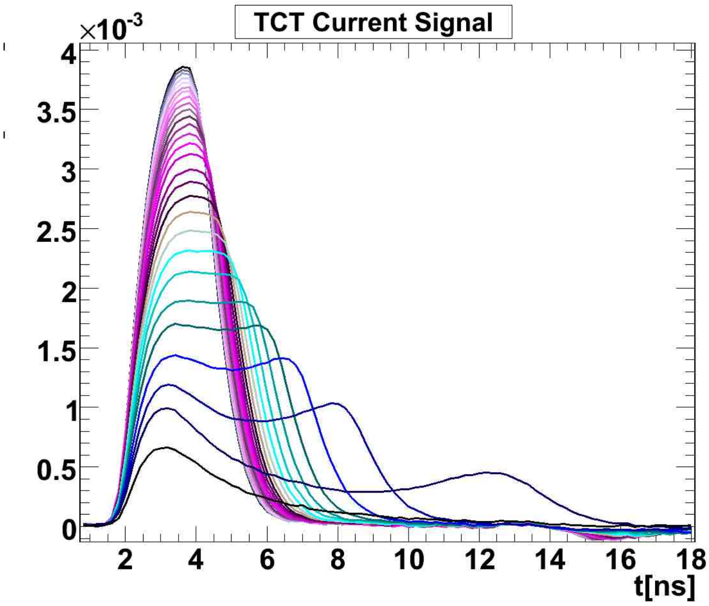

Figure 2: TCT pulses of MCZ200N irradiated with 2.4×10^{14} cm^{-2} 23 MeV protons annealed to 30 minutes at 80 °C, for different bias voltages, beginning from 10 V in 20 V steps up to 550 V.

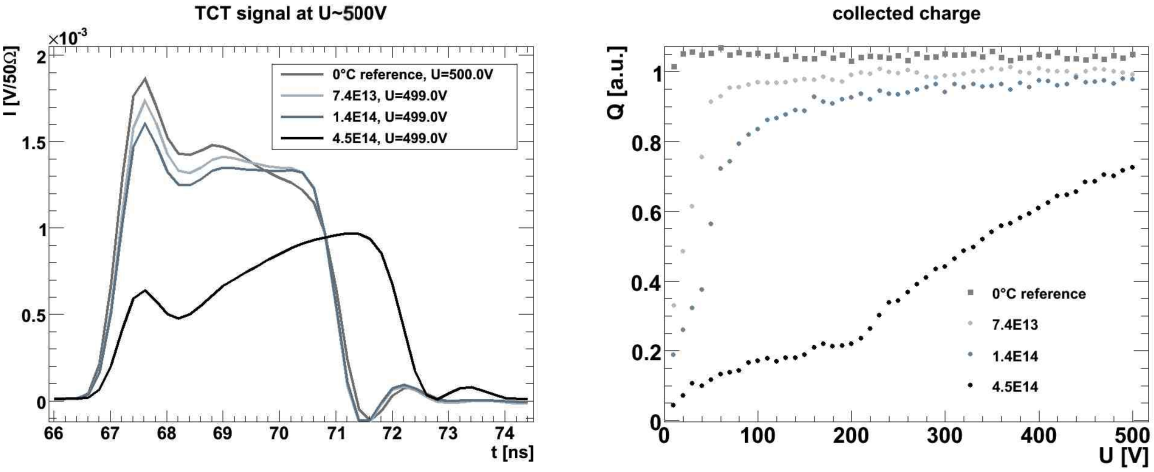

(a) electron collection

(b) hole collection

Figure 3: TCT pulses and CCE taken for red laser illumination from the front of the sensors, measured as irradiated at 0 °C. The sensors are RD50 MCz pad diodes irradiated with three different fluences of 23 MeV protons.

RD50 MCz irradiated with 23 MeV protons

Here TCT pulses and charge collection efficiency of RD50 MCz irradiated with 23 MeV protons are shown. Figure 3a shows TCT pulses after illumination of the front with a 660 nm laser measured as irradiated for three different proton fluences ($\Phi_{eq} = 7.4 \times 10^{13}$, 1.4×10^{14} and 4.5×10^{14} cm^{-2}). This figure and figure 3b, where the CCE of this diodes is shown for increasing voltages, proves the space charge sign inversion after $\Phi_{eq} = 4.5 \times 10^{14}$ cm^{-2} 23 MeV proton irradiation. The sensor irradiated with the highest fluence shows only an increase in CCE after full depletion (”pinch-off”-effect) and the slope of the TCT pulse is positive.

It should be mentioned that the very pronounced high peak at the beginning of the pulses for illumination from the front and the back is most probably due to a damped oscillation of the preamplifier triggered by the fast rise of the signal, also visible in the following wiggles overlapped to the main transient. Thus this first early high peak is not a real signal of the diode. This effect is seen for all diodes with a small pad area (RD50 MCz diodes).

In figure 4 the evolution of the TCT pulse with increasing bias voltage is shown for the fluence of $\Phi_{eq} = 4.5 \times 10^{14}$ cm^{-2} 23 MeV protons. The peak at the end of the signals is highest, which means for illumination from the front, that the electric field distribution is highest at the n^{+} electrode. Only for highest voltages of nearly 500 V the pulse shape becomes flat due to the extremely high field in the sensor.

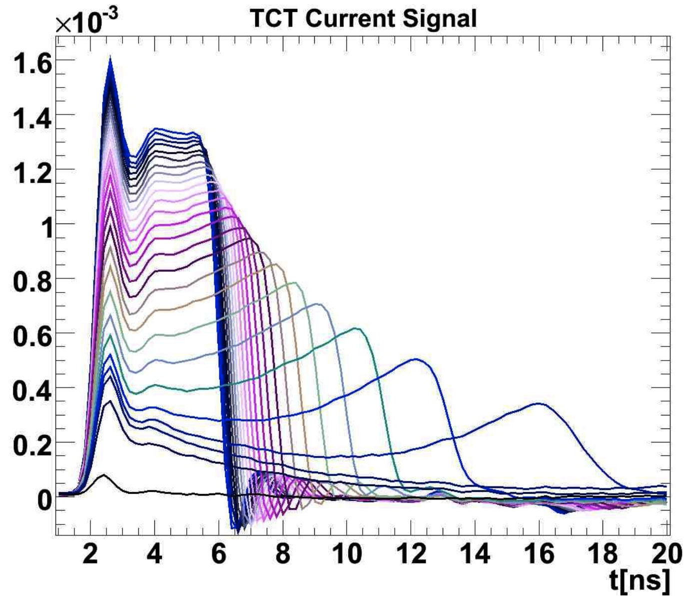

Figure 4: TCT pulse evolution of RD50 MCz diode after $\Phi_{eq} = 4.5 \times 10^{14}$ cm^{-2} 23 MeV proton irradiation, taken for red laser illumination from the front of the sensor, as irradiated measured at 0 °C. The voltages vary from 0 V up to 500 V in 20 V steps.

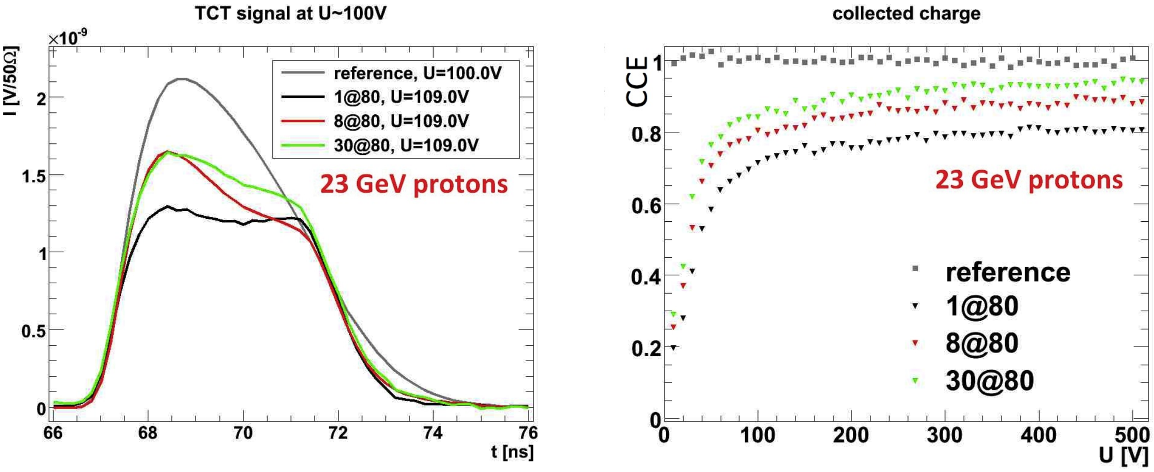

(a) electron signal

(b) CCE (electron collection)

Figure 5: FZ200N after 23 GeV proton irradiation of $\Phi_{eq} = 2.9 \cdot 10^{14}$ cm^{-2}, measured at 0 °C after red laser illumination from the front for a couple of annealing steps: 1, 8 min to 30 minutes at 80 °C.

FZ200N irradiated with 23 GeV protons

The here presented figures prove that the FZ200N sensor irradiated with $\Phi_{eq} = 2.9 \cdot 10^{14}$ cm^{-2} 23 GeV protons stays n-type after irradiation. The TCT pulses shown for illumination from the front with 660 nm laser show the peak maximum at the beginning of the pulses, see figure 5a. This improves with annealing, like the CCE in figure 5b does. Also with additional trapping correction this picture will not change in a crucial way.

Acknowledgements

I would like to thank all my wonderful colleges for their support, good mood and the friendly working atmosphere. I am grateful to everyone who contributed to this work: Doris Eckstein, Joachim Erfle, Thomas Pöhlsen, Alexander Dierlamm, Robert Eber, Georg Steinbrück and Roxana Radu.

The teamwork with Peter Buhmann and Michael Matysek was a pleasure and every time cheerful, like the humorous lunch and coffee breaks, sometimes in German, English or Italian. This enabled me to be productive and having fun doing this work.

Also I want to thank the student research assistants (Christian, Evangelos, Jascha and Ole) for doing parts of the measurements and for their interest in this special topic.

I am very thankful for the supervision of Dr. Eckhart Fretwurst, whose expertise, knowledge and kindness is preeminent.

Special thanks to Alexandra Junkes, who is not only a friend but an inspiration. She always challenged, supported and encouraged me. Without her this thesis would not be possible.

Additionally, the advices and trust from Prof. Dr. Erika Garutti — a very successful woman in physics — always increased my self-confidence.

I wish to express my gratitude to Prof. Dr. Robert Klanner, sharing generously his knowledge and giving steady orientation for highest demands.

I am most thankful for Prof Dr. Wolfgang Hansen as my mentor for more than five years and my second consultant for this thesis.

I am grateful to the RD50 collaboration for letting me be a part of the community, especially to Maurice Glaser and Federico Ravotti for the irradiations at the PS (CERN) and Felix Bögelspacher for the irradiations at the KAZ in Karlsruhe. Also I need to thank the AIDA collaboration for the financial support.

Last but not least, I want to thank my family, friends and roommates for keeping my mind open for things beyond physics. Your support often helped me not to despair. Special thanks to my mother, who supports me my whole life, in all situations. I feel blessed every day for all the love surrounding me.

Hiermit bestätige ich, dass die vorliegende Arbeit von mir selbständig verfasst wurde und ich keine anderen als die angegebenen Hilfsmittel — insbesondere keine im Quellenverzeichnis nicht benannten Internet-Quellen — benutzt habe und die Arbeit von mir vorher nicht einem anderen Prüfungsverfahren eingereicht wurde. Die eingereichte schriftliche Fassung entspricht der auf dem elektronischen Speichermedium. Ich bin damit einverstanden, dass die Master-Arbeit veröffentlicht wird.

Hamburg, 31. Januar 2013, Coralie Neubüser